Master's Thesis of Engineering

Tensile Behavior Characteristics of GFRP and Steel Rebar Reinforced UHPFRC

GFRP 및 철근 보강 UHPFRC의

인장 거동 특성

August 2023

Graduate School of Engineering
Seoul National University
Architecture and Architectural Engineering

Seungkee Hong

Tensile Behavior Characteristics of GFRP and Steel Rebar Reinforced UHPFRC

Advisor: Sung Gul Hong

Submitting a master's thesis of
Architecture and Architectural Engineering

June 2023

Graduate School of Engineering
Seoul National University
Architecture and Architectural Engineering

Seungkee Hong

Confirming the master's thesis written by
Seungkee Hong

August 2023

Chair	**HONG-GUN PARK**	**(Seal)**
Vice Chair	**SUNG-GUL HONG**	**(Seal)**
Examiner	**CHEOL-HO LEE**	**(Seal)**

Abstract

Tensile Behavior Characteristics of GFRP and Steel Rebar Reinforced UHPFRC

Hong, Seungkee
Department of Architecture and Architectural Engineering
College of Engineering
Seoul National University

When Ultra-High-Performance-Fiber-Reinforced-Concretes (UHPFRCs) are combined with reinforcing bars (R-UHPFRC), it leads to structural solutions that meet rigorous durability and mechanical requirements. However, the challenge lies in addressing the higher residual stresses resulting from increased shrinkage and confinement of the reinforcing bars compared to conventional reinforced concrete. Although there have been numerous investigations on the tensile behavior of normal concrete and UHPC reinforced with GFRP bars, research on UHPFRC reinforced with GFRP bars is scarce, particularly when it comes to studying the impact of the steel fiber volume ratio.

The objective of this thesis is to examine how UHPFRC behaves when

reinforced with steel and glass-fiber-reinforced-polymer (GFRP) re-bars, and to make a comparative analysis between them. Specifically, the study examines the effects of changes in rebar type and steel fiber volume ratio on the uniaxial tensile behavior of reinforced UHPFRC. The research follows a systematic approach that explores the overall tensile behavior, the effects of shrinkage on member shortening, and the tension stiffening effect.

The first part of the study involves analyzing the global uniaxial tensile behavior of R-UHPFRC specimens, including ultimate stress and strain in the elastic and plastic states, as well as crack formations and characteristics. Next, the research focuses on the effects of shrinkage on member shortening and residual stress, examining the cracking stresses from both experimental and modified results. Finally, the study compares the tension stiffening effect for different variables, using the Tension Chord Model and Load Sharing Concept to analyze the contribution of the concrete matrix and re-bar to the tensile stress.

The study's comprehensive approach, from intuitive observations to analytical results, can contribute to the development of design guidelines for UHPFRC structures that maximize their performance and durability.

Keywords : Steel Fiber Volume Ratio, Reinforcement Ratio, Shrinkage, Residual Stress, Tension Stiffening Effect.

Student Number : 2021-28331

Contents

List of Tables

List of Figures

Chapter 1. Introduction

1.1 Background

Ultra-high-performance-concrete (UHPC), usually defined as a cement composite with an average compressive strength above about 150 MPa, is a type of cement-based composite consisted of high cementitious material content and an optimized gradation of granular materials. The concept of UHPC was first introduced by Richard and Cheyrezy at the Bouygues Laboratory in France in the early 1990s [1]. Since then, many researchers have developed various types of UHPC, making it possible to exhibit excellent mechanical properties and durability provide significant benefits for creative designs and specific applications.

In the design of structural concrete, the material's ability to stretch without breaking, known as ductility or deformation capacity, is crucial. To address the low tensile strength and brittle response of concrete, steel fibers are used in concrete structures to improve their tensile properties. Over the past few decades, cementitious composites have undergone significant improvements in response to construction, environmental, and structural demands. Through direct tensile tests, numerous researchers have demonstrated that fiber-reinforced-concrete (FRC) members can exhibit ductile behavior even after cracking.

The addition of short, discontinuous fibers to UHPC results in a strain-hardening behavior under uniaxial tension, and it gives rise to a damage pattern

of closely spaced narrow cracks, as depicted in **Figure 1-1** [2]. Ultra-high-performance-fiber-reinforced-concrete (UHPFRC), with their high compressive and tensile strengths, as well as increased toughness due to steel fibers, provide engineers with a new range of materials and possibilities for structural design. Depending on the loading requirements, the tensile elements of UHPFRC can be designed with reinforcing bars, known as R-UHPFRC.

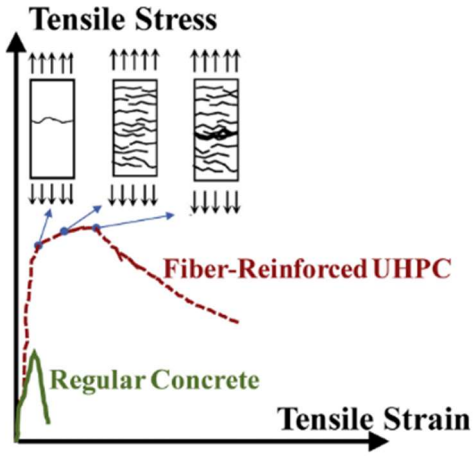

Figure 1-1 Typical tensile stress-strain curve and progressive cracking of fiber-reinforced UHPC (Hung et al. [2])

Unlike normal concrete, UHPFRC is vulnerable to a significantly high ultimate autogenous shrinkage of around 800 $\mu\varepsilon$, due to the low water-to-binder ratio (W/B) used in its composition [3]. When the high autogenous shrinkage of UHPFRC is restricted by internal reinforcing bars, tendons, forms, or adjacent structural members, it can result in significant residual tensile stress and shrinkage cracks in the concrete even without external loading. Several

studies have been conducted to reduce shrinkage stress in concrete, including the use of Glass-Fiber-Reinforced-Polymer (GFRP) bars to reduce restrained shrinkage stresses [4]. Recent research has indicated that the elastic modulus of GFRP bars is lower than that of steel bars, resulting in about one-fifth of the shrinkage stress level observed in concrete with steel bars, as shown in **Figure 1-2**. Consequently, incorporating GFRP bars is expected to have a positive impact on reducing restrained shrinkage stress.

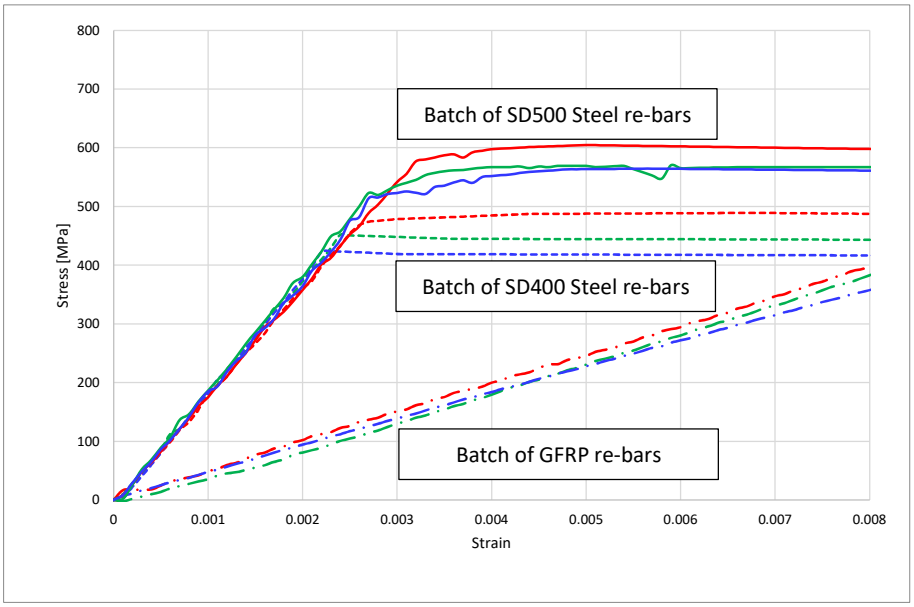

Figure 1-2 Tensile resopnse of GFRP, SD400 and SD500 steel re-bar respectively

In situations where steel is not a suitable reinforcement, such as areas that are prone to corrosion or magnetic fields, GFRP bars present a viable alternative.

Large deflections are common in GFRP bars due to their relatively low stiffness when compared to steel. This factor makes the limit of deflection and crack width at service loads the primary governing criteria in the design of members.

While there have been many notable studies on the tensile behavior of normal concrete and UHPC reinforced with GFRP bars, research on UHPFRC reinforced with GFRP bars remains limited, particularly in cases where the steel fiber volume ratio is the main focus.

1.2 Objectives and Outlines

The primary aim of this thesis is to investigate the uniaxial tensile behavior of reinforced ultra-high-performance fiber-reinforced concrete (R-UHPFRC) and compare the effects of changes in rebar type and steel fiber volume ratio. To accomplish this, the study follows a systematic approach that explores the overall tensile behavior from intuitive observations to analytical results.

The first step in this study involves comparing the global uniaxial tensile behavior of R-UHPFRC specimens. This includes analyzing the ultimate stress and strain in both the elastic and plastic states. Additionally, the study examines various crack formations, including transverse and splitting cracks, as well as crack characteristics like width and spacing.

Second, the study focuses on the detailed effects of member shortening due to shrinkage, such as residual stress and first cracking stress. The cracking stresses from the experimental results, which show the actual behavior with shrinkage observed from the test, and modified results, which show the behavior assuming there is no shrinkage, are the main focus. The study aims to find out how the reinforcement type and steel fiber ratio can affect the shrinkage and residual stress.

In the final part of the study, the tension stiffening effect is compared for different variables, such as re-bar type and steel fiber volume ratio. Both the Tension Chord Model and Load Sharing Concept are used to analyze the contribution of the concrete matrix and re-bar to the tensile stress. The bond factor, which provides a normalized value of the tension stiffening effect, is

derived and compared. This analysis aims to provide insights into how the choice of reinforcement and steel fiber content can affect the tension stiffening behavior of R-UHPFRC.

1.3 Test Set Up and Specimen Notation

1.3.1 Material Properties

Table 1-1 presents the mix proportions of the UHPC material used in this study for test specimens. The composite is consisted of cement, silica fume, quartz powder, silica sand, superplasticizer and water. The compressive strength of UHPC with following proportion performs up to 178MPa as shown in **Table 1-2**. Each of UHPFRC specimens were fabricated using UHPFRC materials with volume ratio 0%, 0.5%, 1%, 1.5% and 2% of steel fiber included. Only a single type of steel fiber was used, of which the diameter 0.2mm, length 13mm, aspect ratio 65.0, tensile strength 2500MPa and Young's Modulus 200GPa. **Figure 1-3** shows N-series (N-series refers to series of specimens without reinforcing bars, references) specimen uniaxial tensile test set up and corresponding stress-strain graph.

Table 1-1 Mix proportion of UHPC (by weight ratio, without fibers)

w/c	C	SF	Quartz	S	SP
0.222	1.0	0.25	0.35	1.1	0.04

Table 1-2 Compressive strength of UHPFRC

V_f [%]	0.0	0.5	1.0	1.5	2.0
f_c [MPa]	153	150	158	177	178

Table 1-3 Geometrical and physical properties of steel fiber.

d_f [mm]	l_f [mm]	Aspect ratio (l_f / d_f)	Density $[g/cm^3]$	f_{ft} [MPa]	E_f [GPa]
0.2	13.0	65.0	7.8	2500	200

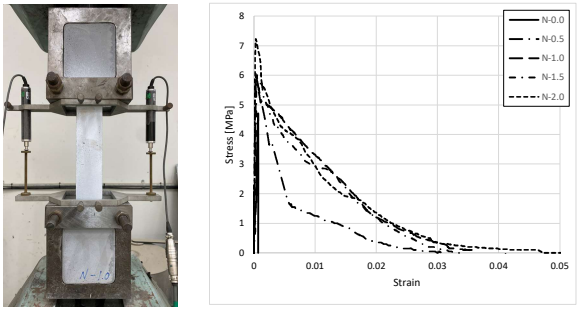

Figure 1-3 N-series UHPFRC specimens uniaxial tensile test set up and corresponding stress-strain graph

Uniaxial tensile tests for each bare steel and GFRP re-bars were done respectively to observe the independent tensile behavior. For GFRP re-bars, LVDT displacement gauge was used because of the wood grain-like fibers which makes it impossible to use strain gauges. Also, only elastic state of tensile behavior could be observed. It was impossible to measure the entire tensile behavior, because the dead-end part of GFRP re-bar was too weak in compressive force to bear UTM fixing equipment's fixing force. Linear behavior predicted through the given modulus of elasticity and ultimate stress of the material was employed to anticipate the subsequent behavior after measuring it through experimentation. **Figure 1-4** shows the GFRP re-bar uniaxial tensile test set up and corresponding stress-strain graph. For steel re-

bar, test procedure had conducted relatively according to the ASTM A370 standards [5]. Test set up and responsive stress-strain graph for SD400 and SD500 is presented in **Figure 1-5** respectively.

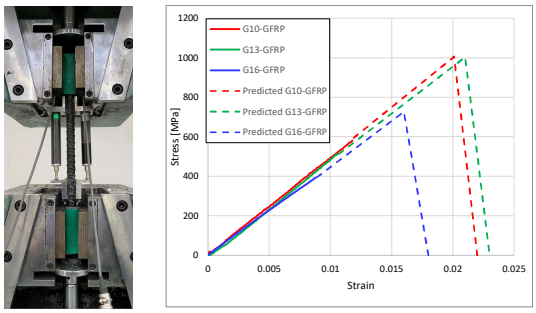

Figure 1-4 GFRP re-bar uniaxial tensile test set up and corresponding stress-strain graph

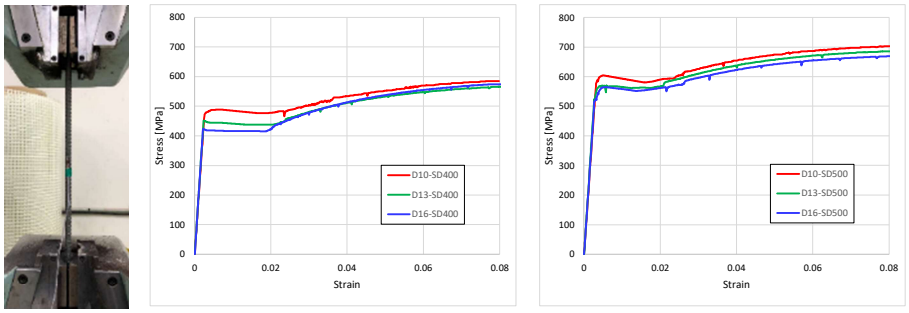

Figure 1-5 Steel re-bar uniaxial tensile test set up and corresponding stress-strain graph: batch SD400 (left graph) and batch SD500(right graph)

1.3.2 Test Set Up

In order to observe the tensile behavior of UHPFRC reinforced with various steel and GFRP rebars, a number of dog bone specimen with a cross section of 50mm × 100mm and a length of 500mm were prepared. Uniaxial tensile test was progressed with 2 LVDT displacement gauges on two sides of specimen with a measurement length 180mm for displacement measurement. The test method follows the procedure demonstrated by Park et al. [6], Yoo et al.[7]

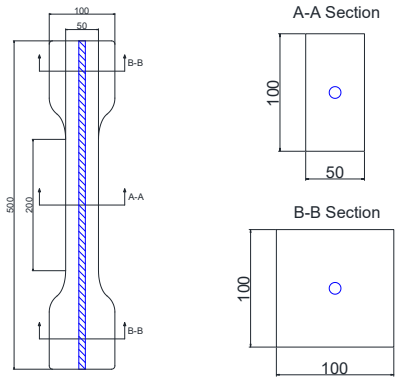

Figure 1-6 Geometry of specimen

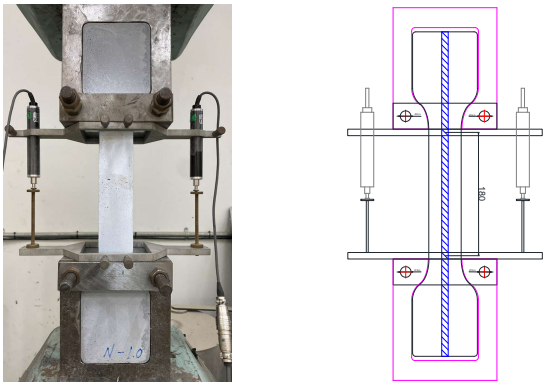

Figure 1-7 Uniaxial tensile test set up

Specimens manufactured for the tensile test were reinforced in the end part with wire mesh to prevent cracks outside of the LVDT measurement zone. There were no additional set up for GFRP re-bars to increase bond strength, while steel re-bars were installed with anchor head in the end part, since anchor head had only decreased the bond performance of GFRP re-bars.

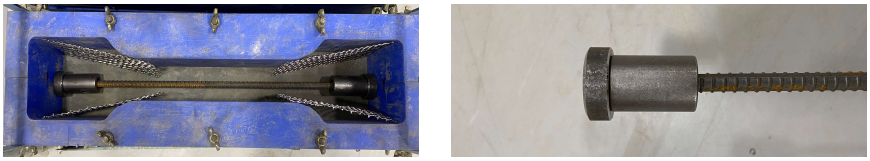

Figure 1-8 Wire mesh and achor head installed in the specimen

1.3.3 Specimen Notations

The notations and additional details for GFRP and steel reinforced UHPFRC specimens are summarized in **Table 1-4**. Each specimen is denoted as "I-II-III" which represents for "re-bar type (I): GFRP (G) or SD400 (S400) or SD500 (S500)", "re-bar diameter (II): D10(A) or D13(B) or D16(C)" and "steel fiber volume ratio (III)". As an example, S400-C-1.0 refers to R-UHPFRC specimen reinforced with D16-SD400 steel re-bar, containing 1% of steel fiber volume ratio.

Table 1-4 Details of uniaxial tensile test specimens and notations

Specimen Notations	d_s [mm]	ρ_s [%]	V_f [%]
G-A-0.0	9.53	0.0143	0.0
G-A-0.5	9.53	0.0143	0.5
G-A-1.0	9.53	0.0143	1.0
G-A-1.5	9.53	0.0143	1.5
G-A-2.0	9.53	0.0143	2.0
G-B-0.0	12.7	0.0253	0.0
G-B-0.5	12.7	0253	0.5
G-B-1.0	12.7	0.0253	1.0
G-B-1.5	12.7	0253	1.5
G-B-2.0	12.7	0.0253	2.0
G-C-0.0	15.9	0.0397	0.0
G-C-0.5	15.9	0.0397	0.5
G-C-1.0	15.9	0.0397	1.0
G-C-1.5	15.9	0.0397	1.5
G-C-2.0	15.9	0.0397	2.0
S400-A-0.0	9.53	0.0143	0.0
S400-A-1.0	9.53	0.0143	1.0

S400-A-2.0	9.53	0.0143	2.0
S400-B-0.0	12.7	0.0253	0.0
S400-B-1.0	12.7	0.0253	1.0
S400-B-2.0	12.7	0.0253	2.0
S400-C-0.0	15.9	0.0397	0.0
S400-C-1.0	15.9	0.0397	1.0
S400-C-2.0	15.9	0.0397	2.0
S500-A-0.0	9.53	0.0143	0.0
S500-A-1.0	9.53	0.0143	1.0
S500-A-2.0	9.53	0.0143	2.0
S500-B-0.0	12.7	0.0253	0.0
S500-B-1.0	12.7	0.0253	1.0
S500-B-2.0	12.7	0.0253	2.0
S500-C-0.0	15.9	0.0397	0.0
S500-C-1.0	15.9	0.0397	1.0
S500-C-2.0	15.9	0.0397	2.0

Chapter 2. Literature Review

2.1 Tension Stiffening Effect and Bond Factor

Considering the reinforced concrete tension member under tensile load, differences are found in the response between the bare re-bar and actual member. Linear elastic behavior between the concrete matrix and reinforcement is assumed to explain equilibrium of forces and compatibility of strains. At the interface of the concrete matrix and reinforcement, bond stress facilitates the interactive transfer of tensile load, which is distributed between two materials based on their individual rigidities. The phenomenon that concrete matrix contributes to sharing tensile load between cracks is called tension stiffening.

Bischoff et al. [8] evaluated tension stiffening effect by considering two methods: load sharing concept and strain approach, which are basically similar in the way that they both compare measured member response with the bare bar response.

Figure 2-1 and **Figure 2-2 (a)** shows load sharing concept, which explains how the tensile load capacity, N, of a reinforced concrete tension member is shared between the concrete matrix and re-bar both at the crack and between cracks. An equilibrium is formed with average load carried by the re-bar, $\overline{N_s}$ and average load carried by the concrete matrix, $\overline{N_c}$ for any given member strain, ε_m.

$$N = \overline{N_s} + \overline{N_c} \tag{2.1}$$

Where, the average load carried by the re-bar, $\overline{N_s}$ can be derived from the area, A_s, elastic modulus, E_s and the average re-bar strain, $\overline{\varepsilon_s}$, which is equal to the average member strain, ε_m ε_m.

$$\overline{N_s} = A_s E_s \varepsilon_m \tag{2.2}$$

Also, for given concrete area, A_c, and tensile cracking stress, f_{cr}, first crack will occur at the tensile member load, N_{cr}, when the load applied only on concrete matrix reaches the cracking load of the concrete, P_{cr}.

$$P_{cr} = A_c f_{cr} \tag{2.3}$$

After the several crack, the tensile load carried by concrete matrix, N_c is distributed between cracks, which is zero at the crack and the highest in the middle of space between two cracks, $N_{c,\max}$. Note that $N_{c,\max}$ cannot be larger than the concrete cracking load, P_{cr}. The average tensile load carried by concrete matrix, $\overline{N_c}$ can be expressed with β, which represents bond factor ($\beta = \frac{\overline{f_c}}{f_{cr}} = \frac{\overline{N_c}}{P_{cr}}$).

$$\overline{N_c} = A_c \overline{f_c} = A_c \beta f_{cr} = \beta P_{cr} \tag{2.4}$$

Figure 2-1 and **Figure 2-2 (b)** shows strain approach, which accounts for the

reduction of the bare re-bar strain response, ε_{sb} at a crack loation by tension stiffening strain value, $\Delta\varepsilon_s$. Assuming that there are no prestressing or thermal effect, the average re-bar strain, $\overline{\varepsilon_s}$ is equal to the average member strain, ε_m.

$$\varepsilon_m = \overline{\varepsilon_s} = \varepsilon_{sb} - \Delta\varepsilon_s \tag{2.5}$$

Rearranging **Eq. (2.1)**, **Eq. (2.2)** and **Eq. (2.4)** the average member strain, ε_m is expressed as following.

$$\overline{N_s} = A_s E_s \varepsilon_m = N - \beta A_c f_{cr} \tag{2.6}$$

$$\varepsilon_m = \overline{\varepsilon_s} = \frac{N}{A_s E_s} - \beta \frac{A_c f_{cr}}{A_s E_s} = \varepsilon_{sb} - \beta\Delta\varepsilon_{s,\max} \tag{2.7}$$

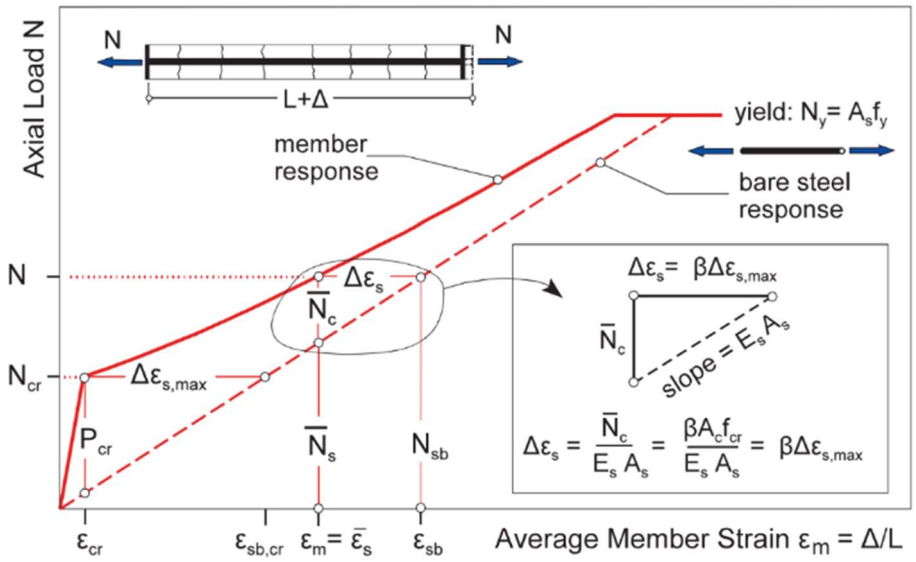

Figure 2-1 Typical response of a reinforced concrete tension member (Bischoff et al. [8])

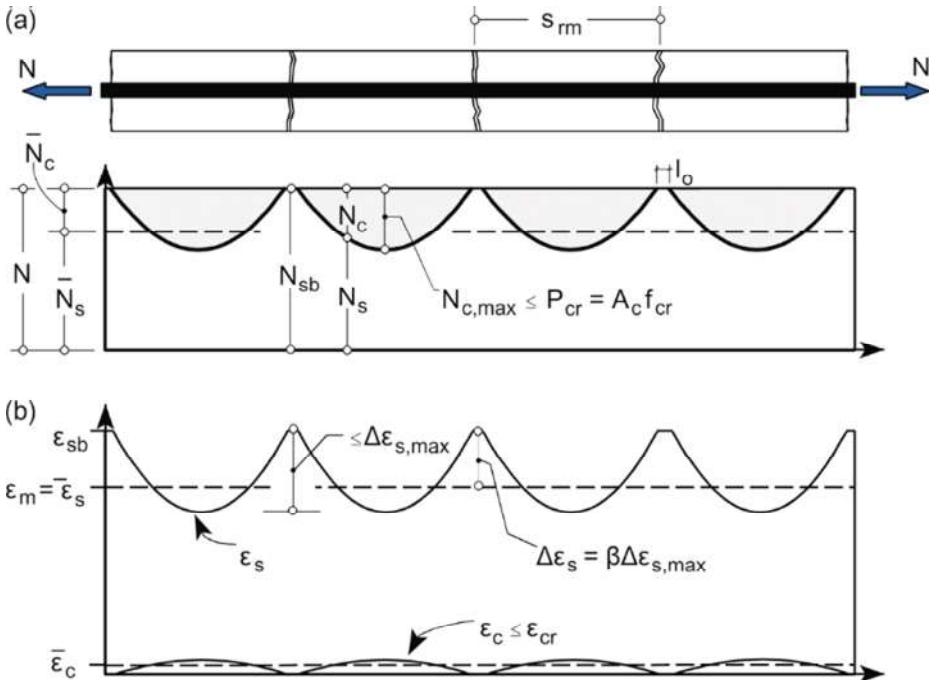

Figure 2-2 Distribution of (a) axial forces and (b) axial strains (for an average stabilized crack pattern) (Bischoff et al. [8])

The initial response of the uncracked tensile member is modeled by incorporating the free shrinkage strain of the concrete, ε_{sh} into the equation for the total concrete strain, ε_c.

$$\varepsilon_m = \varepsilon_c = \varepsilon_{cf} + \varepsilon_{sh} \tag{2.8}$$

$$\varepsilon_m = \varepsilon_s = \varepsilon_{sf} \tag{2.9}$$

ε_{cf} ($= f_c / E_c$, when before cracking) and ε_{sf} ($= f_s / E_s$, when $f_s \le f_y$) represents for strain in concrete matrix and steel caused by tensile stress respectively. Considering strain caused by stress in both concrete and steel as

well as their corresponding linear elastic stress-strain relationships, an initial shortened member strain, $\varepsilon_{m,i}$ at zero tensile load can be derived. Where, the elastic moduli, $n = \frac{E_s}{E_c}$ and the reinforcement raio, $\rho = \frac{A_s}{A_c}$.

$$N = N_c + N_s = A_c f_c + A_s f_s = A_c E_c \varepsilon_{cf} + A_s E_s \varepsilon_{sf} \tag{2.10}$$

$$\varepsilon_{m,i} = \varepsilon_{c,i} = \varepsilon_{sh} \frac{E_c A_c}{E_c A_c + E_s A_s} = \varepsilon_{sh} \frac{1}{1 + n\rho} \tag{2.11}$$

Figure 2-3 (a) and **(b)** not only shows the effects of member shortening caused by shrinkage, but also, reduction of the first cracking load. Concrete matrix is under initial tensile load due to the constraint of reinforcement in shortened member. The initial tensile load is given as following.

$$P_{sh} = E_s A_s \varepsilon_{sh} \tag{2.12}$$

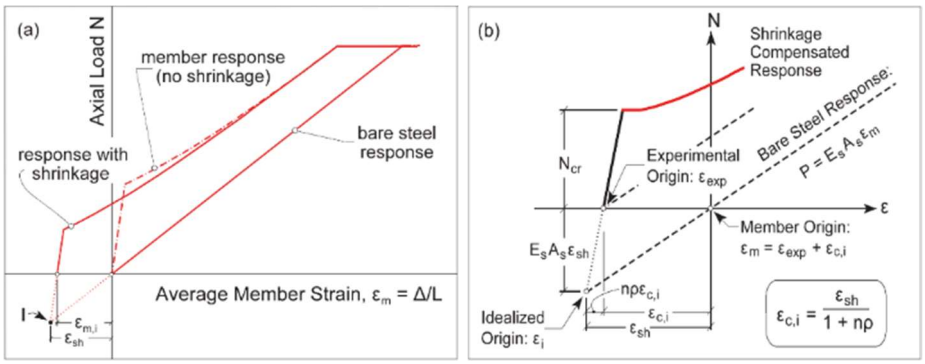

Figure 2-3 (a) Effect of shrinkage on member response and (b) details of test response and shrinkage compensated response (Bischoff et al. [8])

2.2 Shrinkage of UHPFRC Considering Reinforcement Ratio

UHPC experiences greater autogenous shrinkage than drying shrinkage, mainly because of its high cement content and low water-binder ratio. Fehling et al. [9] proposed an equation **Eq. (2.14)**, that describes the theoretical ε_{sh} - ρ_{tot} relationship. The shortening due to shrinkage, ε_{sh} was determined experimentally within test series. With the small contribution of drying shrinkage strain, the overall degree of shrinkage, $\varepsilon_{cs\infty}$ amounts to approximately 1%. (The notation ε_{sh} is used in this paper instead of $\varepsilon_{s,shr}$)

$$\rho_{tot} = \rho_s + 0.5\rho_f \tag{2.13}$$

$$\varepsilon_{sh} = \frac{\varepsilon_{cs\infty}}{1 + \alpha_E \cdot \rho_{tot} \cdot (1 + \rho \cdot \varphi)} \tag{2.14}$$

Where, φ is creep coefficient, ρ is relaxation coefficient and $\alpha_E = E_s / E_c$. **Figure 2-4** shows how the unknown parameters were determined through regression analysis based on measured values. The fiber content is considered as half the bar reinforcement ratio.

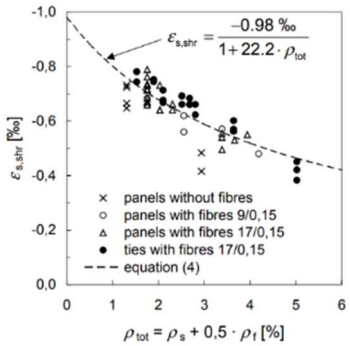

Figure 2-4 Shortening of tensile members due to shrinkage (Fehling et al. [9])

2.3 Tension Chord Model (TCM)

Bond stresses arise at the interface of steel and concrete when there are relative displacements or slip, δ between them. The magnitude of these stresses is influenced by various factors such as concrete strength, bar roughness (which includes size, shape, and spacing of ribs), bar orientation, and the state of stress in both the concrete and reinforcement, etc. Kaufmann et al. [10] demonstrated, in a simplified approach, how the average bond shear stress between re-bar with nominal diameter, ϕ and concrete matrix along the embedment length, l_b is determined from the pullout load, F, as can be seen in **Figure 2-6 (c)**.

$$\tau_b = \frac{F}{\phi \pi l_b} \tag{2.15}$$

$$\frac{d\sigma_s}{dx} = \frac{4\tau_b}{\phi}, \quad \frac{d\sigma_c}{dx} = -\frac{4\tau_b}{\phi} \cdot \frac{\rho}{(1-\rho)} \tag{2.16}$$

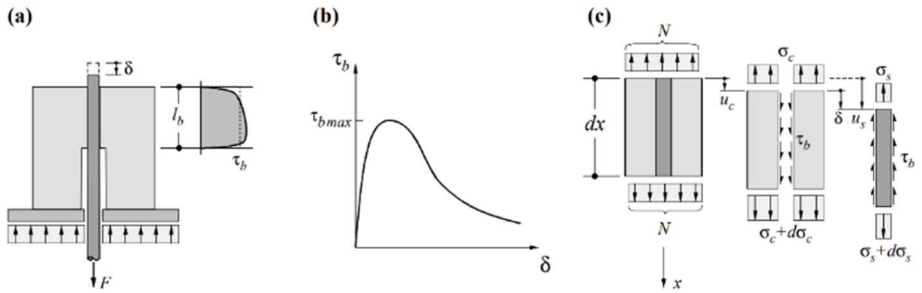

Figure 2-5 Bond behaviour (a) pull-out test, (b) bond shear stress-slip relationship and (c) differential element (Kaufmann et al. [10])

A structural concrete tension chord behavior can be described by an element that is enclosed by two adjacent cracks, as depicted in **Figure 2-7(a)**. The distribution of stresses and strains that occur within this element is illustrated in **Figure 2-7 (b)**, under the condition where equal tensile forces, N act on both sides of the element, i.e., a symmetrical case. At the cracks, the concrete experiences zero stresses while the entire tensile force is borne by the re-bar. Away from the cracks, the transfer of tensile stresses from the reinforcement to the adjacent concrete takes place through bond shear stresses. In a symmetrical scenario, the bond shear stresses and slip at the center between the cracks become zero. At this point, the reinforcement stresses are at a minimum, and the concrete stresses reach their highest value.

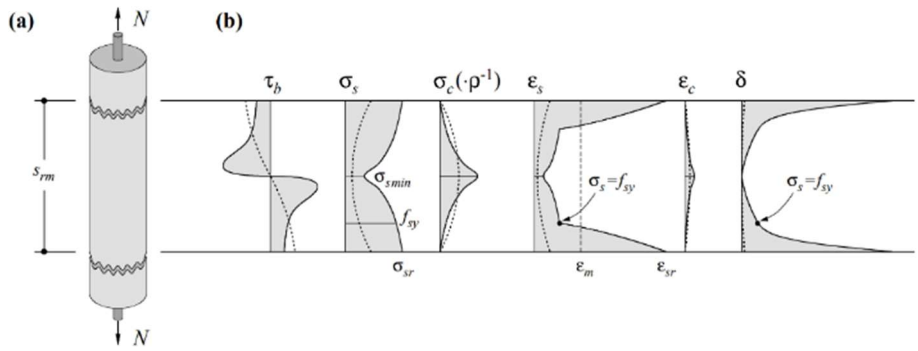

Figure 2-6 Tension stiffening (a) chord element; (b) qualitative distribution of bond shear stresses, steel and concrete stresses and strains, and bond slip (Kaufmann et al. [10])

In most cases, the overall behavior of the chord element is more important than the exact distribution of stresses and strains within it. Therefore, simple stress-strain and bond shear stress-slip relationships can be adopted, as long as

the resulting re-bar stresses and overall strains of the chord element reflect the dominant influences and match experimental data. Sigrist et al. [11] proposed using a bilinear stress-strain characteristic for the reinforcement and a stepped, rigid-perfectly plastic bond shear stress-slip relationship, as shown in **Figure 2-7 (a)** and **(b)**, for this purpose. This approach has been termed the "Tension Chord Model" [10], [11]. The bond shear stresses prior to and after yielding of the re-bar are assumed to be $\tau_{b0} = 2f_{ct}$ and $\tau_{b1} = f_{ct}$ respectively, where, f_{ct} refers to tensile strength of concrete.

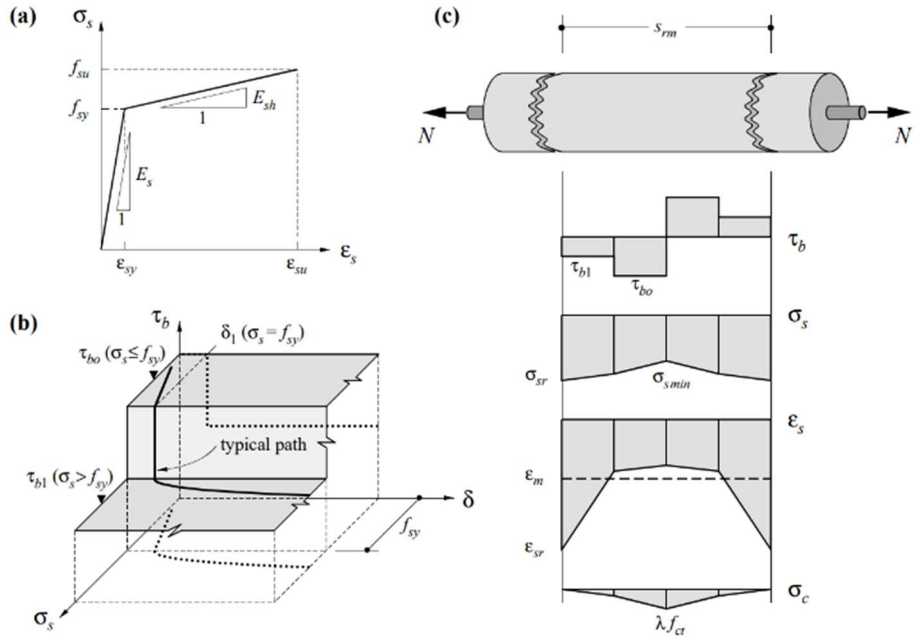

Figure 2-7 Tension chord model (a) stress-strain diagram for re-bar (b) bond shear stress-slip relationship (c) chord element and distribution of bond shear, re-bar and concrete stresses, and re-bar strains (Kaufmann et al. [10])

By considering that the concrete tensile stress cannot exceed the concrete tensile strength f_{ct}, maximum crack spacing, s_{r0} in a fully developed crack pattern follows a requirement **Eq. (2.18)**. It is important to note that the minimum crack spacing is half of the maximum crack spacing, i.e., $s_{r0}/2$, because a tensile stress equal to the concrete tensile strength must be transferred to the concrete in order to create a new crack.

$$\frac{4}{\phi}\cdot\frac{\rho}{(1-\rho)}\int_{x=0}^{s_{r0}/2}\tau_b dx \le f_{ct} \tag{2.17}$$

Resulting the crack spacing, s_{rm} in a fully developed crack pattern limited in a boundary, where $0.5 \le \lambda \le 1.0$.

$$\frac{s_{r0}}{2} \le s_{rm} \le s_{r0} \tag{2.18}$$

$$\lambda = \frac{s_{rm}}{s_{r0}} \tag{2.19}$$

The bond shear stresses drop in a sudden at the point of yielding due to the typical tensile response of re-bar. **Figure 2-7 (a)** shows the drastic change in stress-strain curve, where the strain increases at a much faster rate after yielding ($E_s \ge E_{sh}$). Larger strains and slips result in significantly lower bond shear stresses, **Figure 2-7 (b)**. By utilizing the stepped rigid-perfectly plastic bond shear stress-slip relationship within the tension chord model, numerous problems can be approached analytically. Notably, it is possible to ascertain the distribution of bond shear, re-bar and concrete stresses, and strains, as depicted in **Figure 2-7 (c)**, for any assumed maximum re-bar stress at the crack. This is

accomplished through the establishment of constant bond shear stresses that correspond to linear fluctuations of re-bar and concrete stresses, as denoted in **Eq. (2.17)**. The maximum crack spacing can be expressed as

$$s_{r0} = \frac{f_{ct}\phi}{2\tau_{b0}} \cdot \frac{(1-\rho)}{\rho} \tag{2.20}$$

and the maximum re-bar stress at the cracked section, denoted as $\sigma_{s,r}$, can be obtained through a function of the average member strain, denoted as ε_m, which pertains to the overall deformation. For re-bar stresses below re-bar yield strength, f_{sy} along the entire chord element, $\sigma_{sr} \le f_{sy}$, the maximum re-bar stress is expressed as

$$\sigma_{s,r} = E_s\varepsilon_m + \frac{\tau_{b0}s_{rm}}{\phi} \tag{2.21}$$

As for re-bar stresses partially above and partially under re-bar yield strength, f_{sy}, $\sigma_{s,\min} \le f_{sy} \le \sigma_{s,r}$

$$\sigma_{s,r} = f_{sy} + 2\frac{\frac{\tau_{b0}s_{rm}}{\phi} + \sqrt{\left(f_{sy} + E_s\varepsilon_m\right)\frac{\tau_{b1}s_{rm}}{\phi}\left(\frac{\tau_{b0}}{\tau_{b1}} - \frac{E_s}{E_{sh}}\right) + \frac{E_s}{E_{sh}}\tau_{b0}\tau_{b1}\frac{s_{rm}^2}{\phi^2}}}{\frac{\tau_{b0}}{\tau_{b1}} - \frac{E_s}{E_{sh}}} \tag{2.22}$$

Finally, for re-bar stresses partially above re-bar yield strength, f_{sy} along the entire chord element, $f_{sy} \le \sigma_{s,\min}$

$$\sigma_{s,r} = f_{sy} + E_{sh}\left(\varepsilon_m - \frac{f_{sy}}{E_s}\right) + \frac{\tau_{b1}s_{rm}}{\phi} \tag{2.23}$$

2.4 Modified Tension Chord Model for R-UHPFRC

SFRC members cannot be analyzed at a single discrete cross-section due to the influence of fiber stresses on crack opening, which is unlike RC members. The tension chord model (TCM) is a mechanically consistent tool developed by Marti et al. [11] that can be utilized to model the load-deformation behavior of structural concrete members with uniaxial stress states, including tension ties and tension chords in one-way bending members. TCM assumes a stepped, rigid-perfectly plastic bond shear stress-slip relationship to model the interaction between the reinforcing bar and concrete between cracks in cracked tension chords (Marti et al. [12]), defining the stress state at any point between two cracks in a tension chord, without the need for iterative solutions of the second order differential equation of bond.

The residual tensile strength, or postcracking behavior, is the primary consideration when designing structural concrete that incorporates steel fibers. Unlike plain concrete which has a stress-strain response in tension approximately linear before cracking at the material level, the behavior of steel fiber-reinforced concrete (SFRC) after cracking can be best characterized by its nominal stress versus crack-opening displacement $\sigma - w$ relationship.

Marki´c et al. [13] demonstrated a model that simplifies the stress-strain relationship for softening SFRC. By using residual postcracking tensile stresses, $f_{0.5}$ and $f_{1.5}$ at correstponding crack-opening displacement, $COD_1 = 0.5mm$ and $COD_2 = 1.5mm$, crack width at which the fibers carry zero stresses, l_{fu} is extrapolated. Modeled behavior of softening SFRC is

shown in **Figure 2-8**.

$$l_{fu} = \frac{1}{1 - \frac{f_{1.5}}{f_{0.5}}}\left(COD_2 - COD_1\right) + COD_1 \tag{2.24}$$

The residual tensile strength, σ_{cf} delivered by steel fiber for crack width, w may be expressed as following.

$$\sigma_{cf} = \begin{cases} f_{0.5}\dfrac{l_{fu} - w}{l_{fu} - COD_1} & \left(0 \le w \le l_{fu}\right) \\ 0 & \left(w > l_{fu}\right) \end{cases} \tag{2.25}$$

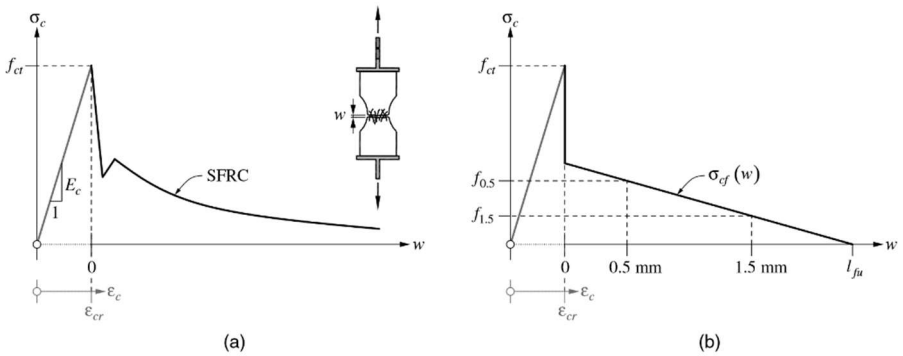

Figure 2-8 Stress-strain/crack width relationship for softening SFRC (a) actual behavior and (b) modeled behavior (Markić et al. [13])

The maximum crack spacing, s_{r0} for UHPFRC as well as SFRC tension tie can be expressed as a function of bond stress between the concrete matrix and re-bar, τ_b , assuming that onset of crack occurs when maximum concrete

matrix stress, $\sigma_{c,cl}$ reaches concrete matrix tensile strength, f_{ct}, (Markić et al. [13] and Valente et al. [14]). Where, $\sigma_{cf,cr}$ indicates stress carried by fiber at cracking load.

$$s_{r0} = \frac{\phi f_{ct}(1-\rho_s)}{2\tau_{b0}\rho_s}\left(1-\frac{\sigma_{cf,cr}}{f_{ct}}\right) \tag{2.26}$$

Since $\sigma_{cf,cr}$ is a function of the crack width w_{cr}, crack width and cracking space are interdependent.

$$w_{cr} = \frac{\tau_{b0}s_{r0}^2}{\phi_s E_s}\left(1+\frac{\rho_s}{1-\rho_s}\right) \tag{2.27}$$

The total resistance of the tension tie can be expressed in terms of stresses by both the reinforcing bars and fibers according to the location of tension chord element.

$$\sigma_N = \rho_s\sigma_{s,r} + (1-\rho_s)\sigma_{cf} = \rho_s\sigma_{s,cl} + (1-\rho_s)\sigma_{c,cl} \tag{2.28}$$

Where, σ_N, $\sigma_{s,r}$, σ_{cf}, $\sigma_{s,cl}$, $\sigma_{c,cl}$ refers to axial load normalized to $A = 1\,m^2$, stress carried by re-bar at cracked section, stress carried by fiber at cracked section, stress carried by re-bar at the center of two adjacent cracks, stress carried by concrete matrix at the center of two adjacent cracks, respectively.

2.5 Bond Stress and Slip Response of GFRP Re-bar in UHPFRC

The cracking behavior of reinforced concrete structures under tension is primarily determined by the bond between the rebar and the concrete. As most structural concerns are addressed at the serviceability level, it is crucial to develop an appropriate bond stress and slip model for the ascending branch in order to accurately predict the cracking behavior. According to Yoo et al. [15], CMR model in **Eq. (2.29)** proposed by Cosenza et al. [16] is suitable for predicting the local bond stress and slip response of GFRP re-bar in UHPFRC.

$$\frac{\tau}{\tau_{\max}} = \left(1 - e^{-s/s_r}\right)^{\beta} \tag{2.29}$$

Where, τ is the bond stress, s is the slip and s_r and β are both the curve fitting coefficients.

Chapter 3. Global Behavior in Uniaxial Tension

3.1 Introduction

This chapter focuses on the global behavior of specimens under uniaxial tension. A total of 33 specimens with different variables were subjected to uniaxial tensile tests until failure to analyze both elastic and plastic behavior.

The load-strain relationships for the specimens in both elastic and plastic states were compared with the behavior of bare re-bars under different variables. When in the elastic state, the focus is on the member cracking load, while in the plastic state, the emphasis is on the type of re-bar failure and ultimate load for comparative analysis.

Actual test results are presented in photographs for the better illustration of crack formation and re-bar failure types. The focus is on identifying the cracking patterns according to steel fiber volume ratio and re-bar diameter. Using the model described in Section 2.2.4, the modeled tensile behavior of the N-series specimens, theoretical crack spacing and crack width are derived and compared with the actual results. Furthermore, in order to compare the interaction between re-bars and UHPFRC with that of normal reinforced concrete (NRC), the material properties of NRC were input into the model to calculate crack width and crack spacing for comparison.

3.2 Applied Load and Corresponding Member Strain

To ensure a fair comparison between GFRP and steel re-bars, the strain range for elastic and plastic states differs due to the different modulus of elasticity. The stress for bare re-bars is obtained by dividing the load of the bare re-bar by the cross-sectional area of the member ($A_c = 5000mm^2$) to enable a better comparison with member stress. Also, for better comparison between the response of bare re-bar and member, load-strain curve is used instead of stress-strain curve.

3.2.1 Tensile Behavior in Elastic State

The overall results in the elastic state indicate that as the steel fiber volume ratio increases and re-bar diameter decreases, it is more likely to observe that the load beared by the member exceeds bare re-bar strength. As the re-bar diameter increases and the steel fiber volume ratio decreases, the bond strength between UHPFRC and re-bar increases, causing more slip to occur. This leads to the measured displacement being greater than the actual displacement of the re-bar.

The point where the load-strain curve first shows a sudden bend is the point at which the initial crack occurs. The load at this point is the initial cracking load of the tensile member, and it can be visually observed and compared for each member. **Figures 3-1, 3-2**, and **3-3** show the overall behavior of specimens with GFRP, SD400, and SD500 steel re-bars, respectively, in the elastic state. The initial cracking load of the tensile member tends to increase with an increase in the steel fiber volume ratio, and a decrease in the diameter and

modulus of elasticity of the re-bar. Chapter 4 will provide a more detailed discussion on the initial cracking load.

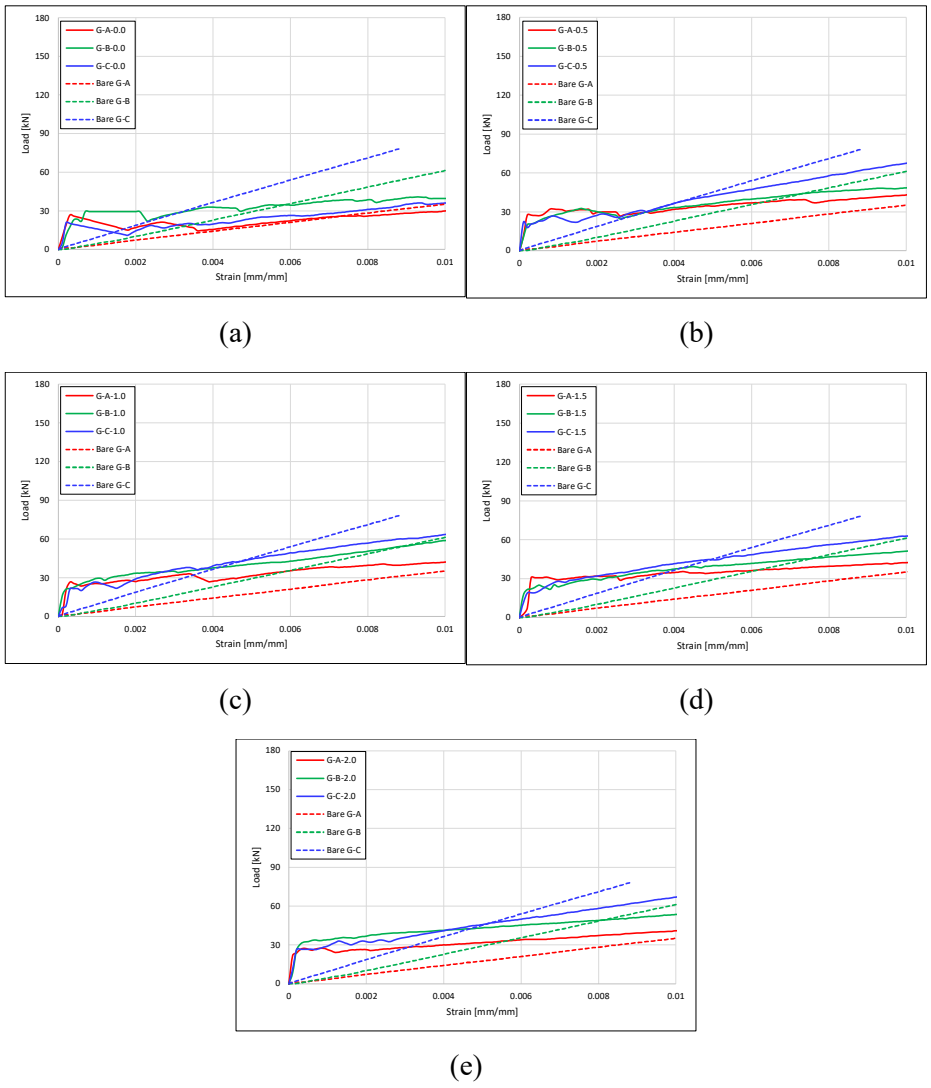

Figure 3-1 Global behavior of specimens with GFRP re-bars in elastic state, steel fiber volume ratio: (a) 0.0% (b) 0.5% (c) 1.0% (d) 1.5% (e) 2.0%

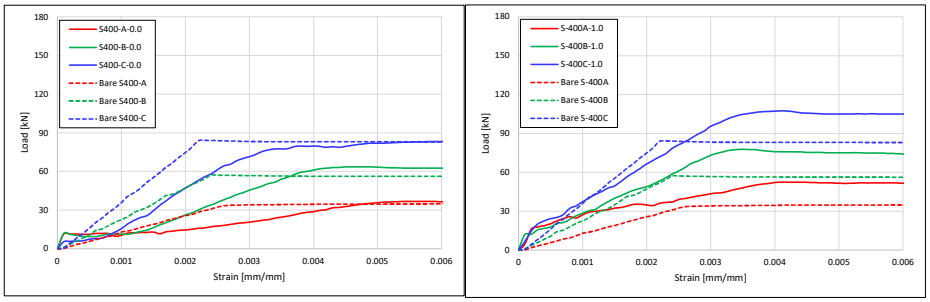

(a) (b)

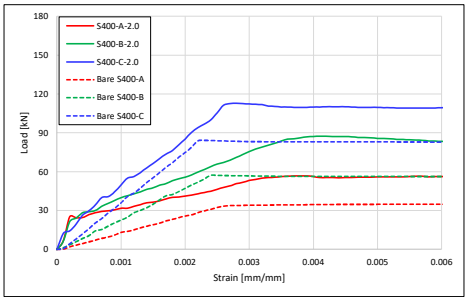

(c)

Figure 3-2 Global behavior of specimens with SD400 steel re-bars in elastic state, steel fiber volume ratio: (a) 0.0% (b) 1.0% (c) 2.0%

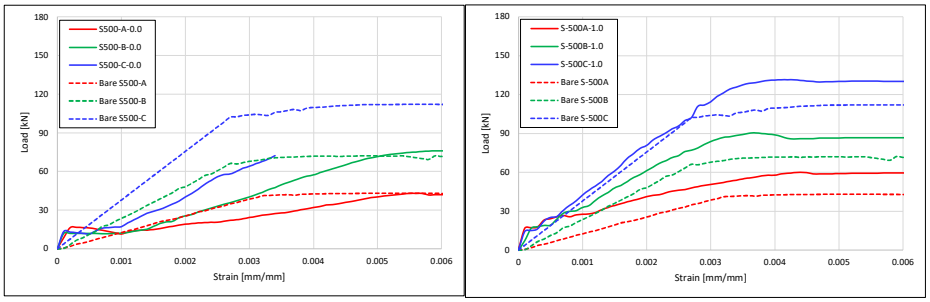

(a) (b)

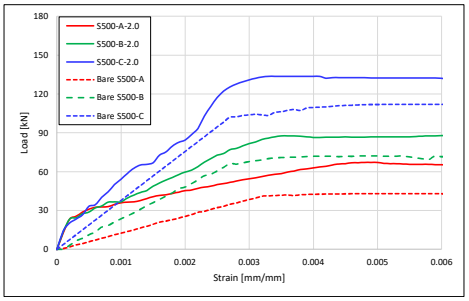

(c)

Figure 3-3 Global behavior of specimens with SD500 steel re-bars in elastic state, steel fiber volume ratio: (a) 0.0% (b) 1.0% (c) 2.0%

3.2.2 Tensile Behavior in Plastic State

Different variables can cause different types of re-bar failure, either pull-out or rupture, which lead to different patterns in the corresponding ultimate load. **Figures 3-4, 3-6** and **3-8** illustrate global behavior of specimens with GFRP, SD400 and SD500 steel re-bars in plastic state respectively. In the figure, the re-bar failure type is denoted by the letter "R" for rupture and "P" for pull-out.

In GFRP re-bar series, when pull-out occurs, the ultimate tensile load increases as the steel fiber volume ratio increases due to the improvement of the bond strength between UHPFRC and the re-bar. On the otherhand, it can be observed that the ultimate tensile load is limited to the tensile strength of the re-bar when the bond strength is sufficient to prevent slip and cause re-bar rupture as can be seen in series G10. This means that the ultimate tensile load does not increase beyond the tensile strength of the re-bar. Also, the ultimate tensile load increases as the reinforcement ratio increases, but the attachment area to the UHPFRC matrix is not proportional to the reinforcement ratio, resulting in an increase in slip due to a decrease in bond strength. The overall ultimate tensile loads of specimens reinforced with GFRP re-bars is depicted in **Figure 3-5**.

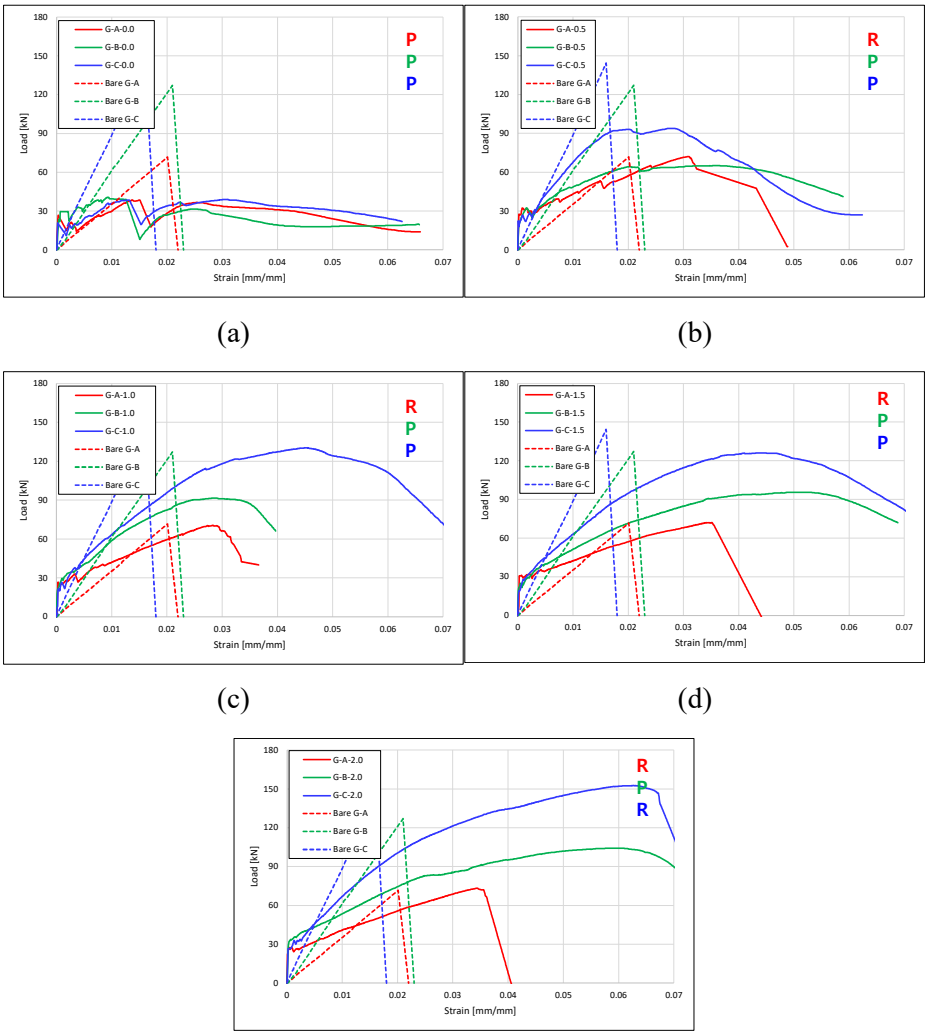

Figure 3-4 Global behavior of specimens with GFRP re-bars in plastic state, steel fiber volume ratio: (a) 0.0% (b) 0.5% (c) 1.0% (d) 1.5% (e) 2.0%

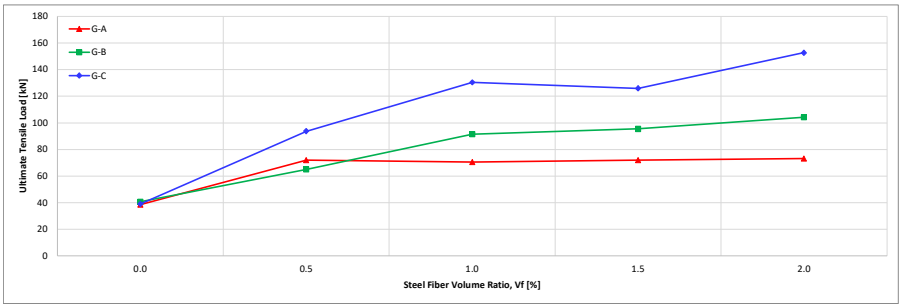

Figure 3-5 Ultimate tensile loads of specimens with GFRP re-bars

The anchor head installed at the end of each re-bar in SD400 steel re-bar series prevents pull-out failure. However, in the case of S400C-0.0, the entire anchor head was pulled out, leading to a failure. In the SD400 series with 0.0% steel fiber volume ratio, the ultimate tensile load of S400C-0.0 did not surpass the bare re-bar tensile strength because of the pull-out, while the ultimate tensile load of S400A-0.0 and S400B-0.0 reached the bare re-bar tensile strength since no pull-out failure occurred. The increase in steel fiber volume ratio increased the ultimate tensile load. The localization of cracks around a single major crack is causes the concentration of stress distribution on the corresponding part of the re-bar, leading to failure at a smaller strain. In both the 1.0% and 2.0% series, it was observed that specimens reinforced with D10 re-bar experienced rupture at a smaller strain compared to bare re-bar. However, D13 and D16 re-bar series did not show this behavior, likely due to a lack of bond stress. The ultimate tensile load exceeds the re-bar tensile strength in all series except for the steel fiber volume ratio 0.0% series, as shown in **Figure 3-7**, due to the contribution of the UHPFRC matrix.

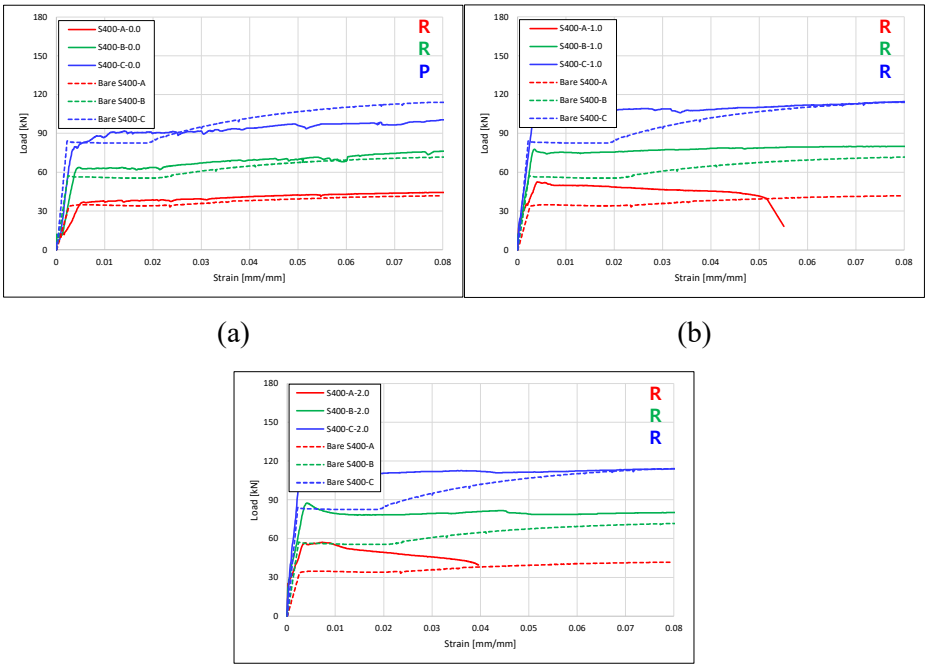

Figure 3-6 Global behavior of specimens with SD400 steel re-bars in plastic state, steel fiber volume ratio: (a) 0.0% (b) 1.0% (c) 2.0%

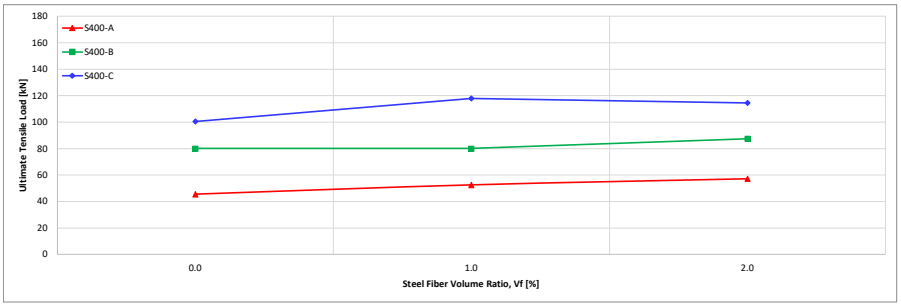

Figure 3-7 Ultimate tensile loads of specimens with SD400 steel re-bars

The failure types observed in the SD500 series are similar to those of SD400 series. Except for the steel fiber volume ratio 0.0% series, all the specimens faced earlier rupture of re-bar due to the localization of cracks. The ultimate tensile load exceeds the re-bar tensile strength in all series except for the steel fiber volume ratio 0.0% series, as shown in **Figure 3-9**, due to the contribution of the UHPFRC matrix.

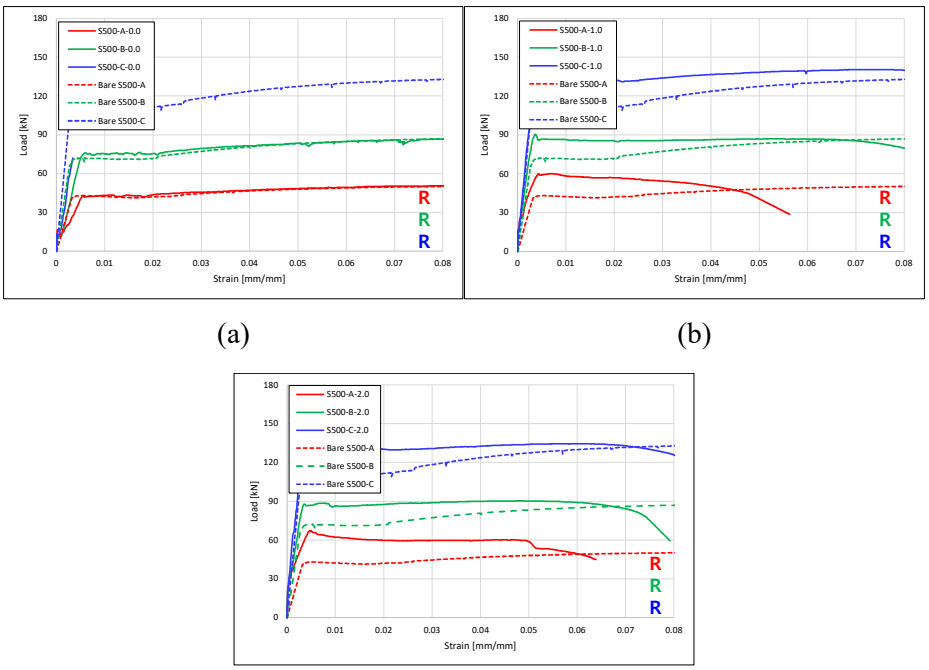

Figure 3-8 Global behavior of specimens with SD500 steel re-bars in plastic state, steel fiber volume ratio: (a) 0.0% (b) 1.0% (c) 2.0%

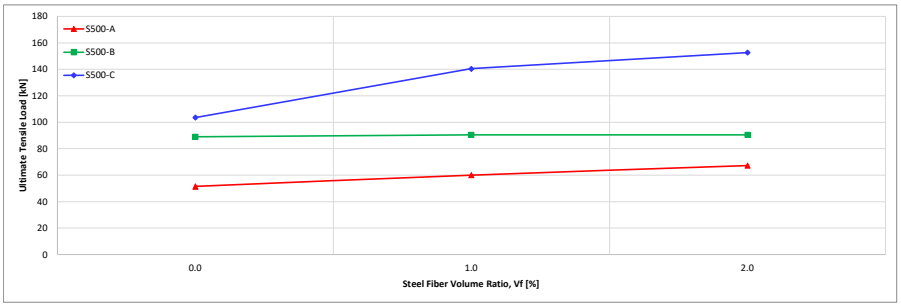

Figure 3-9 Ultimate tensile loads of specimens with SD500 steel re-bars

3.3 Cracking Patterns

In this study, a model for stress-crack opening displacement relationship demonstrated by Marki´c et al. [13] was used for deriving crack width, crack spacing. The model is described in section 2.2.4. Theoretical result values were then compared to experimental result values.

3.3.1 Actual Crack Formations

The following are the results on the crack patterns according to the steel fiber ratio, classified by the reinforcing bar ratio.

In the case of using D10 re-bars, a relatively even distribution of cracks and large splitting cracks were observed as the steel fiber ratio decreased, while micro cracks localized around the main crack and smaller splitting cracks were observed as the steel fiber ratio increased. **Figure 3-10, 3-11** and **3-12** show the crack formation of specimens reinforced with D10 GFRP, SD400 and SD500 re-bar respectively from actual tensile test. There were not significant differences observed in the cracking patterns by varying the steel fiber volume ratio, when the re-bar type was changed.

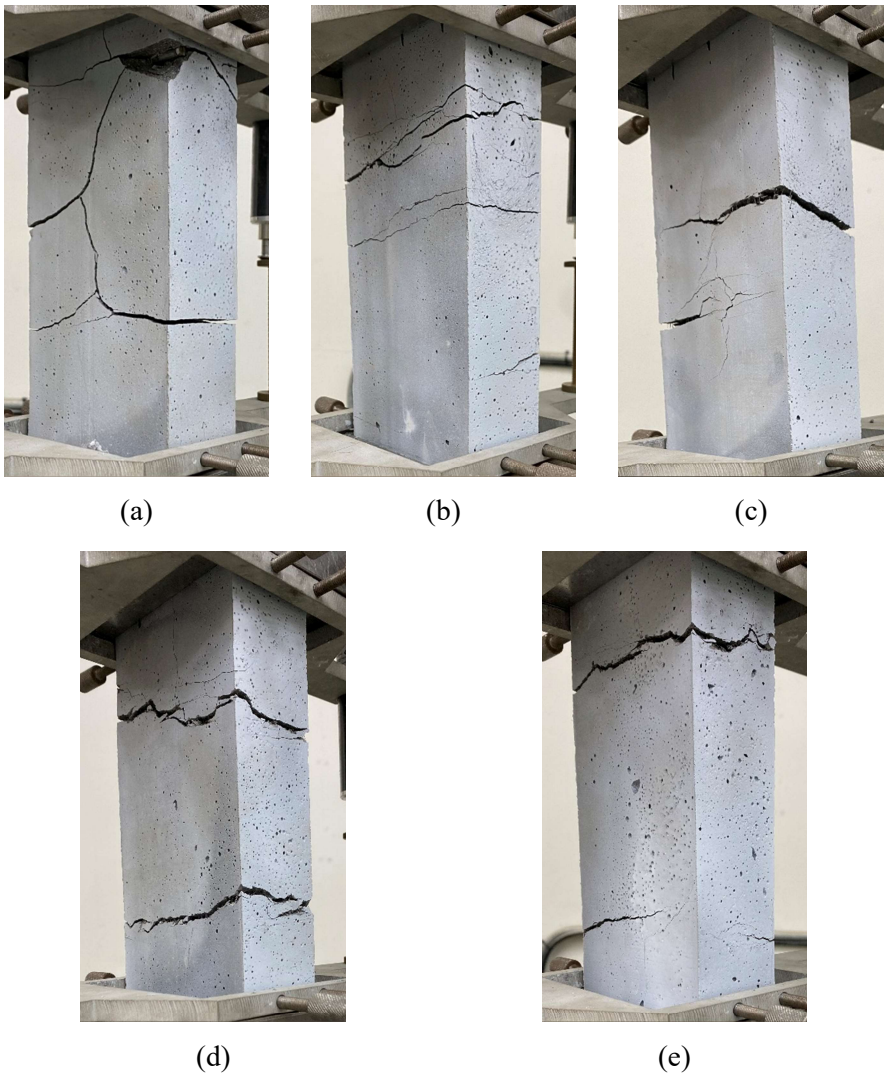

(a) (b) (c)

(d) (e)

Figure 3-10 Cracking patterns of specimens with D10 GFRP re-bars, steel fiber volume ratio: (a) 0.0% (b) 0.5% (c) 1.0% (d) 1.5% (e) 2.0%

(a) (b) (c)

Figure 3-11 Cracking patterns of specimens with D10 SD400 steel re-bars, steel fiber volume ratio: (a) 0.0% (b) 1.0% (c) 2.0%

(a) (b) (c)

Figure 3-12 Cracking patterns of specimens with D10 SD500 steel re-bars, steel fiber volume ratio: (a) 0.0% (b) 1.0% (c) 2.0%

In the case of using D13 re-bars, a relatively even distribution of cracks was also observed as the steel fiber ratio decreased, and localizing of fine cracks around the main crack was observed as the steel fiber ratio increased. Additionally, larger splitting cracks were observed compared to those in the case of using D10 re-bars, as the thickness of the cover decreased. **Figure 3-13**, 3-14 and 3-15 show the crack formation of specimens reinforced with D13 GFRP, SD400 and SD500 re-bar respectively from actual tensile test. Compared to specimens reinforced with GFRP re-bars, SD400 and SD500 serieses showed more microcracks.

(a) (b) (c)

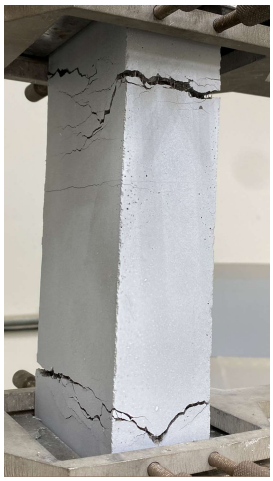

(d)

(e)

Figure 3-13 Cracking patterns of specimens with D13 GFRP re-bars, steel fiber volume ratio: (a) 0.0% (b) 0.5% (c) 1.0% (d) 1.5% (e) 2.0%

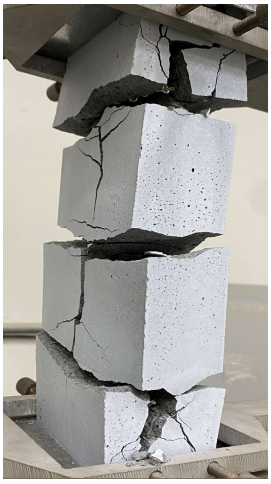

(a)

(b)

(c)

Figure 3-14 Cracking patterns of specimens with D13 SD400 steel re-bars, steel fiber volume ratio: (a) 0.0% (b) 1.0% (c) 2.0%

(a) (b) (c)

Figure 3-15 Cracking patterns of specimens with D13 SD500 steel re-bars, steel fiber volume ratio: (a) 0.0% (b) 1.0% (c) 2.0%

Lastly, in the case of using D16 re-bars, it was observed similar to that in the case of using D13, and more micro cracks and larger splitting cracks were observed as the thickness of the cover decreased compared to those in the case of using D13. **Figure 3-16**, **3-17** and **3-18** show the crack formation of specimens reinforced with D16 GFRP, SD400 and SD500 re-bar respectively from actual tensile test. Additionally, it is noteworthy that the SD400 series exhibited more significant splitting cracks in comparison to the SD500 series.

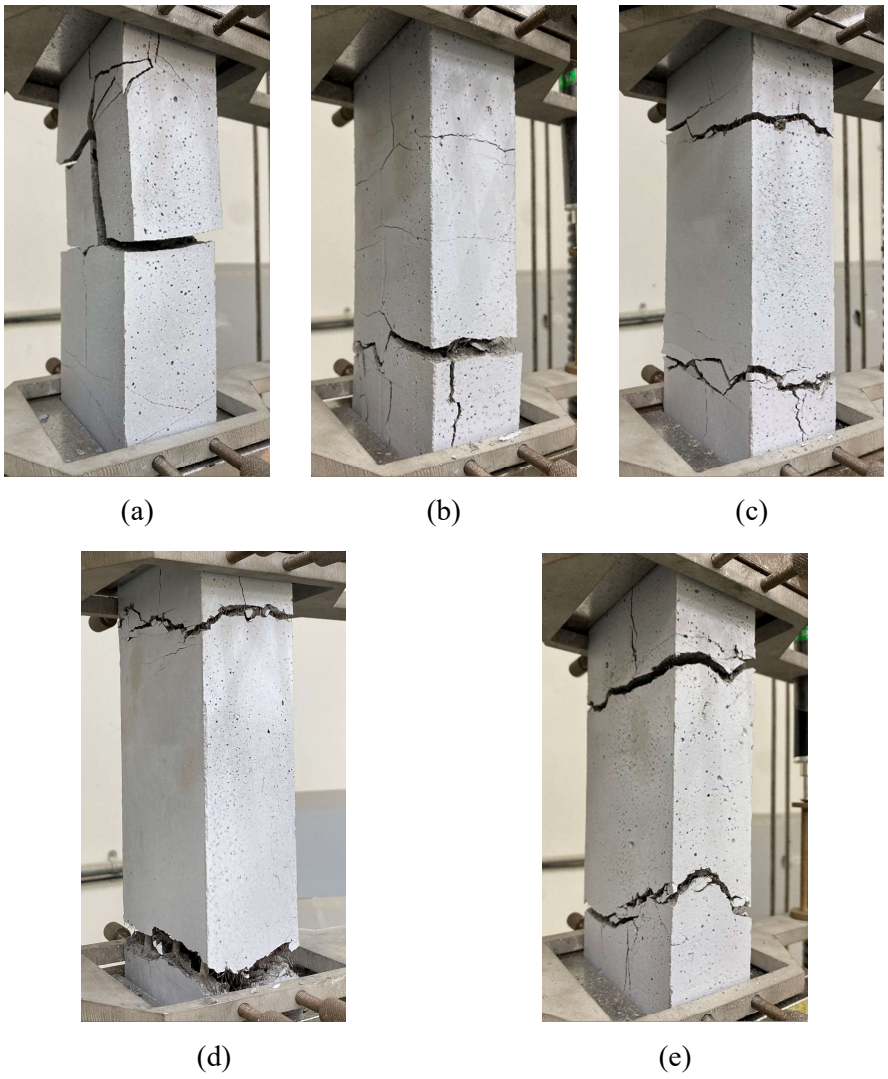

(a) (b) (c)

(d) (e)

Figure 3-16 Cracking patterns of specimens with D16 GFRP re-bars, steel fiber volume ratio: (a) 0.0% (b) 0.5% (c) 1.0% (d) 1.5% (e) 2.0%

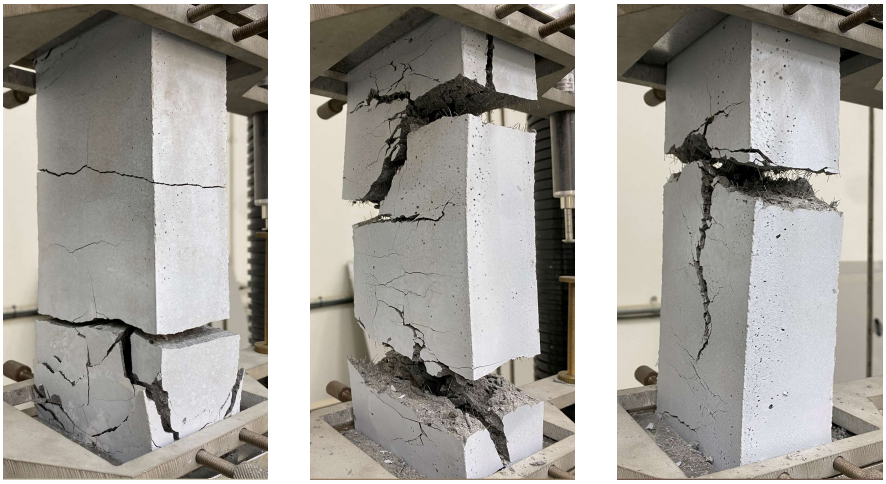

(a) (b) (c)

Figure 3-17 Cracking patterns of specimens with D16 SD400 steel re-bars, steel fiber volume ratio: (a) 0.0% (b) 1.0% (c) 2.0%

(a) (b) (c)

Figure 3-18 Cracking patterns of specimens with D16 SD500 steel re-bars, steel fiber volume ratio: (a) 0.0% (b) 1.0% (c) 2.0%

3.3.2 Modeled Behavior of Cracks

The model proposed by Marki´c et al. [13] showed in **Figure 2-8** is modified using fracture energy concept proposed by Hillerborg et al. [17], [18] for better fitting in this study with several assumptions below. As can be seen in **Figure 3-19**, both actual and modeled UHPFRC stresses, σ_c are expressed in terms of member tensile strain, ε_m.

1. Modeled behavior is derived by assuming the total fracture energy density (energy by unit of volume), $W_{M,tot}$ from the modeled tensile behavior is the same as that from actual tensile behavior of UHPFRC, $W_{A,tot}$.

$$W_{M,tot} = W_{A,tot} \tag{3.1}$$

2. Since only a single crack occurred for each N-series specimen, $\varepsilon_m = \frac{w}{l_{LVDT}}$ is assumed, where w is crack width and l_{LVDT} is the measurement length between two LVDTs ($=180mm$).

3. The crack opening at which steel fibers carry zero tensile stress (complete extraction of steel fibers), w_{fu} is assumed as $\frac{l_f}{2} = 6.5mm$, where l_f is steel fiber length, Pfyl et al. [19]. By assumption 2, the corresponding member strain at which steel fibers carry zero tensile stress, $\varepsilon_{fu} = 0.036$.

The total amount of fracture energy density, W_{tot} is the area below the measured stress-strain curve, **Eq. (3.2)**, where $\varepsilon_{\max}$ is maximum tensile strain where fibers carry zero tensile stress. The area below both modeled and actual behavior curves can be derived by integrating corresponding stress-strain curve. The total fracture energy density, $W_{M,tot}$ from the modeled tensile behavior can be devided into two parts, the energy density before the crack, $W_{M,b,cr}$ and the energy density after the crack, $W_{M,a,cr}$, **Eq. (3.3)**.

$$W_{tot} = \int_0^{\varepsilon_{\max}} \sigma_c d\varepsilon \tag{3.2}$$

$$W_{M,tot} = W_{M,b,cr} + W_{M,a,cr} = \int_0^{\varepsilon_{cr}} \sigma_{c,M} d\varepsilon + \int_{\varepsilon_{cr}}^{\varepsilon_{fu}} \sigma_{c,M} d\varepsilon \tag{3.3}$$

The modeled behavior indicates the UHPFRC cracking stress and the residual tensile strength provided by the fibers, σ_{cf}, as well as the fiber contribution in tension immediately after the crack, $\sigma_{cf,cr}$. Since, the modeled behavior is in triangular shape, it is convenient to calculate $\sigma_{cf,cr}$, once the total energy density of actual tensile behavior of UHPFRC, $W_{A,tot}$ is derived, **Eq. (3.4) ~ (3.6)**.

$$W_{M,b,cr} = \int_0^{\varepsilon_{cr}} \sigma_{c,M} d\varepsilon = \frac{f_{ct}\varepsilon_{cr}}{2} \tag{3.4}$$

$$W_{M,a,cr} = \frac{\sigma_{cf,cr}\left(\varepsilon_{fu} - \varepsilon_{cr}\right)}{2} \tag{3.5}$$

$$\sigma_{cf,cr} = \frac{2\left(W_{A,tot} - W_{M,b,cr}\right)}{\varepsilon_{fu} - \varepsilon_{cr}} \tag{3.6}$$

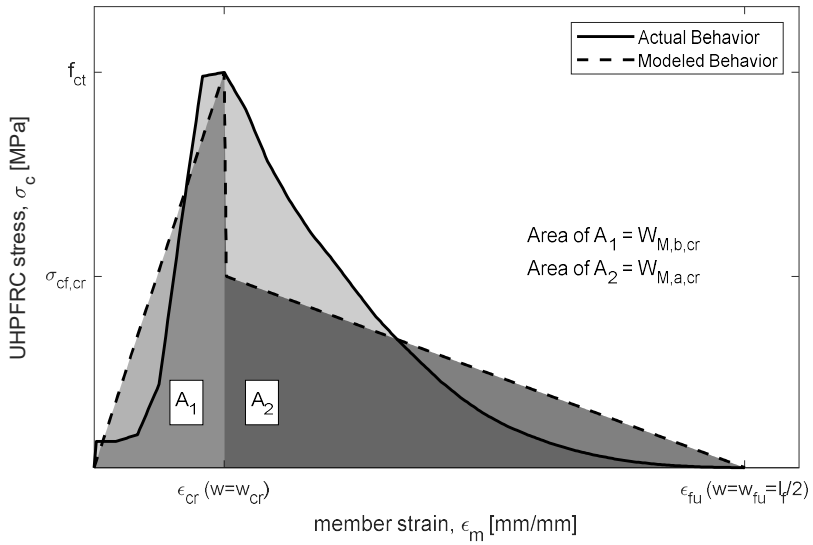

Figure 3-19 Modeled tensile behavior of UHPFRC by fracture energy

Figure 3-20 (a) and **(b)** display the actual N-series UHPFRC uniaxial tensile stress-strain behavior and its corresponding modeled behavior, which is represented by a straight line.

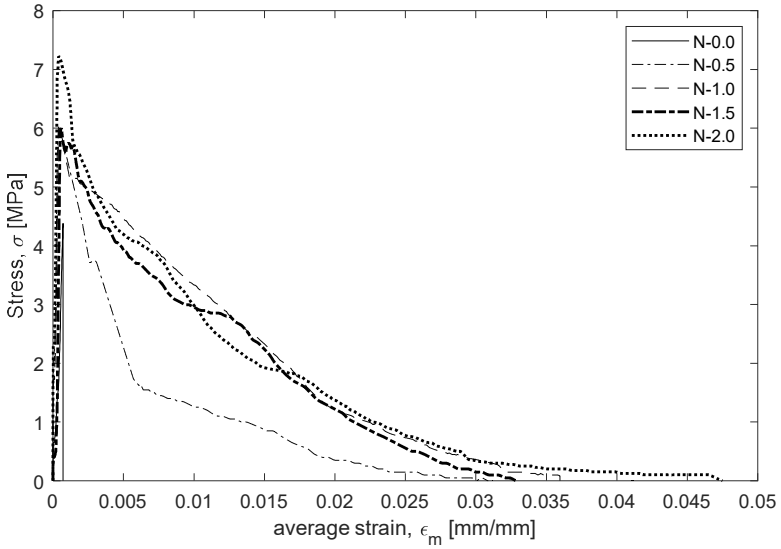

(a)

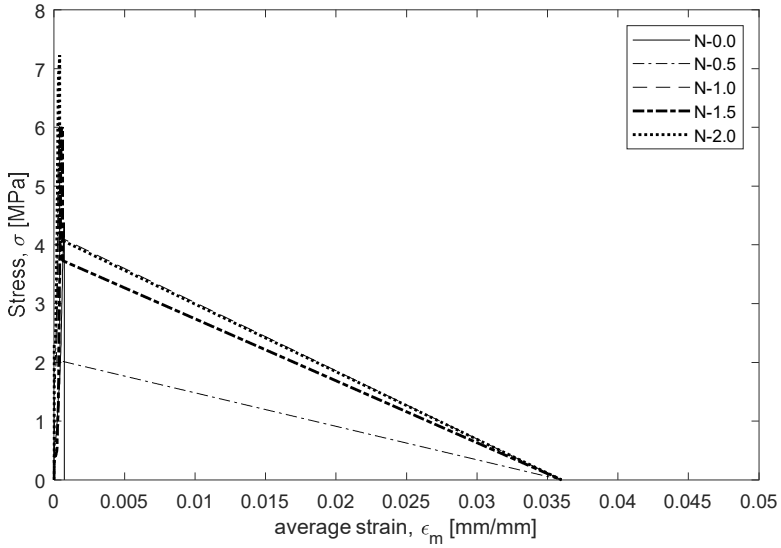

(b)

Figure 3-20 (a) N-series UHPFRC uniaxial tensile stress-strain behavior (b) Corresponding modeled behavior

The maximum crack spacing, s_{r0} is derived by **Eq. 2.26**. The term $\left(1-\frac{\sigma_{cf,cr}}{f_{ct}}\right)$ in **Eq. 2.26** causes a reduction in the maximum crack spacing due to an increase in the fiber contribution in tension immediately after the crack, $\sigma_{cf,cr}$. The bond stress, τ_{b0} used in this equation followed **Eq. 5.2** in section 5.3.1 for GFRP re-bar and **Eq. 5.11** in section 5.3.2 conventional Tension Chord Model for steel re-bar respectively. **Figure 3-21 (a), (b)** and **(c)** show the average crack spacing, s_{rm} of specimens reinforced with GFRP, SD400 and SD500 re-bar by the steel fiber volume ratio. The crack spacing, i.e. crack element length is greater in specimens reinforced with smaller diameter re-bars and steel fiber volume ratio less than 1.0%. There is no difference between SD400 and SD500 steel re-bar since the same bond stresses, $\tau_{b0}=f_{ct}$ were used. However, the crack spacing for GFRP re-bar is larger due to lower bond stress, τ_{b0} compared to steel re-bars. The crack spacing is set to be larger than at least steel fiber length, l_f which is $13mm$. Since NRC is not containing steel fiber, UHPC which refers to UHPFRC with 0% of steel fiber volume ratio is mainly compared. For GFRP re-bar reinforced UHPC, crack spacing is larger than NRC, while steel re-bar reinforced UHPC has smaller crack spacing than NRC.

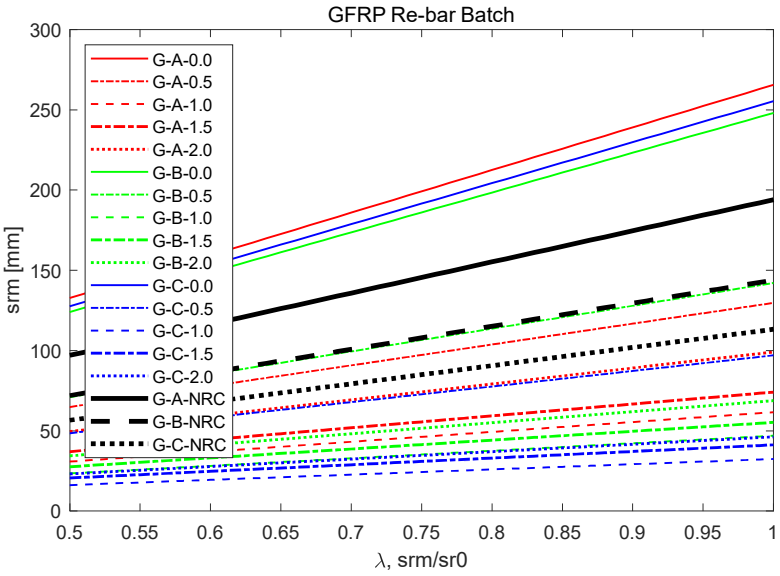
GFRP Re-bar Batch
srm [mm]
λ, srm/sr0
G-A-0.0
G-A-0.5
G-A-1.0
G-A-1.5
G-A-2.0
G-B-0.0
G-B-0.5
G-B-1.0
G-B-1.5
G-B-2.0
G-C-0.0
G-C-0.5
G-C-1.0
G-C-1.5
G-C-2.0
G-A-NRC
G-B-NRC
G-C-NRC

(a)

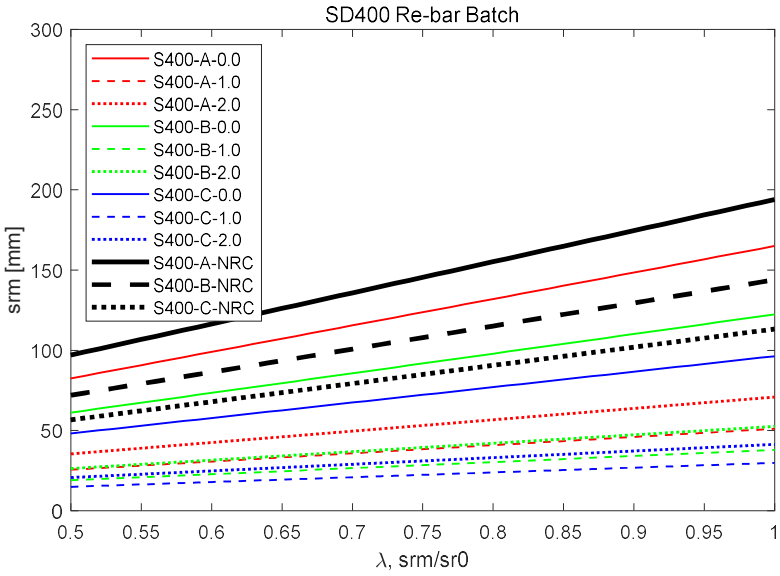
SD400 Re-bar Batch
srm [mm]
λ, srm/sr0
S400-A-0.0
S400-A-1.0
S400-A-2.0
S400-B-0.0
S400-B-1.0
S400-B-2.0
S400-C-0.0
S400-C-1.0
S400-C-2.0
S400-A-NRC
S400-B-NRC
S400-C-NRC

(b)

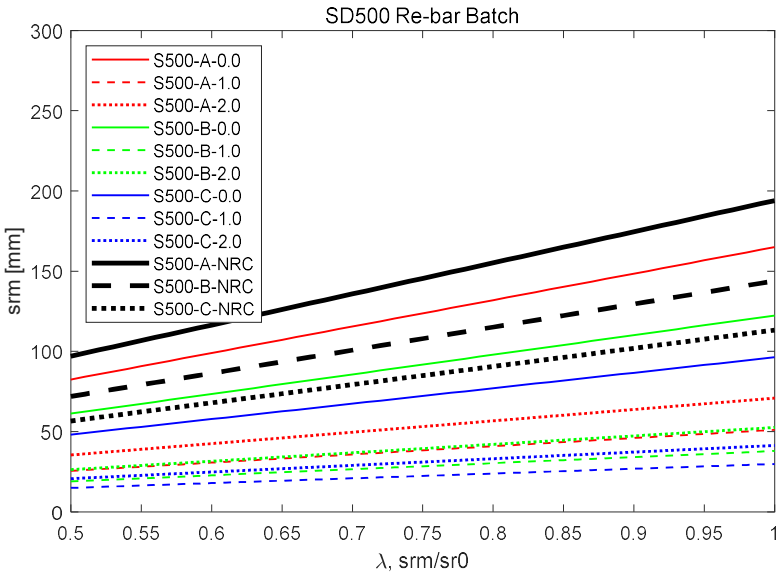

(c)

Figure 3-21 Modeled crack spacing of UHPFRC and NRC reinforced with: (a) GFRP re-bar (b) SD400 steel re-bar (c) SD500 steel re-bar

As the maximum crack spacing, s_{r0} is the function of the fiber contribution in tension immediately after the crack, $\sigma_{cf,cr}$, the crack width, w_{cr}, described in **Eq. 2.27** is also dependent to $\sigma_{cf,cr}$. Increasing the steel fiber volume ratio, re-bar diameter, and bond stress, τ_{b0} made it more likely to observe micro cracks. **Figure 3-22** shows a comparison of the overall crack width, w_{cr} of the entire specimens. Also, it can be observed that the crack width of NRC is smaller than that of UHPC, especially in GFRP series. However, by increasing steel fiber volume ratio crack widths of UHPFRC can be controlled.

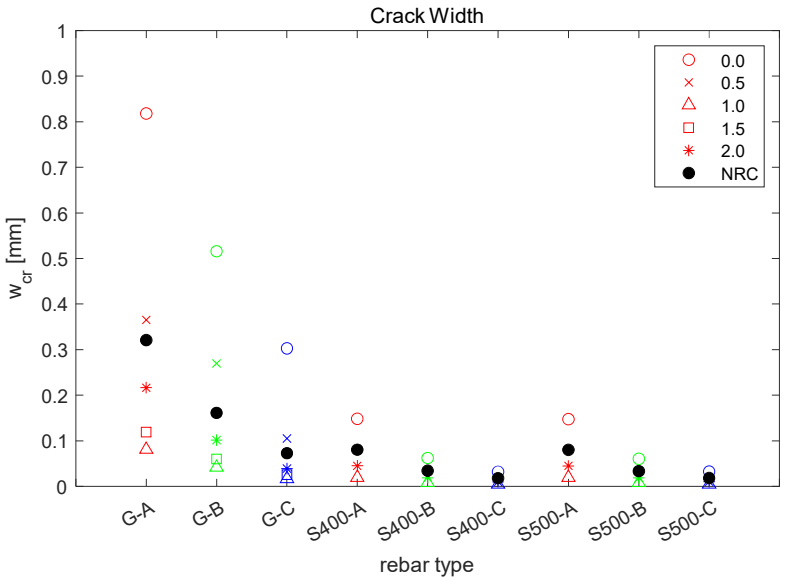

Figure 3-22 Modeled crack width of UHPFRC and NRC

3.4 Conclusion

Different factors can result in various types of re-bar failure, such as pull-out or rupture, which give rise to distinct patterns in the ultimate stress. In GFRP re-bar series, for the specimens failed by pull-out, the ultimate tensile stress rises as the steel fiber volume ratio increases, owing to the bond strength between UHPFRC and the re-bar. Conversely, if the bond strength is sufficient to prevent the pull-out and cause re-bar rupture, the ultimate tensile stress is limited to the re-bar's tensile strength. Additionally, although the ultimate tensile stress increases as the reinforcement ratio increases, the increase of attachment area to the UHPFRC matrix is not proportional, resulting in an increase in slippage due to a relative reduction in bond strength. In the SD400 and SD500 steel re-bar series, an increase in steel fiber volume ratio leads to a rise in the ultimate tensile stress. The localization of cracks around a single major crack results in stress concentration on the corresponding part of the re-bar, causing failure at a smaller strain. This phenomenon is more likely to occur in SD500 series compared to SD400 series at a higher steel fiber volume ratio. In all series except for the steel fiber volume ratio 0.0% series, the ultimate tensile stress exceeded the re-bar's tensile strength due to the contribution of the UHPFRC matrix.

Although the actual crack formation observed during the tests does not precisely match the numerically simulated crack formation suggested by the model, the trends in the variation of crack spacing and crack width among the variables are deemed reliable. The results obtained in this chapter are applied to the Tension Chord Model presented in chapter 5.

Chapter 4. Effects of Shrinkage on Uniaxial Tensile Members

4.1 Introduction

Unlike normal concrete, UHPFRC is susceptible to a substantially high ultimate autogenous shrinkage of about 800 $\mu\varepsilon$ due to its low water-to-binder ratio (W/B). When the high autogenous shrinkage of UHPFRC is limited by internal reinforcing bars, tendons, forms, or adjacent structural members, it can lead to considerable residual tensile stress and shrinkage cracks in the concrete, even in the absence of external loading, posing a risk of diminished effective tensile strength under operating load conditions.

This chapter presents a derivation of theoretical shrinkage strain and corresponding residual stress, which is then applied to the measured member tensile response. A comparison is made between experimental member responses considering the effect of shrinkage and modified member responses that neglect the effect of shrinkage, both modified from the original experimental member responses. The main focus of the comparison is the initial cracking stress with and without shrinkage applied. Finally, the decomposed tensile contribution of the UHPFRC matrix in member responses that neglect the effect of shrinkage is compared with results from the N-series.

4.2 Residual Tensile Stress Due to Shrinkage

The Fehling et al. [9] model, described in section 2.2.2, proposes the theoretical ε_{sh} - ρ_{tot} relationship. ε_{sh} was derived from **Eq. (2.14)** and applied to the Bischoff et al. [8] model, which suggests **Eq. (2.12)**, to obtain the corresponding residual load, P_{sh} and initial UHPFRC strain for zero axial load, ε_{ci} for each variable by considering theoretical shrinkage. **Figure 2-3** depict the **(a)** detailed effect of shrinkage on member response and **(b)** test response and shrinkage compensated response, respectively. The residual load, P_{sh} is dependent on the corresponding shrinkage, ε_{sh} and the molulus of elasticity of re-bar, E_s. **Figure 4-1** displays the total shrinkage strain, ε_{sh}, and the corresponding residual load, P_{sh}, of each test specimen. Due to the lower modulus of elasticity of GFRP re-bar, larger shrinkage strains and smaller residual stresses were observed compared to those of steel re-bar.

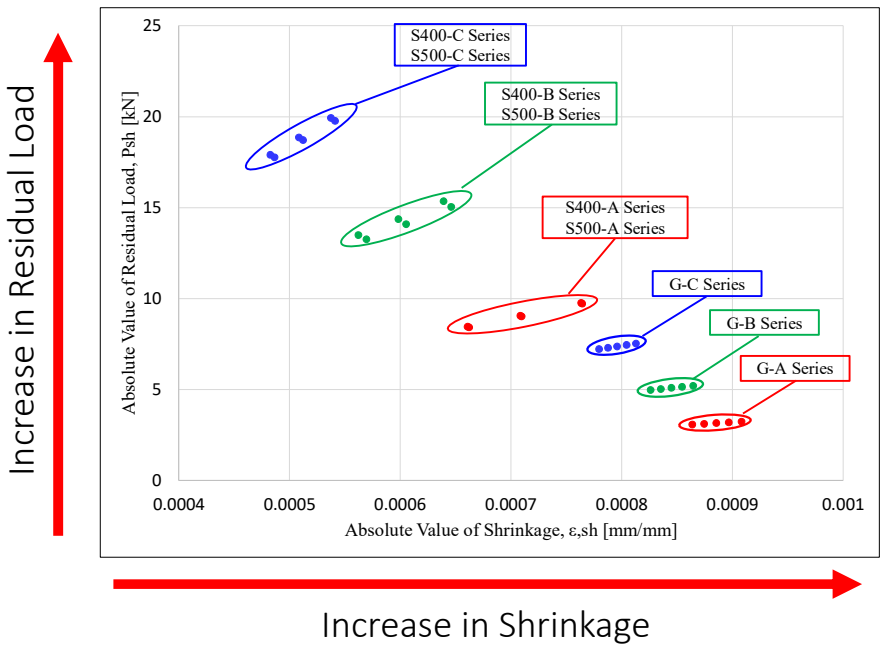

Figure 4-1 Residual load, p_{sh} due to member shortening and corresponding shrinkage strain, ε_{sh}

4.3 Initial Cracking Load

The location of the first significant bend in the experimental member tensile response indicates the occurrence of the initial crack. In this section, the experimental member tensile response (considering shrinkage effect) and the modified member tensile response (neglecting shrinkage effect) is derived by adjusting the member tensile response directly from the test. The difference in initial cracking load before and after adjustment is compared.

4.3.1 Experimental Behavior Considering the Effect of Shrinkage

Table 4-1 shows the N series specimens shrinkage strain, ε_{sh}, corresponding residual load, P_{sh} and initial UHPFRC strain for zero axial load, ε_{ci} for the reference. It shows the pure effect of steel fiber volume ratio to shrinkage which is only half of the effect of the re-bar. N-0.0 has total shrinkage strain of -0.00098, which is the maximum shrinkage.

Table 4-1 N series shrinkage strain, ε_{sh}, corresponding residual load, P_{sh} and initial UHPFRC strain for zero axial load, ε_{ci}

Notation	V_f [%]	ε_{sh} [mm/mm]	ε_{ci} [mm/mm]	P_{sh} [kN]
N-0.0	0.0	-0.00098	-0.00098	0.00
N-0.5	0.5	-0.00093	-0.000918	0.00
N-1.0	1.0	-0.00088	-0.000863	0.00
N-1.5	1.5	-0.00084	-0.000813	0.00
N-2.0	2.0	-0.00080	-0.000768	0.00

The GFRP re-bar series have results of shrinkage strain, ε_{sh} and residual load, P_{sh} varying from -0.000908 to -0.000741 and $-7.53kN$ to $-3.08kN$ respectively. Although the effect is small, the steel fiber volume ratio increase has a relieving effect on the shrinkage strain and residual load. **Tables 4-2, 4-3** and **4-4** show the result values, while Figure 4-2 shows the GFRP re-bar series tensile response considering shrinkage effect.

Table 4-2 G-A series shrinkage strain, ε_{sh}, corresponding residual load, P_{sh} and initial UHPFRC strain for zero axial load, ε_{ci}

Notation	V_f [%]	ε_{sh} [mm/mm]	ε_{ci} [mm/mm]	P_{sh} [kN]
G-A-0.0	0.0	-0.000908	-0.000894	-3.24
G-A-0.5	0.5	-0.000897	-0.00088	-3.20
G-A-1.0	1.0	-0.000885	-0.000867	-3.16
G-A-1.5	1.5	-0.000874	-0.000854	-3.12
G-A-2.0	2.0	-0.000864	-0.000841	-3.08

Table 4-3 G-B series shrinkage strain, ε_{sh}, corresponding residual load, P_{sh} and initial UHPFRC strain for zero axial load, ε_{ci}

Notation	V_f [%]	ε_{sh} [mm/mm]	ε_{ci} [mm/mm]	P_{sh} [kN]
G-B-0.0	0.0	-0.000877	-0.000857	-4.62
G-B-0.5	0.5	-0.000869	-0.000847	-4.57
G-B-1.0	1.0	-0.00086	-0.000836	-4.52
G-B-1.5	1.5	-0.000851	-0.000826	-4.48
G-B-2.0	2.0	-0.000843	-0.000816	-4.43

Table 4-4 G-C series shrinkage strain, ε_{sh}, corresponding residual load, P_{sh} and initial UHPFRC strain for zero axial load, ε_{ci}

Notation	V_f [%]	ε_{sh} [mm/mm]	ε_{ci} [mm/mm]	P_{sh} [kN]
G-C-0.0	0.0	-0.000813	-0.000781	-7.53
G-C-0.5	0.5	-0.000804	-0.000771	-7.45
G-C-1.0	1.0	-0.000796	-0.000761	-7.37
G-C-1.5	1.5	-0.000788	-0.000751	-7.29
G-C-2.0	2.0	-0.000779	-0.000741	-7.22

The initial cracking load does not show a clear tendency and there is not a significant difference between each variable. This is likely due to the fact that the difference in residual load resulting from changes in the diameter of the re-bar is relatively small. Additionally, the initial UHPFRC strain for zero axial load, ε_{ci}, for each variable, does not vary significantly from one another.

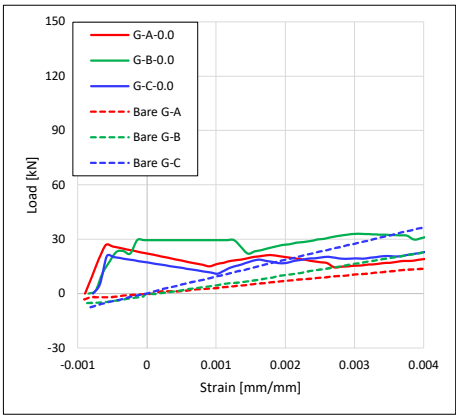
G-A-0.0
G-B-0.0
G-C-0.0
Bare G-A
Bare G-B
Bare G-C
Load [kN]
Strain [mm/mm]

(a)

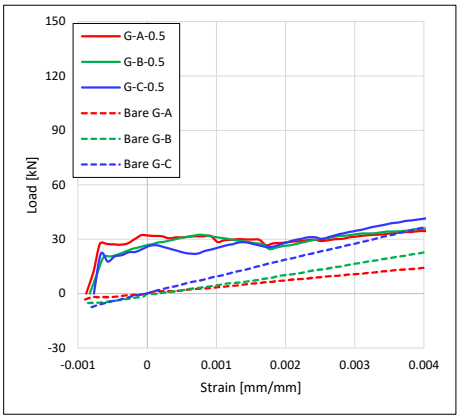
G-A-0.5
G-B-0.5
G-C-0.5
Bare G-A
Bare G-B
Bare G-C
Load [kN]
Strain [mm/mm]

(b)

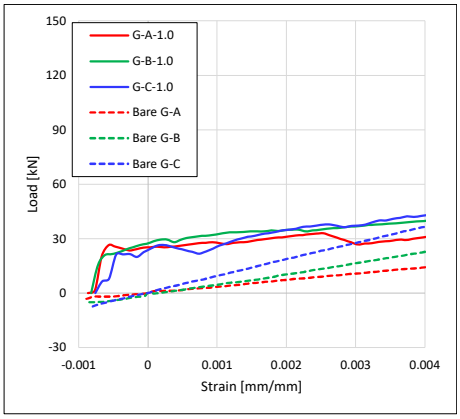
G-A-1.0
G-B-1.0
G-C-1.0
Bare G-A
Bare G-B
Bare G-C
Load [kN]
Strain [mm/mm]

(c)

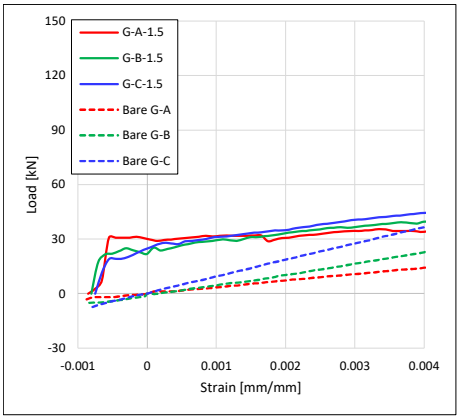
G-A-1.5
G-B-1.5
G-C-1.5
Bare G-A
Bare G-B
Bare G-C
Load [kN]
Strain [mm/mm]

(d)

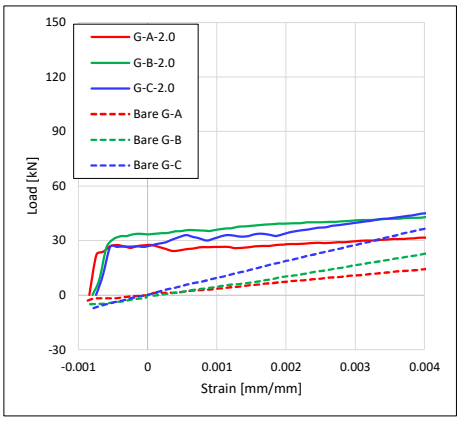
G-A-2.0
G-B-2.0
G-C-2.0
Bare G-A
Bare G-B
Bare G-C
Load [kN]
Strain [mm/mm]

(e)

Figure 4-2 Tensile behavior of specimens with GFRP re-bars with experimental origin, $\varepsilon_{\exp}$, considering shrinkage, steel fiber volume ratio: (a) 0.0% (b) 0.5% (c) 1.0% (d) 1.5% (e) 2.0%

The SD400 steel re-bar series have results of shrinkage strain, ε_{sh} and residual load, P_{sh} varying from -0.000764 to -0.000482 and $-19.94kN$ to $-8.42kN$ respectively. The increase of steel fiber volume ratio has a larger relieving effect on the shrinkage strain and residual load compared to GFRP series. **Tables 4-5, 4-6** and **4-7** show the result values, while **Figure 4-3** shows the SD400 steel re-bar series tensile response considering shrinkage effect.

Table 4-5 S400-A series shrinkage strain, ε_{sh}, corresponding residual load, P_{sh} and initial UHPFRC strain for zero axial load, ε_{ci}

Notation	V_f [%]	ε_{sh} [mm/mm]	ε_{ci} [mm/mm]	P_{sh} [kN]
S400-A-0.0	0.0	-0.000764	-0.000723	-9.72
S400-A-1.0	1.0	-0.000709	-0.000659	-9.02
S400-A-2.0	2.0	-0.000662	-0.000604	-8.42

Table 4-6 S400-B series shrinkage strain, ε_{sh}, corresponding residual load, P_{sh} and initial UHPFRC strain for zero axial load, ε_{ci}

Notation	V_f [%]	ε_{sh} [mm/mm]	ε_{ci} [mm/mm]	P_{sh} [kN]
S400-B-0.0	0.0	-0.000646	-0.000585	-15.05
S400-B-1.0	1.0	-0.000605	-0.000538	-14.10
S400-B-2.0	2.0	-0.000569	-0.000497	-13.26

Table 4-7 S400-C series shrinkage strain, ε_{sh}, corresponding residual load, P_{sh} and initial UHPFRC strain for zero axial load, ε_{ci}

Notation	V_f [%]	ε_{sh} [mm/mm]	ε_{ci} [mm/mm]	P_{sh} [kN]
S400-C-0.0	0.0	-0.000537	-0.000461	-19.94
S400-C-1.0	1.0	-0.000508	-0.000429	-18.87
S400-C-2.0	2.0	-0.000482	-0.0004	-17.90

The initial cracking load displays a more noticeable trend and significant differences between each variable compared to the GFRP series. The initial cracking load decreases as the diameter of the re-bar increases. This is likely because the difference in residual load resulting from changes in the re-bar diameter is relatively larger compared to the GFRP series. Furthermore, the initial UHPFRC strain for zero axial load, ε_{ci}, for each variable exhibits a significant difference as the re-bar diameter varies.

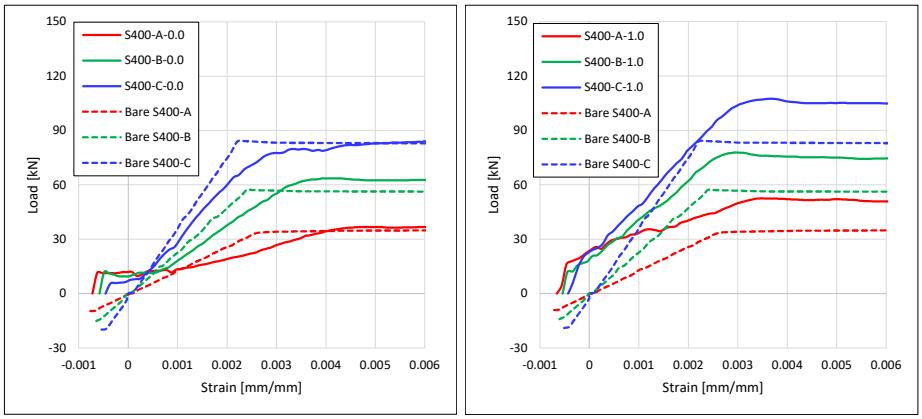

(a)

(b)

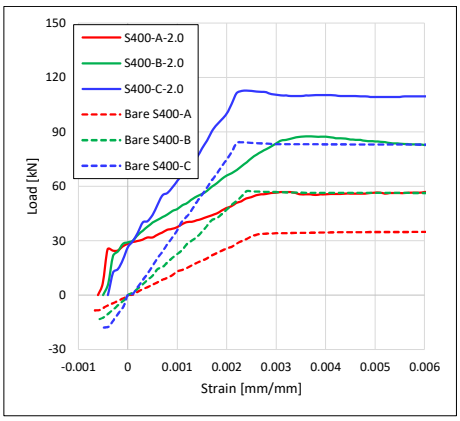

(c)

Figure 4-3 Tensile behavior of specimens with SD400 steel re-bars with experimental origin, $\varepsilon_{\exp}$, considering shrinkage, steel fiber volume ratio: (a) 0.0% (b) 1.0% (c) 2.0%

The SD500 steel re-bar series have results of shrinkage strain, ε_{sh} and residual load, P_{sh} varying from -0.000763 to -0.000486 and $-19.77kN$ to $-8.45kN$ respectively. **Tables 4-8, 4-9** and **4-10** show the

result values, while **Figure 4-4** shows the SD500 steel re-bar series tensile response considering shrinkage effect. The results are nearly identical to those of the SD400 steel re-bar series, as there is not a significant difference in the modulus of elasticity between SD400 and SD500 re-bars.

Table 4-8 S500-A series shrinkage strain, ε_{sh}, corresponding residual load, P_{sh} and initial UHPFRC strain for zero axial load, ε_{ci}

Notation	V_f [%]	ε_{sh} [mm/mm]	ε_{ci} [mm/mm]	P_{sh} [kN]
S500-A-0.0	0.0	-0.000763	-0.000722	-9.76
S500-A-1.0	1.0	-0.000708	-0.000658	-9.06
S500-A-2.0	2.0	-0.000661	-0.000603	-8.45

Table 4-9 S500-B series shrinkage strain, ε_{sh}, corresponding residual load, P_{sh} and initial UHPFRC strain for zero axial load, ε_{ci}

Notation	V_f [%]	ε_{sh} [mm/mm]	ε_{ci} [mm/mm]	P_{sh} [kN]
S500-B-0.0	0.0	-0.000639	-0.000577	-15.35
S500-B-1.0	1.0	-0.000598	-0.00053	-14.37
S500-B-2.0	2.0	-0.000562	-0.000489	-13.50

Table 4-10 S500-C series shrinkage strain, ε_{sh}, corresponding residual load, P_{sh} and initial UHPFRC strain for zero axial load, ε_{ci}

Notation	V_f [%]	ε_{sh} [mm/mm]	ε_{ci} [mm/mm]	P_{sh} [kN]
S500-C-0.0	0.0	-0.000541	-0.000465	-19.77
S500-C-1.0	1.0	-0.000512	-0.000433	-18.72
S500-C-2.0	2.0	-0.000486	-0.000404	-17.77

Similar to the SD400 series, the initial cracking load exhibits a clear trend and significant variation among each variable in comparison to the GFRP series.

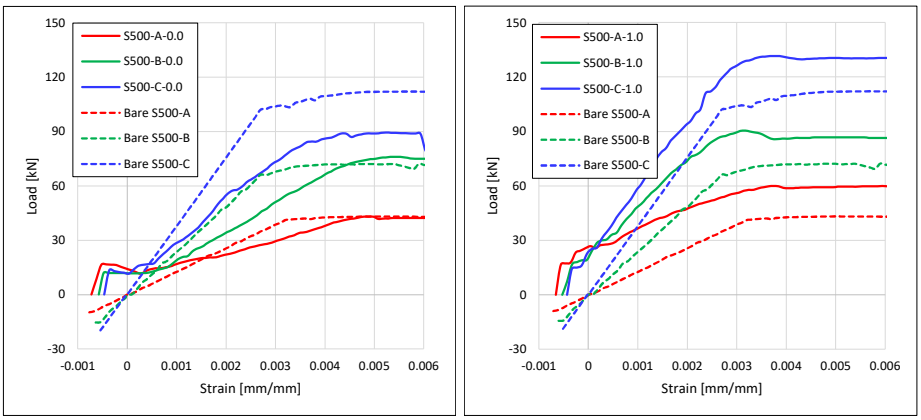

(a)

(b)

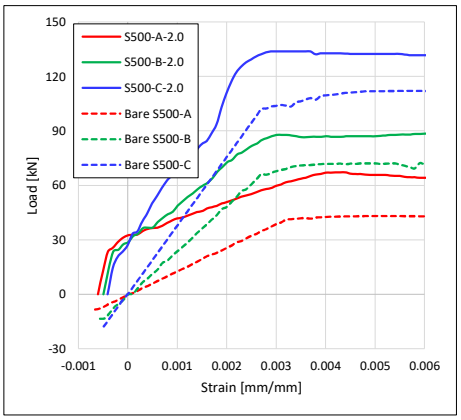

(c)

Figure 4-4 Tensile behavior of specimens with SD500 steel re-bars with experimental origin, $\varepsilon_{\exp}$, considering shrinkage, steel fiber volume ratio: (a) 0.0% (b) 1.0% (c) 2.0%

4.3.2 Modified Behavior for Neglecting the Effect of Shrinkage

Modified behavior neglecting the effect of shrinkage was obtained by moving each part at the coordinates according to the ratio of strain, to make the shrinkage strain 0 in the slope of the modulus of elasticity of the bare re-bar. Section 2.2.1 provide detailed explanations. As depicted in **Figure 4-5, 4-6** and **4-7**, in members with the same steel fiber volume ratio, the points indicating initial cracking in the modified tensile response of members with different re-bar diameters are distributed closer together.

The initial cracking load in the modified tensile behavior neglecting the effect of shrinkage in GFRP re-bar series increase compared to those in the tensile behavior considering shrinkage effect. The corresponding values derived for the increase in initial cracking stress, $\overline{\sigma}_{i,cr}$ are presented in **Table 4-11** and **Eq. (4.1)**, where, $P_{\mathrm{mod},cr}$ is the cracking load in the modified tensile behavior neglecting the effect of shrinkage, $P_{\mathrm{exp},cr}$ is the cracking load in the experimental behavior considering the effect of shrinkage and A is the member gross sectional area $\left(A_c + A_s\right)$.

$$\overline{\sigma}_{i,cr} = \frac{P_{\mathrm{mod},cr} - P_{\mathrm{exp},cr}}{A} \tag{4.1}$$

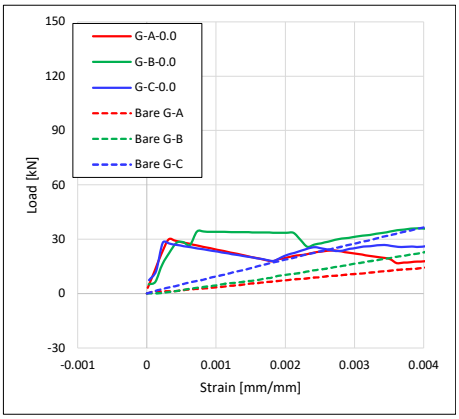
G-A-0.0
G-B-0.0
G-C-0.0
Bare G-A
Bare G-B
Bare G-C
Load [kN]
Strain [mm/mm]

(a)

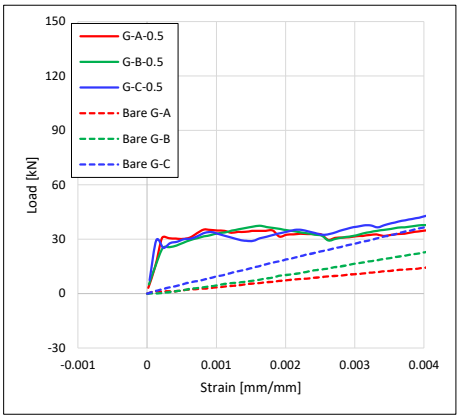
G-A-0.5
G-B-0.5
G-C-0.5
Bare G-A
Bare G-B
Bare G-C
Load [kN]
Strain [mm/mm]

(b)

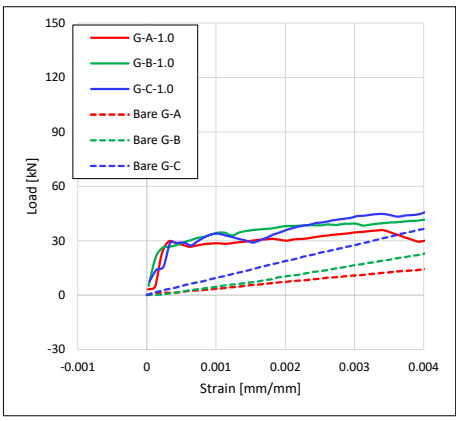
G-A-1.0
G-B-1.0
G-C-1.0
Bare G-A
Bare G-B
Bare G-C
Load [kN]
Strain [mm/mm]

(c)

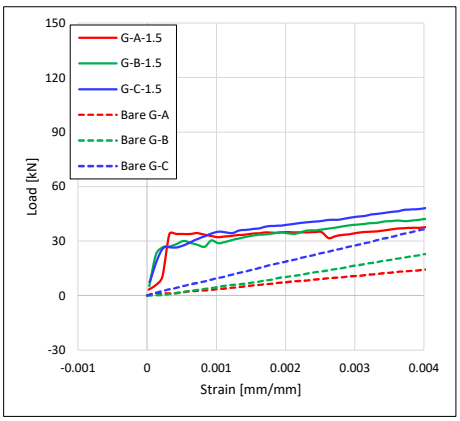
G-A-1.5
G-B-1.5
G-C-1.5
Bare G-A
Bare G-B
Bare G-C
Load [kN]
Strain [mm/mm]

(d)

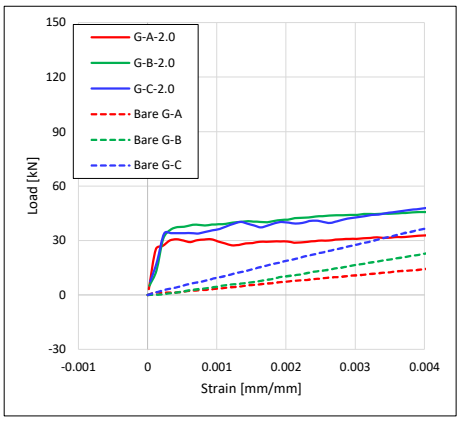
G-A-2.0
G-B-2.0
G-C-2.0
Bare G-A
Bare G-B
Bare G-C
Load [kN]
Strain [mm/mm]

(e)

Figure 4-5 Modified tensile behavior of specimens with GFRP re-bars considering no shrinkage, steel fiber volume ratio: (a) 0.0% (b) 0.5% (c) 1.0% (d) 1.5% (e) 2.0%

Table 4-11 The increase of the initial cracking stress when neglecting shrinkage effect, $\overline{\sigma}_{i,cr}$ in GFRP re-bar series [MPa]

V_f [%]	0.0	0.5	1.0	1.5	2.0
G-A	0.64	0.63	0.65	0.65	0.62
G-B	0.85	0.88	0.85	0.89	0.90
G-C	1.47	1.47	1.48	1.46	1.47

The increase of the initial cracking stress when neglecting shrinkage effect, $\overline{\sigma}_{i,cr}$ in SD400 steel re-bar series increase compared to those in the tensile behavior of GFRP re-bar series as presented in **Table 4-12**. Due to the large modulus of elasticity of steel re-bar, the residual load caused by shrinkage differs significantly for each re-bar diameter, resulting in a significant difference in the corresponding $\overline{\sigma}_{i,cr}$.

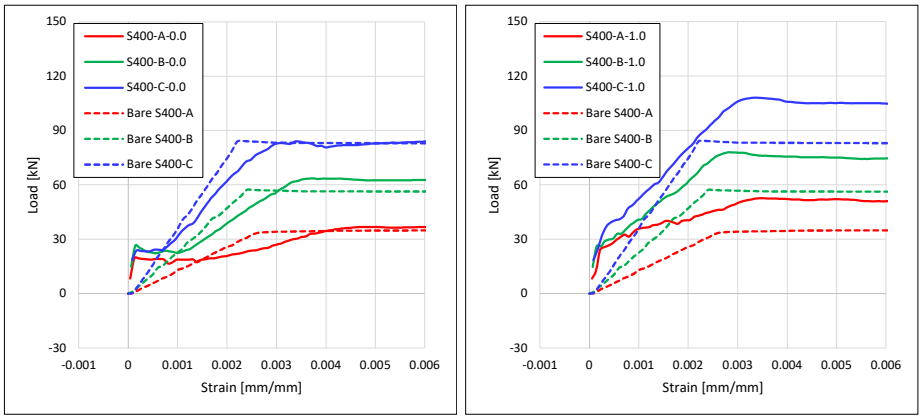

(a) (b)

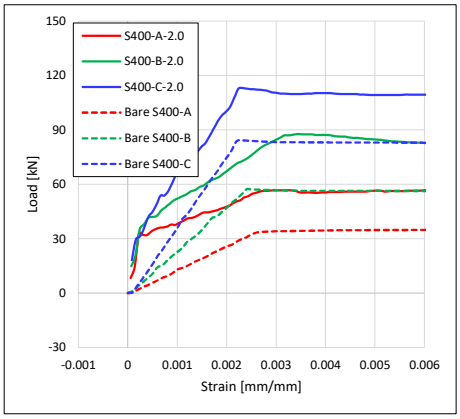

(c)

Figure 4-6 Modified tensile behavior of specimens with SD400 steel re-bars considering no shrinkage, steel fiber volume ratio: (a) 0.0% (b) 1.0% (c) 2.0%

Table 4-12 The increase of the initial cracking stress when neglecting shrinkage effect, $\overline{\sigma}_{i,cr}$ in SD400 steel re-bar series, [MPa]

V_f [%]	0.0	1.0	2.0
S400-A	1.54	1.24	1.45
S400-B	2.69	2.63	2.39
S400-C	3.21	3.00	2.78

Table 4-13 demonstrates that the increase in initial cracking stress when neglecting the shrinkage effect, $\overline{\sigma}_{i,cr}$ is similar in SD500 steel re-bar series compared to SD400 steel re-bar series, as both have a similar modulus of elasticity.

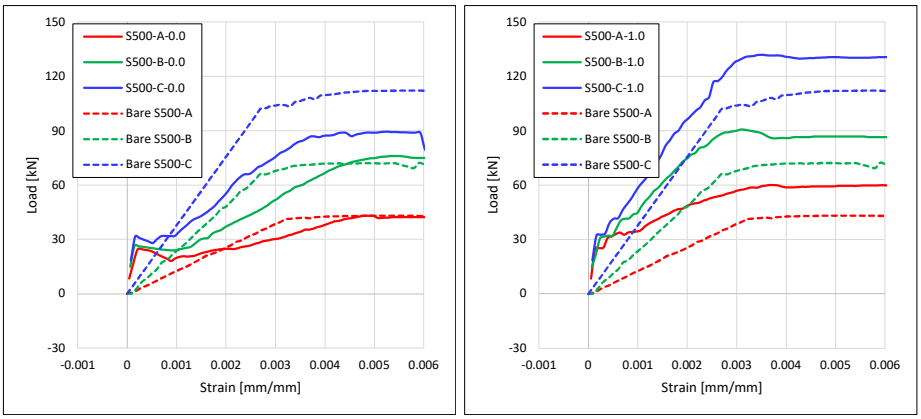

(a)

(b)

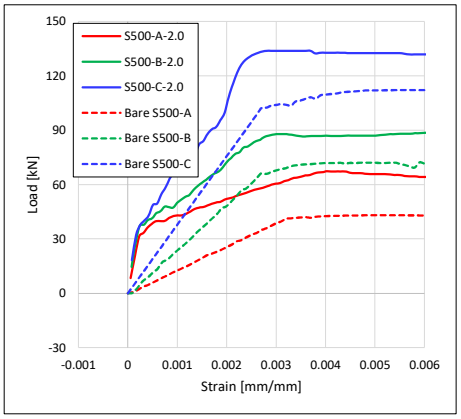

(c)

Figure 4-7 Modified tensile behavior of specimens with SD500 steel re-bars considering no shrinkage, steel fiber volume ratio: (a) 0.0% (b) 1.0% (c) 2.0%

Table 4-13 The increase of the initial cracking stress when neglecting shrinkage effect, $\overline{\sigma}_{i,cr}$ in SD500 steel re-bar series, [MPa]

V_f [%]	0.0	1.0	2.0
S500-A	1.51	1.41	1.35
S500-B	2.61	2.47	2.43
S500-C	3.20	3.15	2.70

4.4 Conclusion

The comparison between the tensile behaviors of the members with and without considering the shrinkage effect is carried out with a focus on the initial cracking load as the main concern in this chapter. The maximum shrinkage strain and corresponding residual load of members with each variable, the primary factors that influence the initial cracking load were derived. These factors were then used to modify the original tensile behavior of the members to obtain experimental tensile behavior with the effect of shrinkage considered, and modified tensile behavior with the effect of shrinkage neglected.

It was found that there is an increase in residual load with the increase in both the diameter and modulus of elasticity of the re-bar. On the other hand, an increase in the steel fiber volume ratio was found to relieve the residual load, eventually leading to an increase in the initial cracking load. The GFRP re-bar series has the largest shrinkage and the lowest residual load because of small modulus of elasticity compared to series of SD400 and SD500 steel re-bar, resulting the largest initial cracking load when the shrinkage effect is considered.

The tensile contribution of the UHPFRC matrix is determined for the experimental tensile response considering the effect of shrinkage by subtracting the bare re-bar response from it for all variables, and compared with the tensile behavior of the N series. As shown in **Figure 4-8**, the decomposed stress of the UHPFRC matrix exhibits a similar behavior to that of the N series for each steel fiber volume ratio, particularly with respect to the initial cracking stress.

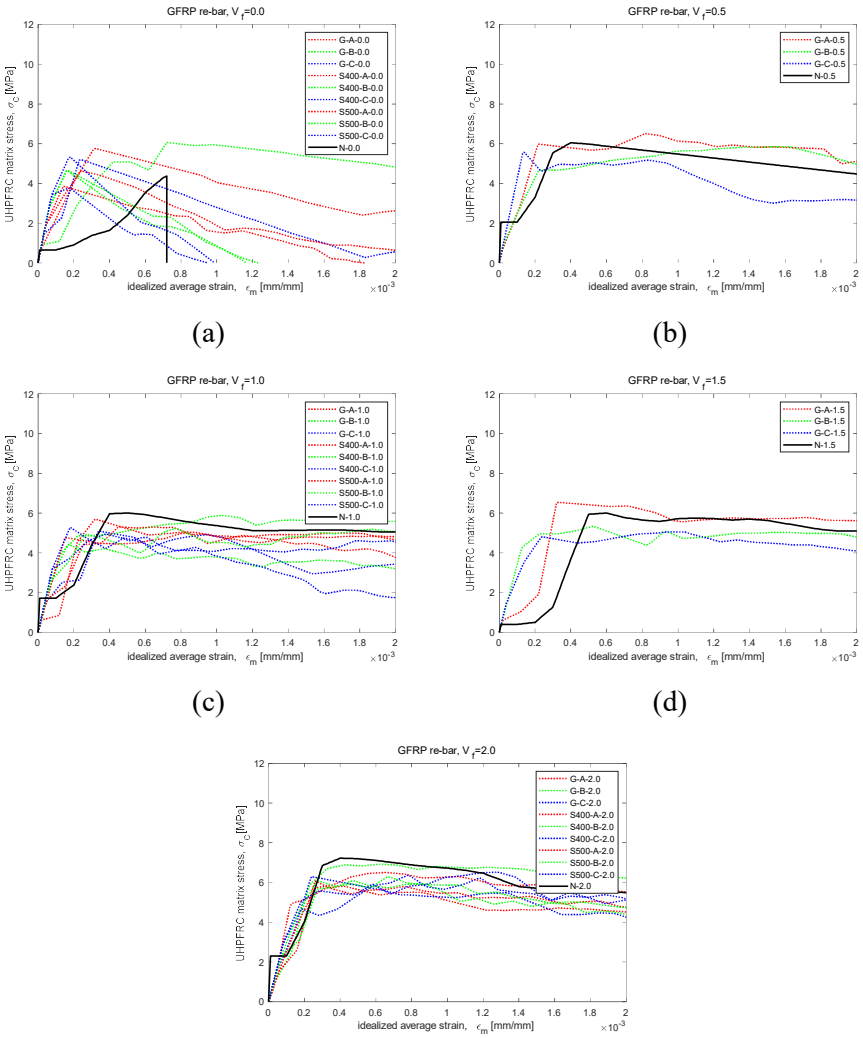

Figure 4-8 UHPFRC matrix decomposed stress compared to N-series, steel fiber volume ratio: (a) 0.0% (b) 0.5% (c) 1.0% (d) 1.5% (e) 2.0%

Chapter 5. Tension Stiffening Effect

5.1 Introduction

The tension stiffening effect refers to the phenomenon where, when tensile loads act on a reinforced concrete structure, the concrete bears some of the tensile stress transmitted from the reinforcement bar due to the bond between the concrete and the reinforcement bar, resulting in a decrease in the deformation of the reinforcement bar. The tension stiffening effect is maintained until the tensile stress exceeds the allowable tensile strength of the concrete and the maximum bond strength between the concrete and reinforcement bar.

The significance lies in situations where the main concern is to forecast the load-bearing capability of members like beams and slabs. Additionally, it is relevant to consider aspects such as the spacing and width of cracks, as well as the stiffness and displacement of both flexural and tensile members.

In this chapter, a comparative analysis is conducted between the tension stiffening effect among various variables obtained through the simple subtraction of bare re-bar response from the measured member response and the Tension Chord Model. This section not only examines the overall tension stiffening effect in a member's response but also provides insight into the detailed behavior of the decomposed UHPFRC matrix tensile contribution in a crack element, taking into account bond strength variations due to the type of re-bar and steel fiber volume ratio.

5.2 Tensile Contribution of UHPFRC Composite by Load Sharing Concept

By comparing the tensile contribution of UHPFRC matrix, which reflects the extent of tension stiffening effect, it is possible to intuitively compare various variables. In this section, the tensile contribution of UHPFRC matrix in elastic state is calculated by directly subtracting the bare re-bar response from the measured member response.

5.2.1 Tension Stiffening Effect by Load Sharing Concept for GFRP Re-bar

The increase in steel fiber volume ratio leads to an increase in tension stiffening effect in GFRP re-bar series. For re-bar with smaller diameters, even a slight increase in steel fiber volume ratio can have a significant impact on tension stiffening effect, but as the diameter of the re-bar increases, the effectiveness of tension stiffening effect decreases as depicted in **Figure 5-1**. It is suggested that this is due to the relative decrease in bond strength compared to the increase in re-bar tensile strength, as explained in section 3.2.2.

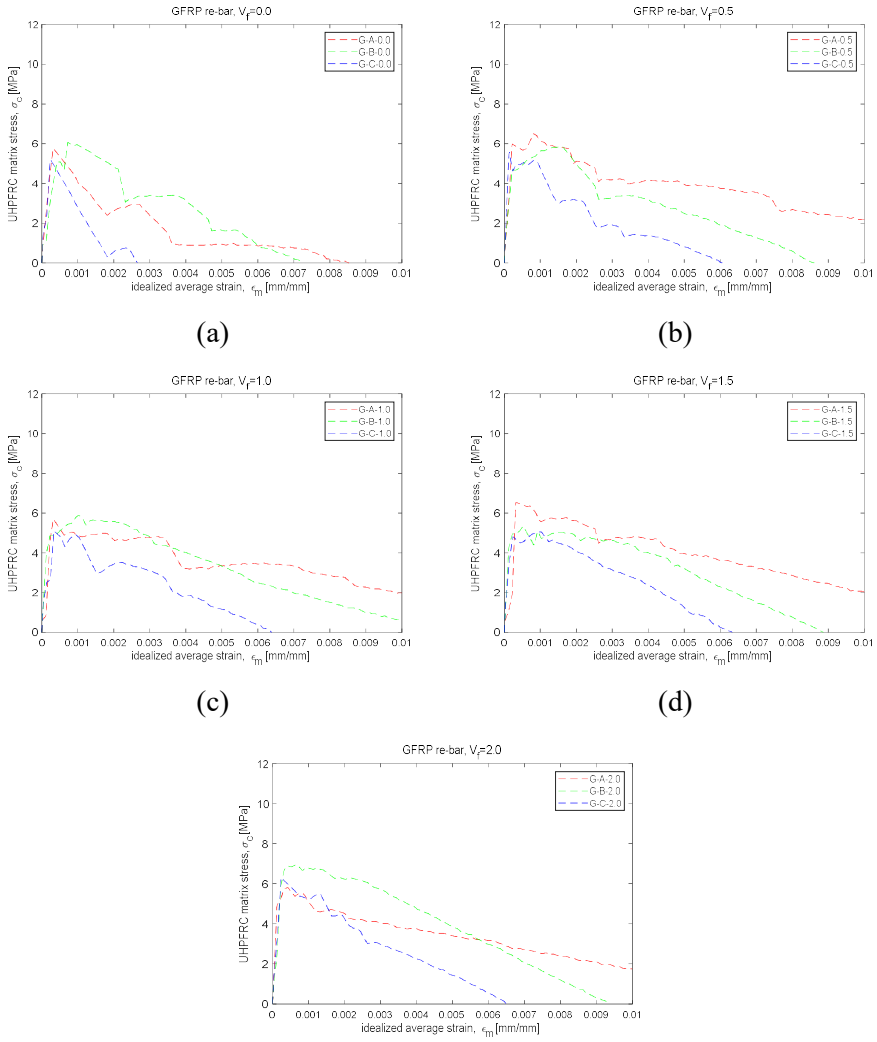

Figure 5-1 Average tensile contribution of UHPFRC matrix in specimen reinforced with GFRP re-bar by Load Sharing Concept, steel fiber volume ratio: (a) 0.0% (b) 0.5% (c) 1.0% (d) 1.5% (e) 2.0%

5.2.2 Tension Stiffening Effect by Load Sharing Concept for Steel Re-bar

The steel re-bar series have a different range of strain in the elastic state compared to the GFRP re-bar series, due to the difference in the modulus of elasticity. **Figure 5-2** and **5-3** shows average tensile contribution of UHPFRC matrix in specimen reinforced with SD400 and SD500 steel re-bar respectively. The increase in tension stiffening effect due to the increase in steel fiber volume ratio shows a similar trend in effectiveness between steel re-bar and GFRP re-bar series. It is considered that when taking into account and removing the values of residual stresses caused by shrinkage from the UHPFRC tensile contribution depicted in **Figures 5-1, 5-2,** and **5-3**, the GFRP re-bar series exhibits a higher peak than the steel re-bar series.

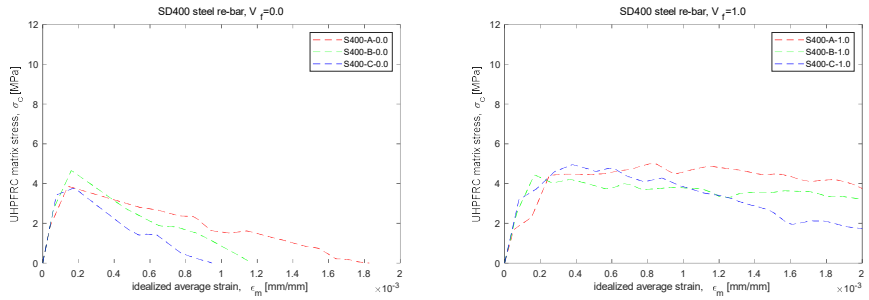

(a)

(b)

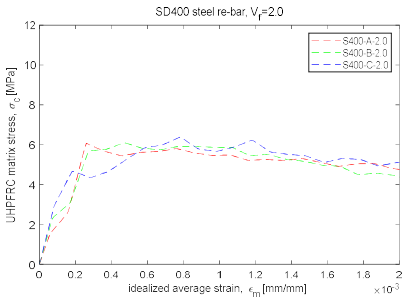

(c)

Figure 5-2 Average tensile contribution of UHPFRC matrix in specimen reinforced with SD400 steel re-bar by Load Sharing Concept, steel fiber volume ratio: (a) 0.0% (b) 1.0% (c) 2.0%

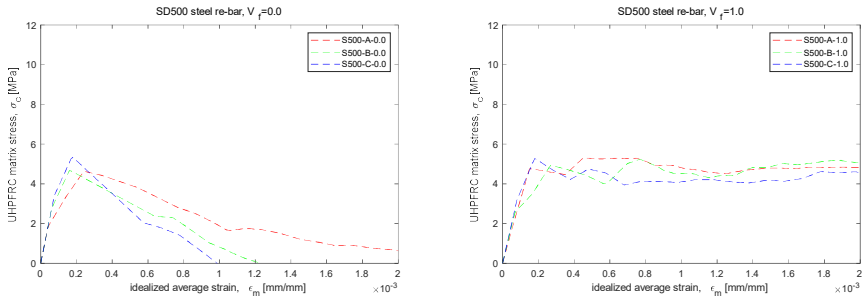

(a)

(b)

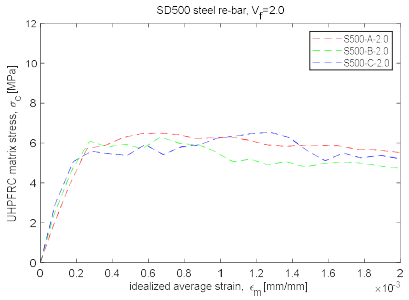

(c)

Figure 5-3 Average tensile contribution of UHPFRC matrix in specimen reinforced with SD500 steel re-bar by Load Sharing Concept, steel fiber volume ratio: (a) 0.0% (b) 1.0% (c) 2.0%

5.3 Tensile Contribution of UHPFRC Composite by Tension Chord Model

The Tension Chord Model is a model that explains the tensile reinforcement effect in short tensile members, effectively describing the contribution of the tensile strength of the concrete according to the state of the reinforcement bar, considering the bond between the reinforcement bar and the concrete in between cracks. In this sectoin, the contribution of the tensile strength of the steel bars and the simple tensile behavior of the steel bars were considered using the Tension Chord Model.

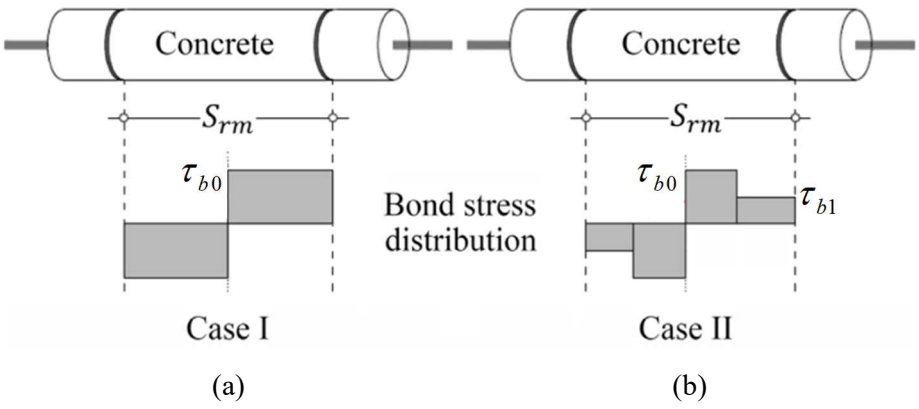

Figure 5-4 Tension Chord Model (TCM) for GFRP and steel re-bar:

(a) Case I (b) Case II (Zhou et al. [20])

Table 5-1 and **5-2** demonstrate the dissimilarities in tensile behavior between GFRP rebar and steel rebar. Specifically, steel rebar has a defined yield strength,

f_y, while GFRP does not. As a result, different approaches were necessary to apply the Tension Chord Model to each material.

Table 5-1 Bare GFRP re-bar tensile test results

Re-bar type	d_s [mm]	E_s [GPa]	f_u [MPa]
D10-GFRP	10	49.978	1000
D13-GFRP	13	41.53	1000
D16-GFRP	16	46.63	750

Table 5-2 Bare steel re-bar tensile test results

Re-bar type	d_s [mm]	E_s [GPa]	E_{sh} [GPa]	f_y [MPa]	f_u [MPa]
D10-SD400	10	178.306	1.302	488.995	585.238
D13-SD400	13	183.875	1.387	451.815	570.126
D16-SD400	16	186.83	1.998	424.144	573.968
D10-SD500	10	179.351	1.056	604.584	709.856
D13-SD500	13	189.602	1.146	570.166	694.475
D16-SD500	16	184.009	0.762	564.527	678.723

5.3.1 Tension Stiffening Effect by Tension Chord Model for GFRP Re-bar

By adopting comparable analytical techniques and considering the mechanical characteristics of a reinforced concrete member with GFRP, the Tension Chord Model is expanded to investigate its overall tensile performance, Zhou et al. [20]. Detailed explanation for modified Tension Chord Model for R-UHPFRC is in section 2.3 and 2.4. Multiple models exist for forecasting the bond-strain curve of GFRP. In this research, the CMR model presented by Cosenza et al. [16] was employed, as Yoo et al. demonstrated that it is the most suitable for utilizing GFRP rebar in UHPFRC.

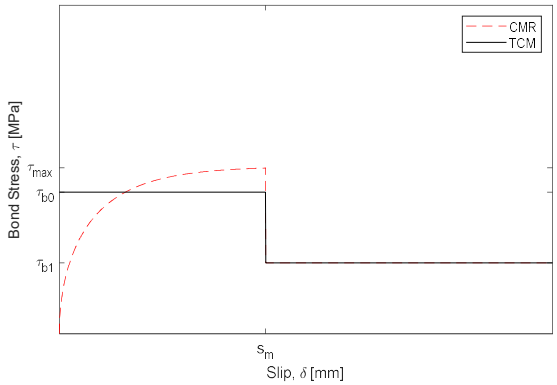

Figure 5-5 Mean bond stress model for GFRP re-bar based on CMR model

The ascending branch, red dotted line (slip, $\delta \le s_m$) in **Figure 5-5** is represented as **Eq. (5.1)**. s_m is slip when the bond stress reaches the maximum bond stress, $\tau_{\max}$. There are few assumptions made for using CMR model. For s_m in this study, it is assumed that the maximum bond stress is

attained when the bond stress reaches 99% of the true maximum bond stress. The curve fitting coefficients, s_r and β are also assumed to be 0.16 and 0.5 respectively, Yoo et al. [15].

$$\frac{\tau}{\tau_{\max}} = \left(1 - e^{-s/s_r}\right)^{\beta} \tag{5.1}$$

The mean bond stress is obtained by integrating the CMR curve up to a specified slip value, s_m . Therefore, the mean bond stress values for the ascending, τ_{b0} and horizontal branches, τ_{b1} of the bond-slip relationship, depicted in **Figure 5-5**, can be determined using **Eq. (5.2)** and **(5.3)**, respectively.

$$\tau_{b0} = \frac{\tau_{\max}}{s_m}\int_0^{s_m}\left(1 - e^{-\delta/s_r}\right)^{\beta} d\delta \tag{5.2}$$

$$\tau_{b1} = \tau_{b0} / 2 \tag{5.3}$$

The mean bond stress, τ , at any point during loading can be computed using **Eq. (5.4)**, where P represents the tensile load, d_b is the diameter of the reinforcement bar, and l_b is the embedment length of the bar.

$$\tau = \frac{P}{\pi d_b l_b} \tag{5.4}$$

Maximum bond stress, $\tau_{\max}$ in **Table 5-3** is derived directly from the test results. In the absence of any additional measures to enhance bond strength, the maximum tensile load obtained from a direct tensile test after the steel fibers

have no effect can be considered as the maximum bond strength. The ultimate tensile load, P_u both when the re-bar is fractured and pulled out is assumed as the maximum bond strength as **Eq. (5.5)**.

$$\tau_{\max} = \frac{P_u}{\pi d_b l_b} \tag{5.5}$$

Table 5-3 GFRP maximum bond stress, $\tau_{\max}$ derived from test results by steel fiber volume ratio [MPa]

Re-bar type	0.0%	0.5%	1.0%	1.5%	2.0%
D10-GFRP	6.43	12.02	11.77	12.02	12.23
D13-GFRP	5.11	8.14	11.46	11.97	13.06
D16-GFRP	3.90	9.39	13.06	12.61	15.29

Due to the symmetry of the chord element, only half of it needs to be analyzed. The amount of slip of δ can be calculated by multiplying the average strain of the GFRP reinforcement, E_f with half the length of the chord element as shown in **Eq. (5.7)**. σ_{fr} is the stress of reinforcement at crack and also the applied stress; E_f is the modulus of elasticity of GFRP reinforcement. The second term on the right-hand side of **Eq. (5.6)**, $\left(\frac{S_{rm}\tau_{b0}}{\phi_f E_f}\right)$ represents the reduced strain resulting from the tension stiffening effect.

$$\varepsilon_{fm} = \frac{\sigma_{fr}}{E_f} - \frac{S_{rm}\tau_{b0}}{\phi_f E_f} \tag{5.6}$$

$$\delta = \varepsilon_{fm} \frac{S_{rm}}{2} \tag{5.7}$$

The length at which the maximum bond stress is achieved on the GFRP re-bar in the crack element, measured from the center, is represented by l_{f1}, and the stress acting on the GFRP at l_{f1} is defined as the critical stress, symbolized as σ_{fr}^{*}. The critical stress σ_{fr}^{*} is obtained from **Eq. (5.6)** and **(5.7)** by assuming δ equals to s_m, as shown in **Eq. (5.8)**.

$$\sigma_{fr}^{*} = \frac{2S_m E_f}{S_{rm}} + \frac{S_{rm}\tau_{b0}}{\phi_f} \tag{5.8}$$

The length l_{f2} is where the stress in the GFRP re-bar surpasses the critical stress. The relationship between l_{f1} and l_{f2} is expressed by **Eq. (5.10)**.

$$l_{f2} = \left(\sigma_{fr} - \sigma_{fr}^{*}\right)\frac{\phi_f}{4\tau_{b1}} \tag{5.9}$$

$$l_{f1} = \frac{s_{r0}}{2} - l_{f2} \tag{5.10}$$

Case I denotes the condition where the stress in the GFRP re-bar has not yet reached the critical stress, which implies that l_{f1} is not positioned within the crack element ($s_{rm}/2 \le l_{f1}$). Assuming that the slip at the crack of the chord, δ, is smaller than s_m, the bond stress distribution along the chord element remains constant, τ_{b0}, resulting in a constant slope of reinforcement stress distribution, $4\tau_{b0}/\phi_f$.

Conversely, Case II pertains to the state where the stress in the GFRP re-bar has exceeded the critical stress, i.e., l_{f1} is situated inside the crack element ($0 \le l_{f1} \le s_{rm}/2$). When the reinforcement stress at the crack σ_{fr} exceeds the critical stress σ_{fr}^{*}, the distribution of reinforcement stress along the chord element is divided into two segments with different slopes, which is caused by the variation of bond stresses. Specifically, a constant bond stress distribution of τ_{b1} exists along the length of l_{f2} near the crack, while the residual portion of a chord element is characterized by the constant bond stress distribution of τ_{b0} along the length of l_{f1}. **Figure 5-6 (a)** and **(b)** illustrate the tensile stress exerted on the GFRP with and without l_{f1} within a crack element, i.e., the region between two adjacent cracks.

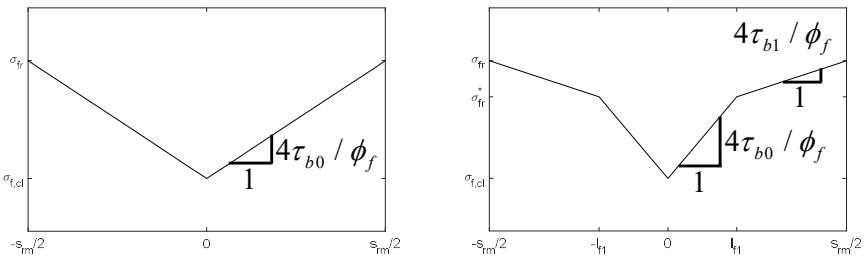

(a) (b)

Figure 5-6 Stress distribution of GFRP re-bar in Tension Chord Model:

(a) Case I ($s_{rm}/2 \le l_{f1}$) (b) Case II ($0 \le l_{f1} \le s_{rm}/2$)

Mean bond stress models for G10 GFRP re-bar by applying CMR model based on the test result maximum bond stress, $\tau_{\max}$ in **Table 5-3** is shown in

Figure 5-7. Also, for G13 and G16 GFRP re-bars, mean bond stress models are shown in **Figure 5-9** and **Figure 5-11** respectively.

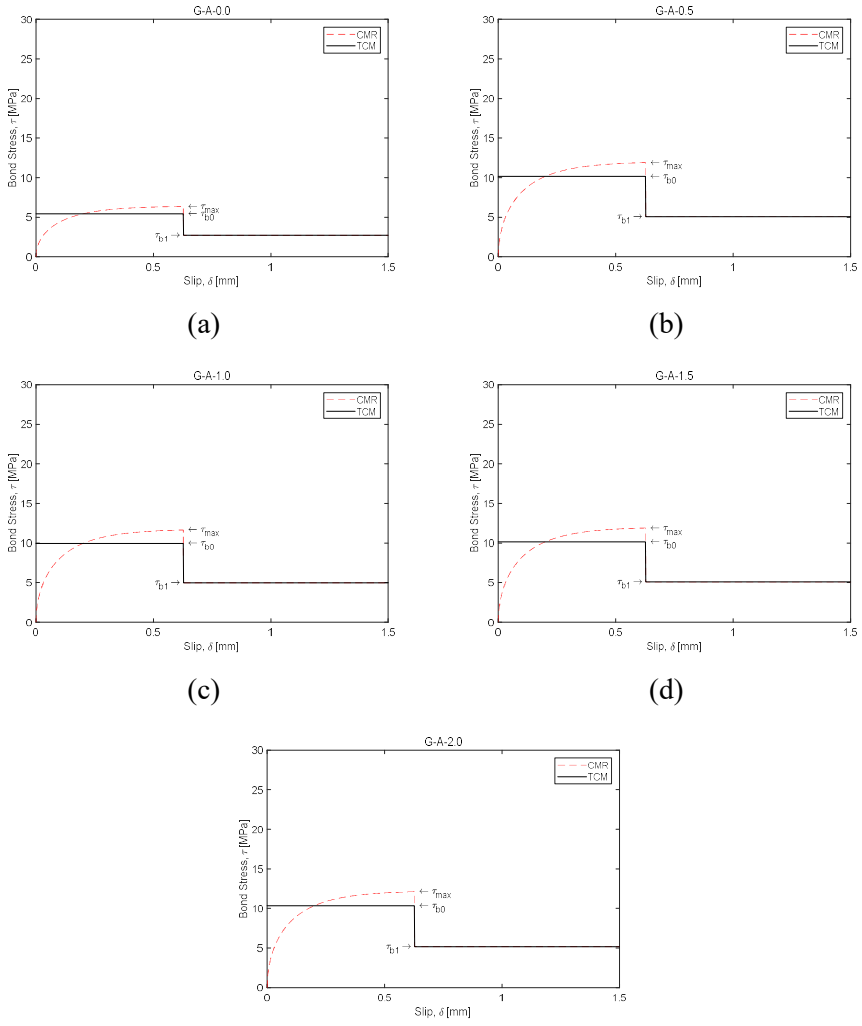

Figure 5-7 Mean bond stress model for G10 GFRP re-bar by applying CMR model, steel fiber volume ratio: (a) 0.0% (b) 0.5% (c) 1.0% (d) 1.5% (e) 2.0%

The 3D plot of maximum tensile contribution of UHPFRC matrix by strain(left) is composed of multiple polygonal sections, each representing the contribution of the concrete matrix to the tensile behavior at a specific average strain of the GFRP rebar. The stiffness of the diagonal line in each section increases as the bond stress increases. The stress in UHPFRC matrix in the center of the crack element, $\sigma_{c,cl}$ is described with a line on the center of polygonal sections. The re-bar stress and corresponding average member strain relationship is expressed in Eq. (2.21), (2.22) and (2.23) for different re-bar state. Also, stresses by both re-bar and UHPFRC matrix according to the location of tension chord element is expressed in Eq. (2.28).

The 3D plot of average tensile contribution of UHPFRC matrix by strain(right) shows the average tensile contribution of UHPFRC matrix along the entire length of the crack element. The rectangular sections depicted in the plot have equivalent area to the polygonal sections in the 3D plot of the maximum tensile contribution of the UHPFRC matrix at the corresponding strain value.

Maximum and average tensile contribution of UHPFRC matrix by strain in specimen reinforced with G10 GFRP re-bar by Tension Chord Model is described in **Figure 5-8**. As the steel fiber volume ratio increases, the length of the crack element decreases, but the contribution of the UHPFRC matrix increases. This can be observed from the fact that the height of the polygonal section increases with increasing steel fiber volume ratio.

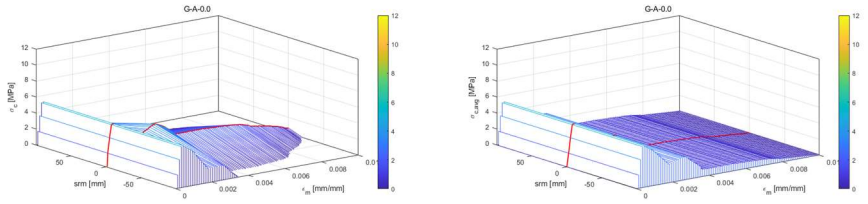
G-A-0.0
G-A-0.0
srm [mm]
srm [mm]

(a)

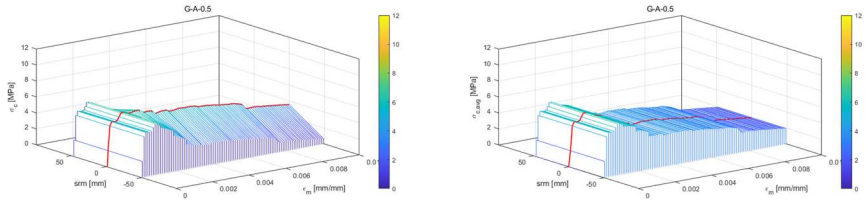
G-A-0.5
G-A-0.5
srm [mm]
srm [mm]

(b)

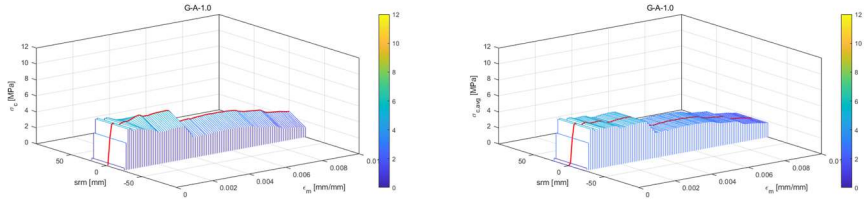
G-A-1.0
G-A-1.0
srm [mm]
srm [mm]

(c)

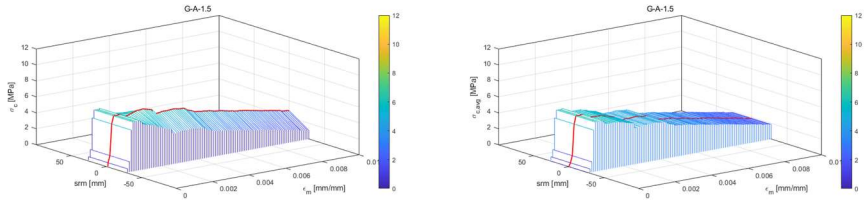
G-A-1.5
G-A-1.5
srm [mm]
srm [mm]

(d)

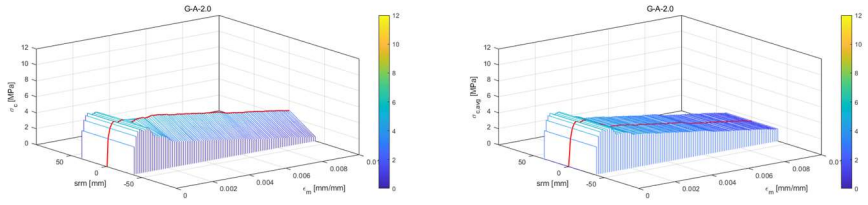
G-A-2.0
G-A-2.0
srm [mm]
srm [mm]

(e)

Figure 5-8 Maximum(left) and average(right) tensile contribution of UHPFRC matrix by strain in entire crack element in specimen reinforced with D10 GFRP re-bar by Tension Chord Model, steel fiber volume ratio: (a) 0.0% (b) 0.5% (c) 1.0% (d) 1.5% (e) 2.0%

Maximum and average tensile contribution of UHPFRC matrix by strain in specimen reinforced with G13 GFRP re-bar by Tension Chord Model is described in **Figure 5-10**. As the steel fiber volume ratio increases, the length of the crack element decreases, but the UHPFRC matrix's tensile contribution increases in a pattern similar to that of the series of G10 GFRP re-bars. However, the overall tensile contribution of the UHPFRC matrix decreases when compared to that of the series of G10 GFRP re-bars.

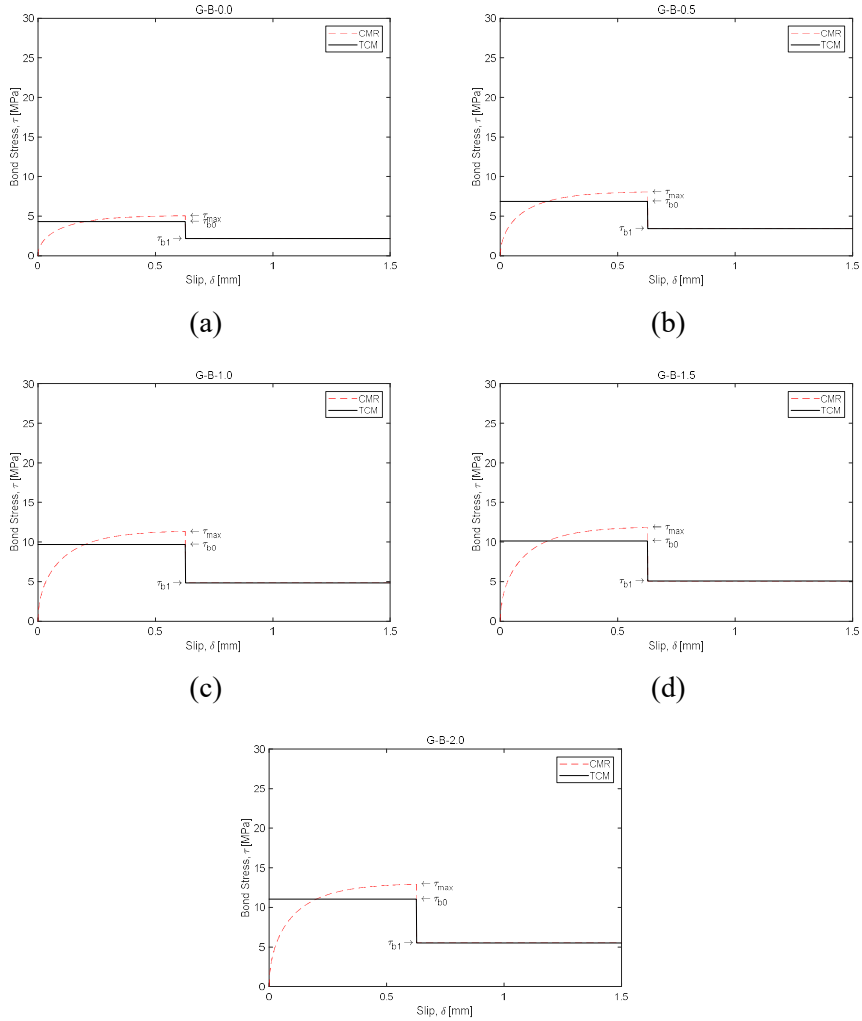

Figure 5-9 Mean bond stress model for G13 GFRP re-bar by applying CMR model, steel fiber volume ratio: (a) 0.0% (b) 0.5% (c) 1.0% (d) 1.5% (e) 2.0%

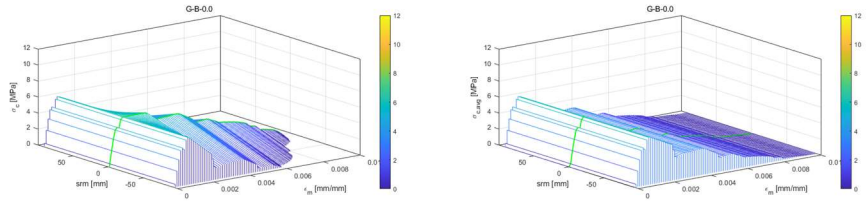
G-B-0.0
G-B-0.0
srm [mm]
srm [mm]

(a)

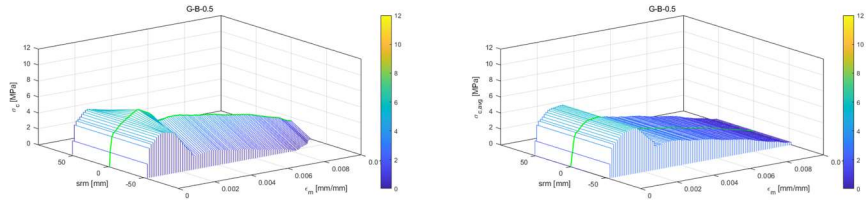
G-B-0.5
G-B-0.5
srm [mm]
srm [mm]

(b)

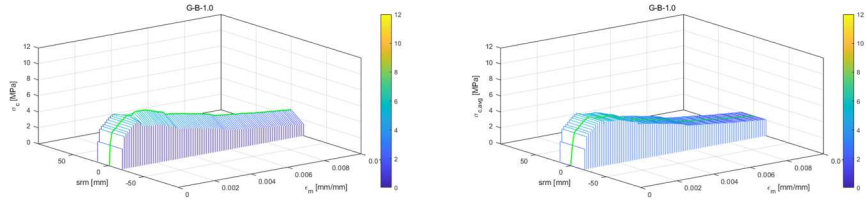
G-B-1.0
G-B-1.0
srm [mm]
srm [mm]

(c)

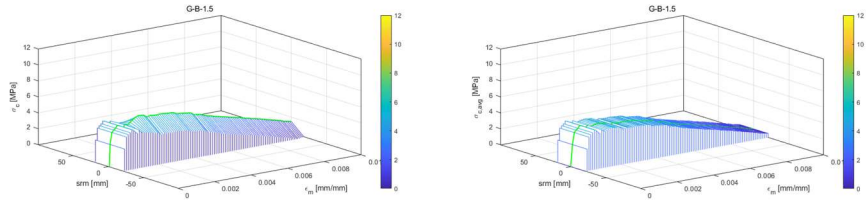
G-B-1.5
G-B-1.5
srm [mm]
srm [mm]

(d)

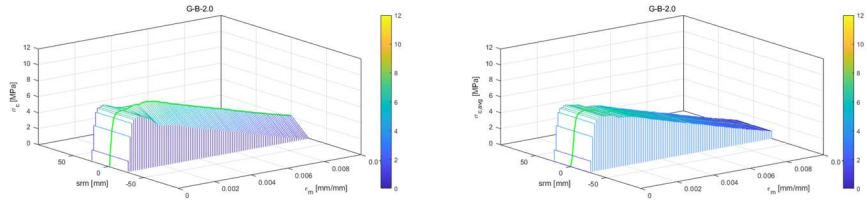
G-B-2.0
G-B-2.0
srm [mm]
srm [mm]

(e)

Figure 5-10 Maximum(left) and average(right) tensile contribution of UHPFRC matrix by strain in entire crack element in specimen reinforced with D13 GFRP re-bar by Tension Chord Model, steel fiber volume ratio: (a) 0.0% (b) 0.5% (c) 1.0% (d) 1.5% (e) 2.0%

Maximum and average tensile contribution of UHPFRC matrix by strain in specimen reinforced with G16 GFRP re-bar by Tension Chord Model is described in **Figure 5-12**. The pattern of increase in tensile contribution of UHPFRC matrix with an increase in steel fiber volume ratio is similar to that observed in the series of G10 and G13 GFRP re-bars. Compared to the series of G10 and G13 GFRP re-bars, the overall tensile contribution of the UHPFRC matrix decreases.

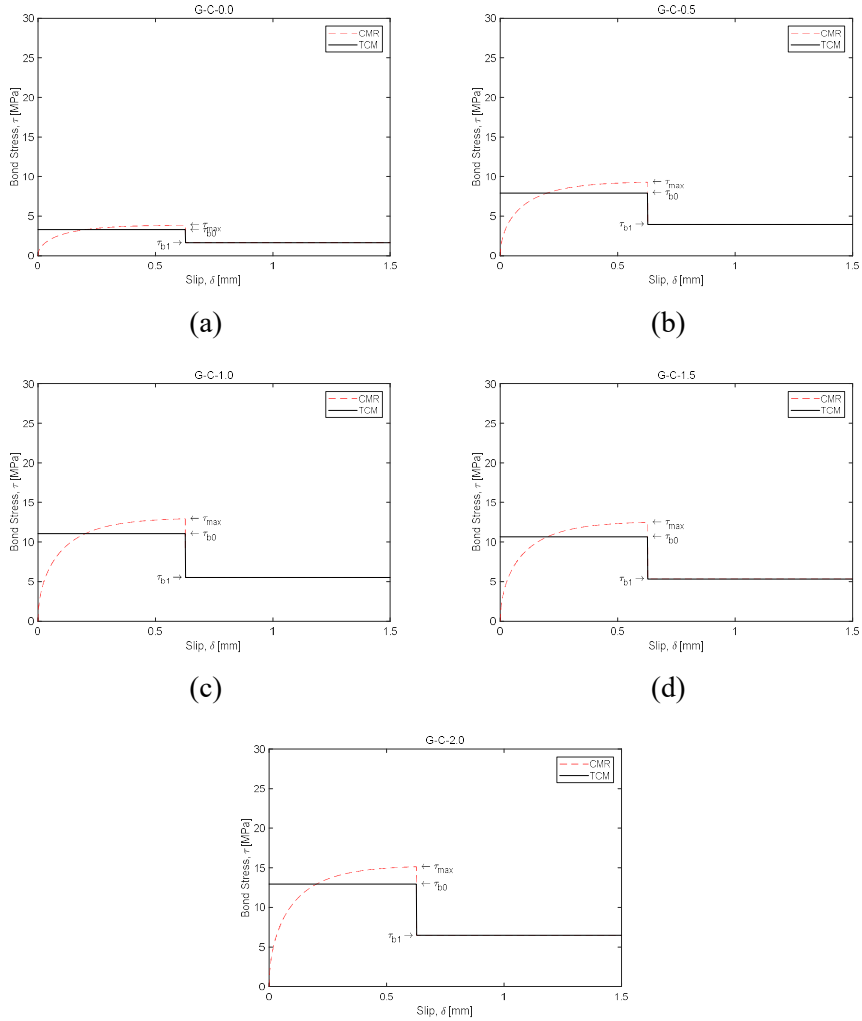

Figure 5-11 Mean bond stress model for G16 GFRP re-bar by applying CMR model, steel fiber volume ratio: (a) 0.0% (b) 0.5% (c) 1.0% (d) 1.5% (e) 2.0%

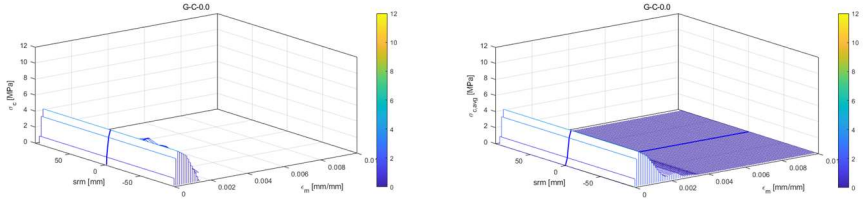
G-C-0.0
G-C-0.0
srm [mm]
srm [mm]

(a)

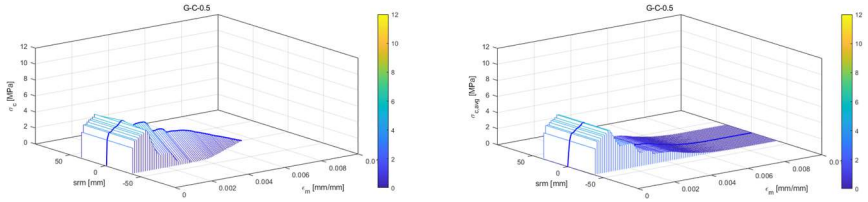
G-C-0.5
G-C-0.5
srm [mm]
srm [mm]

(b)

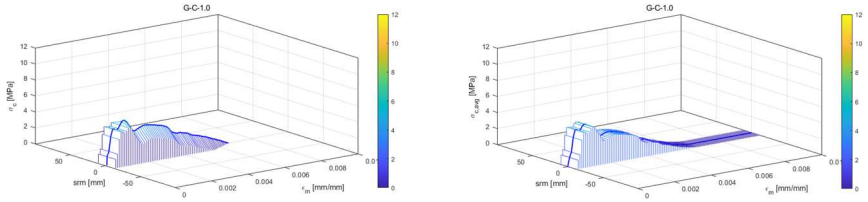
G-C-1.0
G-C-1.0
srm [mm]
srm [mm]

(c)

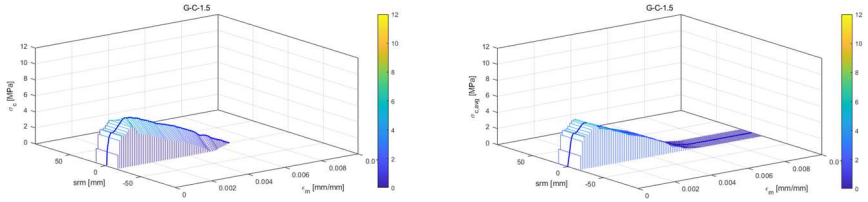
G-C-1.5
G-C-1.5
srm [mm]
srm [mm]

(d)

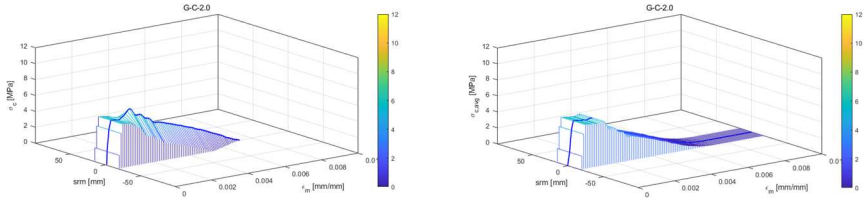
G-C-2.0
G-C-2.0
srm [mm]
srm [mm]

(e)

Figure 5-12 Maximum(left) and average(right) tensile contribution of UHPFRC matrix by strain in entire crack element in specimen reinforced with D16 GFRP re-bar by Tension Chord Model, steel fiber volume ratio: (a) 0.0% (b) 0.5% (c) 1.0% (d) 1.5% (e) 2.0%

The overall comparison of tensile contribution of the UHPFRC matrix of crack element in specimen reinforced with GFRP re-bar is depicted in **Figure 5-13**. The line extracted from the center of the 3D plot of the average tensile contribution of the UHPFRC matrix is converted into 2D curve. The increase in steel fiber volume ratio leads to an increase in the tensile contribution of the UHPFRC matrix, which is associated with the degree of tension stiffening effect. This can be attributed to the increase in bond strength with the increase in steel fiber volume ratio. On the other hand, the tensile contribution of the UHPFRC matrix decreases as the diameter of the re-bar increases. This is considered to be due to the relatively lower increase in bond strength compared to the increase in re-bar strength.

The comparison between the results from the Load Sharing Concept and the Tension Chord Model is shown by drawing the results from the Load Sharing Concept in a dashed line and the results from the Tension Chord Model in a solid line. The two methods show small difference between each other.

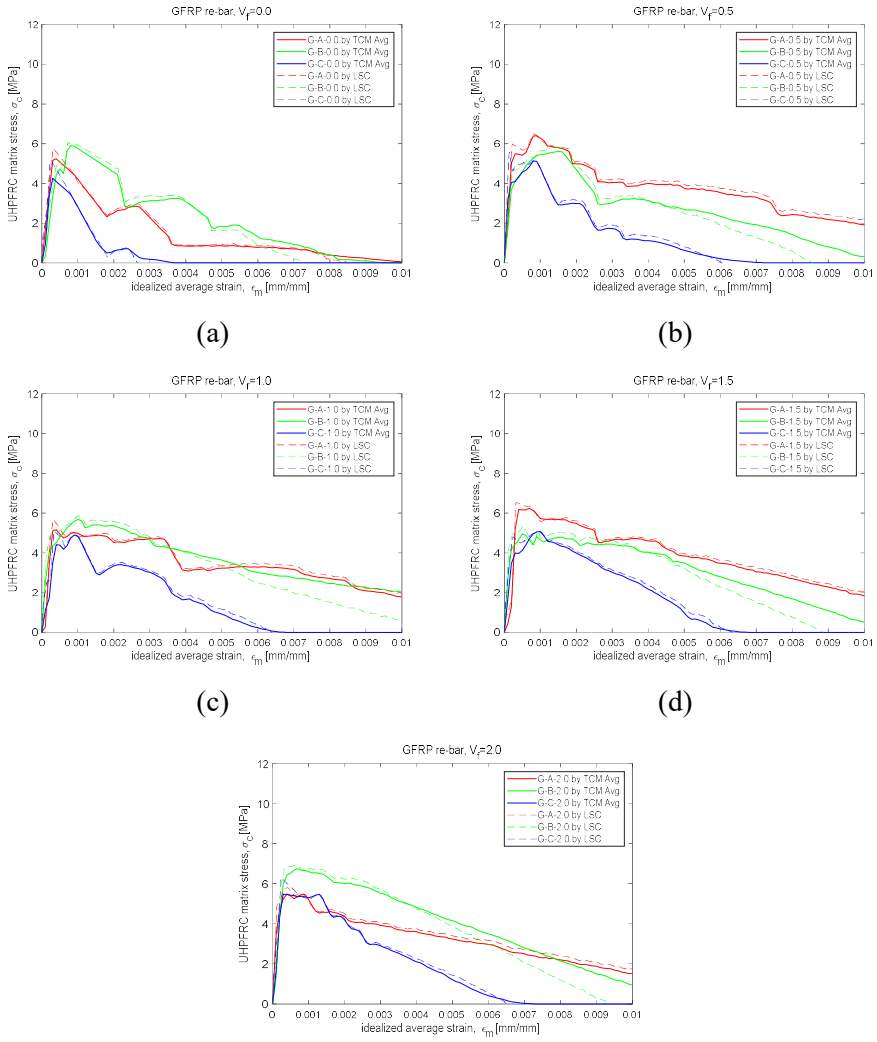

Figure 5-13 Average tensile contribution of UHPFRC matrix of crack element in specimen reinforced with GFRP re-bar by Tension Chord Model compared to Load Sharing Concept, steel fiber volume ratio: (a) 0.0% (b) 0.5% (c) 1.0% (d) 1.5% (e) 2.0%

5.3.2 Tension Stiffening Effect by Tension Chord Model for Steel Re-bar

Steel re-bar reinforced UHPFRC on the otherhand, is considered appropriate to follow the conventional Tension Chord Model. The bond shear stresses before, τ_{b0} ($\sigma_s \leq f_{sy}$) and after, τ_{b1} ($f_{sy} \leq \sigma_s$) the re-bar yields are modeled using **Eq. (5.11)** and **(5.12)**, respectively, where, f_{ct} represents the tensile strength of concrete.

$$\tau_{b0} = 2f_{ct} \tag{5.11}$$

$$\tau_{b1} = \frac{\tau_{b0}}{2} \tag{5.12}$$

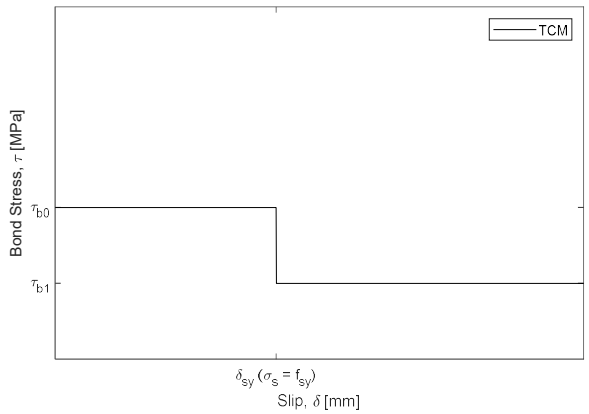

Figure 5-14 Mean bond stress model for steel re-bar

Steel re-bar stress-strain behavior needed to be modified to achieve elastic modulus, E_s and hardening modulus, E_{sh} of steel re-bar respectively as shown in **Figure 5-15**.

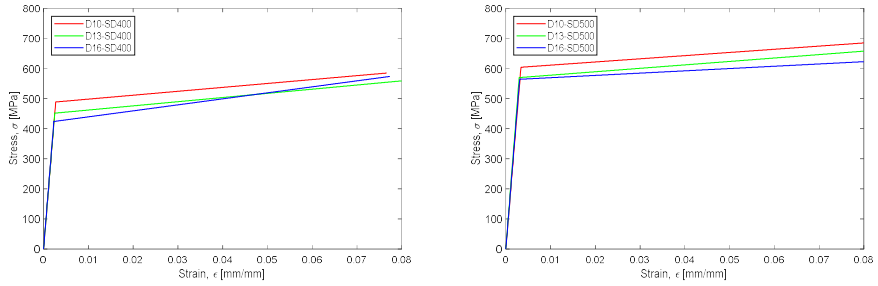

(a) (b)

Figure 5-15 Modeled stress-strain behavior of steel re-bar (a) SD400 series (b) SD500 series

In Case I, the steel re-bar stress, σ_s, has not yet reached its yield stress, f_{sy}. Under this condition, the bond stress distribution along the chord element remains constant, represented by τ_{b0}, which leads to a consistent slope of the reinforcement stress distribution, $4\tau_{b0}/\phi_f$.

On the other hand, Case II refers to the condition where the stress in the steel re-bar has surpassed the yield stress. In this case, when the rebar stress at the crack, $\sigma_{s,r}$ exceeds the yield stress, f_{sy}, the reinforcement stress distribution along the chord element is divided into two segments with varying slopes due to the changes in bond stresses. Specifically, after the stress in the steel re-bar has exceeded the yield stress, f_{sy} a constant bond stress distribution of τ_{b1} can be observed along the re-bar that has yielded near the crack with a reinforcement stress distribution that maintains a constant slope, $4\tau_{b1}/\phi_f$. However, the remaining part of the chord element is characterized by a constant

bond stress distribution of τ_{b0} along the re-bar prior to yielding with a reinforcement stress distribution of consistent slope, $4\tau_{b0} / \phi_f$. **Figure 5-16 (a)** and **(b)** depict the tensile stress experienced by the steel re-bar in the crack element in Case I and II, respectively.

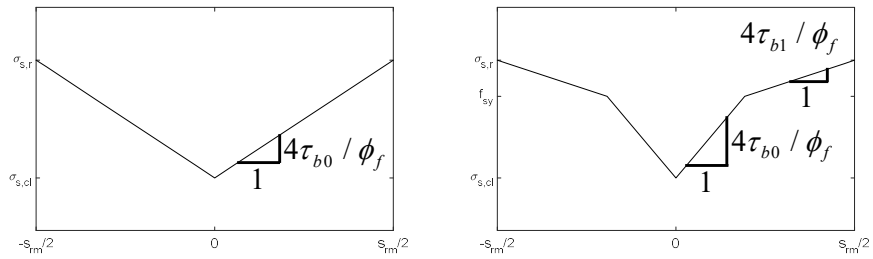

(a) (b)

Figure 5-16 Stress distribution of steel re-bar in Tension Chord Model:

(a) Case I ($\sigma_s \le f_{sy}$) (b) Case II ($f_{sy} \le \sigma_s$)

Mean bond stress models for D10, D13 and D16 SD400 steel re-bar is shown in **Figure 5-17, 5-19** and **5-21** respectively. The slip, δ_{sy} that steel re-bar starts to yield depends on the length of crack element, s_{rm}.

$$\delta_{sy} = \frac{s_{rm}}{2}\varepsilon_{sy} \tag{5.13}$$

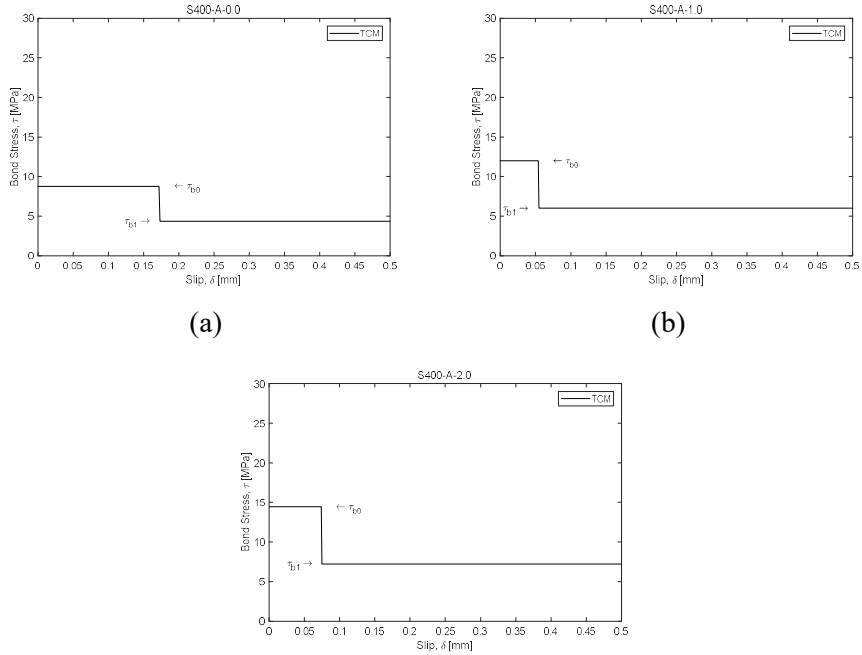

Figure 5-17 Mean bond stress model for D10 SD400 steel re-bar, steel fiber volume ratio: (a) 0.0% (b) 1.0% (c) 2.0%

Maximum and average tensile contribution of UHPFRC matrix by strain in entire crack element in specimen reinforced with D10 SD400 re-bar by Tension Chord Model is described in **Figure 5-18**. As the steel fiber volume ratio increases, the length of the crack element decreases, but the contribution of the UHPFRC matrix increases i.e, the tension stiffening effect increases.

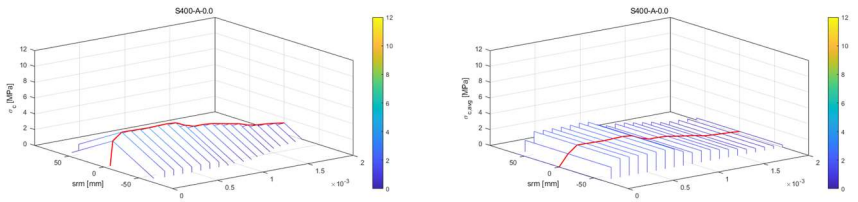

(a)

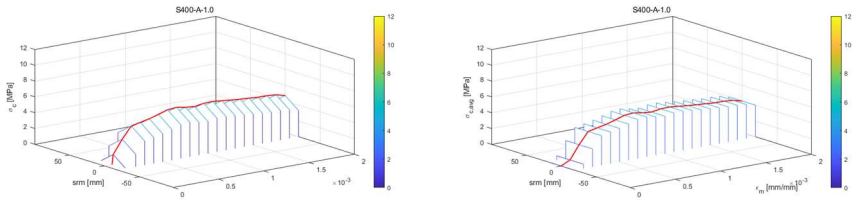

(b)

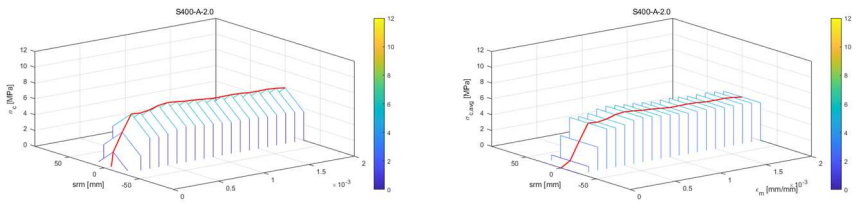

(c)

Figure 5-18 Maximum(left) and average(right) tensile contribution of UHPFRC matrix by strain in entire crack element in specimen reinforced with D10 SD400 steel re-bar by Tension Chord Model, steel fiber volume ratio: (a) 0.0% (b) 1.0% (c) 2.0%

Maximum and average tensile contribution of UHPFRC matrix by strain in entire crack element in specimen reinforced with D13 SD400 steel re-bar by Tension Chord Model is described in **Figure 5-20**. The length of the crack element decreases as the steel fiber volume ratio increases. The overall tensile contribution of the UHPFRC matrix decreases compared to the series of D10

SD400 steel re-bars when the steel fiber volume ratio is low. Also, the increase in tension stiffening effect is not as significant as that observed in the series of D10 SD400 steel re-bars as the steel fiber volume ratio increase.

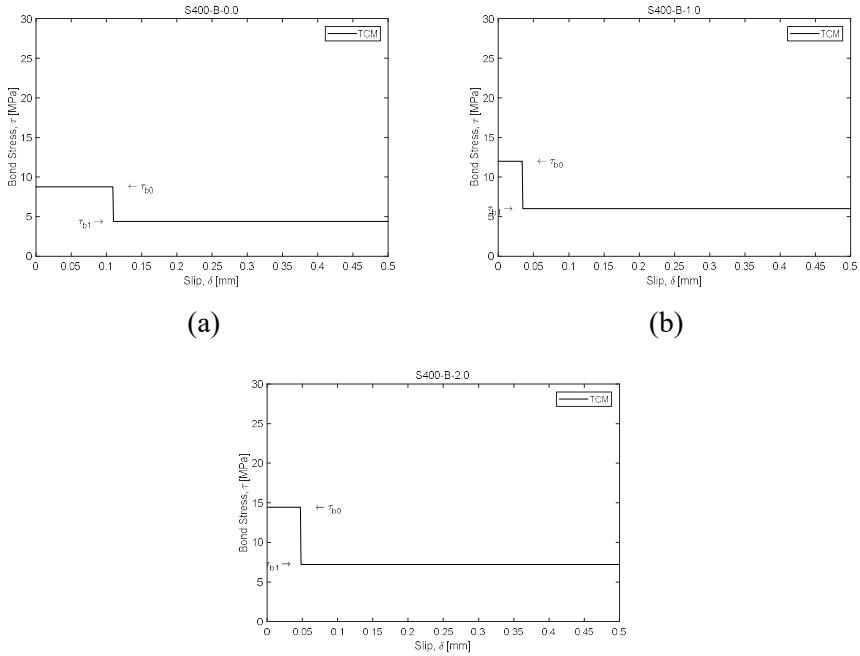

Figure 5-19 Mean bond stress model for D13 SD400 steel re-bar, steel fiber volume ratio: (a) 0.0% (b) 1.0% (c) 2.0%

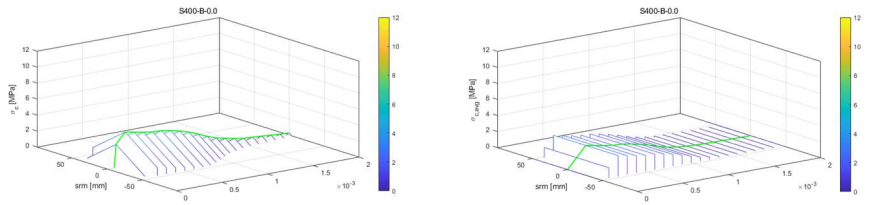

(a)

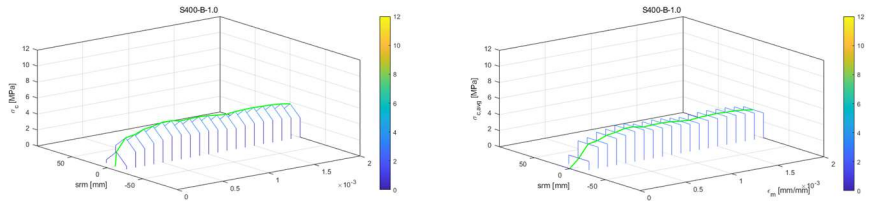

(b)

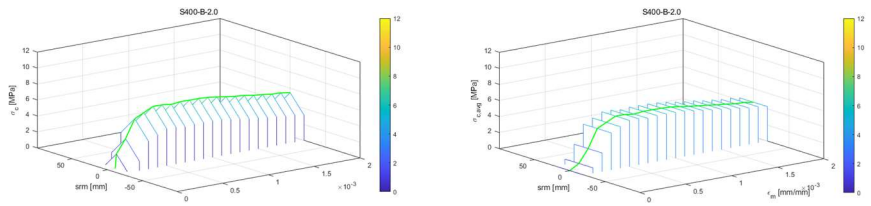

(c)

Figure 5-20 Maximum(left) and average(right) tensile contribution of UHPFRC matrix by strain in entire crack element in specimen reinforced with D13 SD400 steel re-bar by Tension Chord Model, steel fiber volume ratio: (a) 0.0% (b) 1.0% (c) 2.0%

Maximum and average tensile contribution of UHPFRC matrix by strain in specimen reinforced with D16 SD400 steel re-bar by Tension Chord Model is described in **Figure 5-22**. The increase in steel fiber volume ratio results in a similar pattern of increase in the tensile contribution of the UHPFRC matrix as observed in the series of D10 and D13 SD400 steel re-bars. However, the

overall tensile contribution of the UHPFRC matrix decreases even more in comparison to the series of D13 SD400 steel re-bars when the steel fiber volume ratio is low.

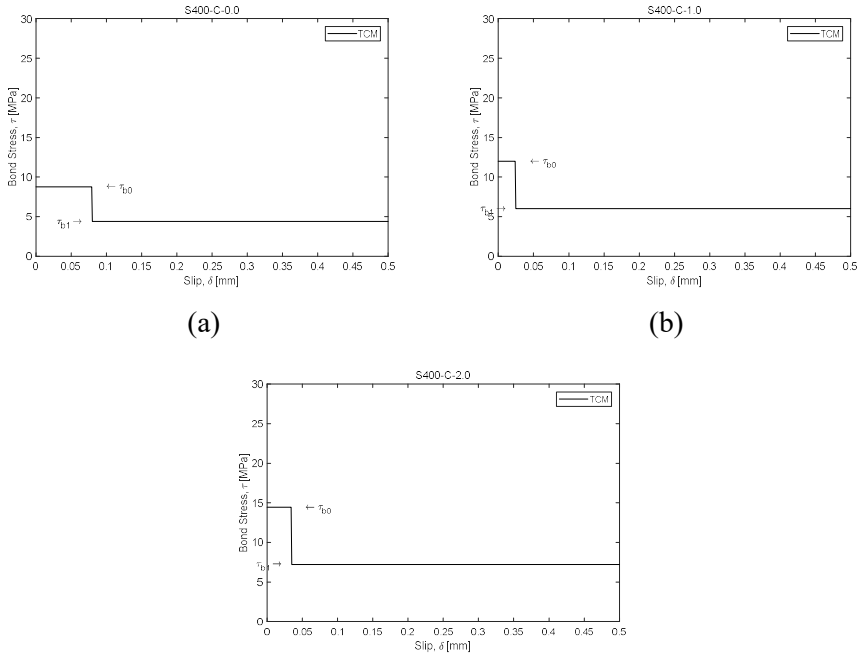

Figure 5-21 Mean bond stress model for D16 SD400 steel re-bar, steel fiber volume ratio: (a) 0.0% (b) 1.0% (c) 2.0%

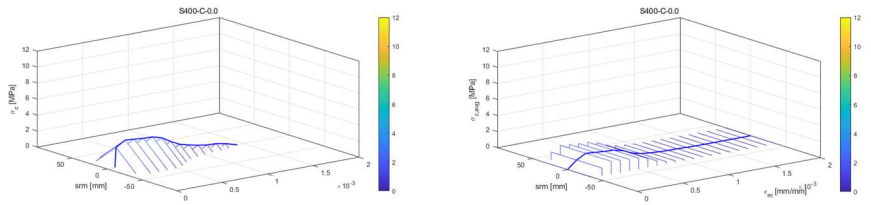

(a)

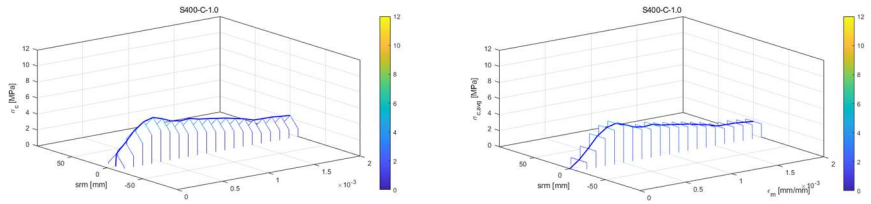

(b)

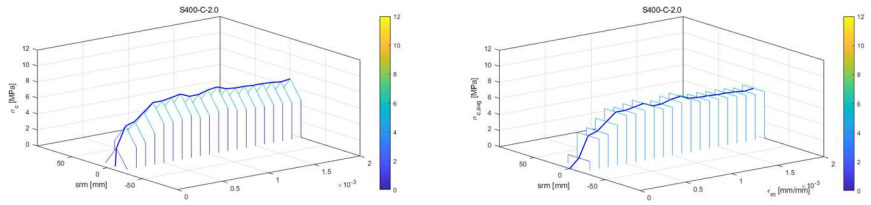

(c)

Figure 5-22 Maximum(left) and average(right) tensile contribution of UHPFRC matrix by strain in entire crack element in specimen reinforced with D16 SD400 steel re-bar by Tension Chord Model, steel fiber volume ratio: (a) 0.0% (b) 1.0% (c) 2.0%

The overall comparison of tensile contribution of the UHPFRC matrix UHPFRC matrix of crack element in specimen reinforced with SD400 steel re-bar is depicted in **Figure 5-23**. Increasing steel fiber volume ratio enhances tension stiffening effect of UHPFRC matrix due to improved bond strength. Similar as GFRP series, larger re-bar diameter results in lower tensile

contribution UHPFRC matrix due to weaker bond strength compared to re-bar strength, only the the effect is lower. The increase in steel fiber volume ratio has a more significant impact on tension stiffening in specimens with lower reinforcement ratios, indicating a stronger effect in re-bars with smaller diameters even at low steel fiber volume ratios.

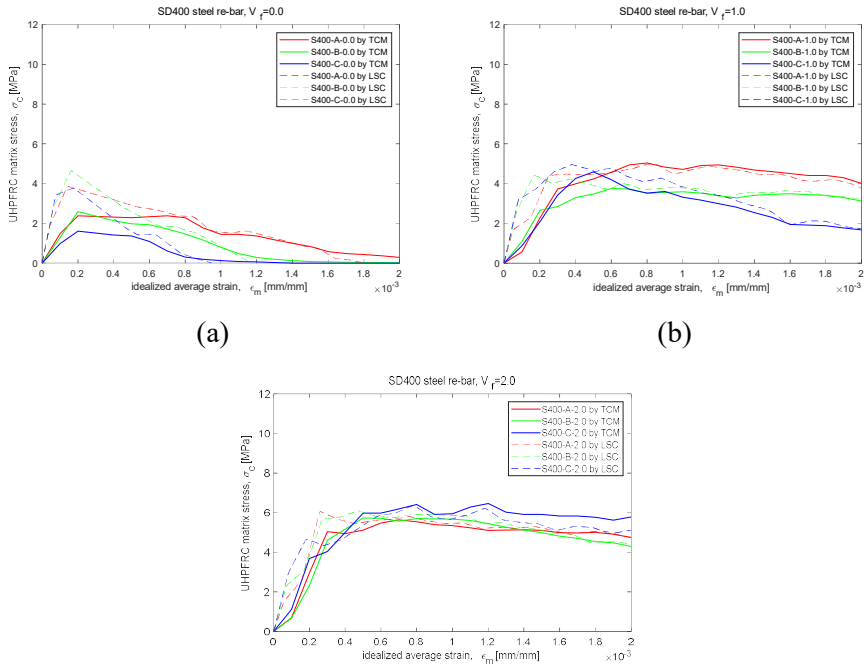

Figure 5-23 Average tensile contribution of UHPFRC matrix of crack element in specimen reinforced with SD400 steel re-bar by Tension Chord Model compared to Load Sharing Concept, steel fiber volume ratio: (a) 0.0% (b) 1.0% (c) 2.0%

Mean bond stress models for D10, D13 and D16 SD500 steel re-bar is shown in **Figure 5-24, 5-26** and **5-28** respectively. The slip, δ_{sy} that steel re-bar starts to yield depends on the length of crack element, s_{rm} as well.

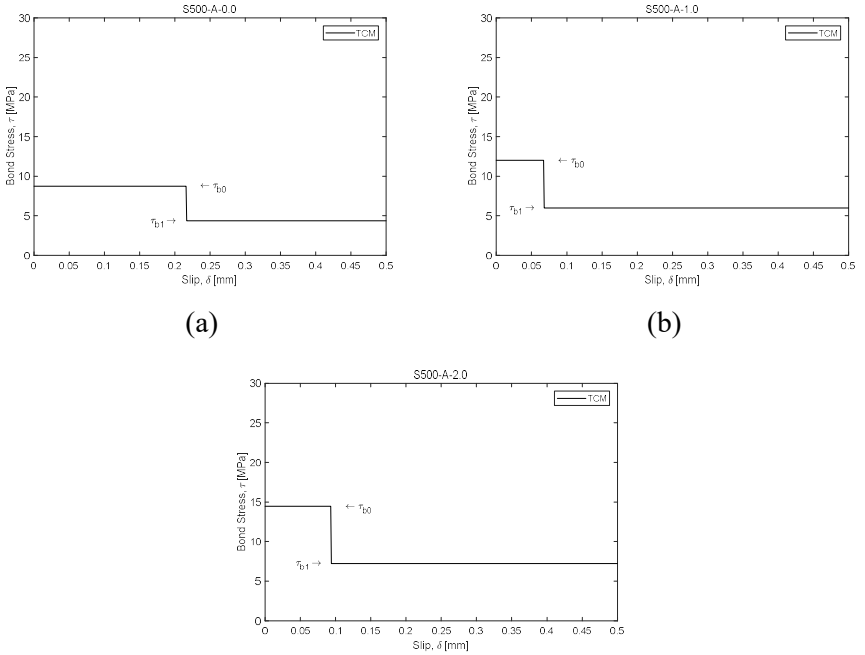

(a) (b)

(c)

Figure 5-24 Mean bond stress model for D10 SD500 steel re-bar, steel fiber volume ratio: (a) 0.0% (b) 1.0% (c) 2.0%

Maximum and average tensile contribution of UHPFRC matrix by strain in entire crack element in specimen reinforced with D10 SD500 re-bar by Tension Chord Model is described in **Figure 5-25**. The tension stiffening effect

observed in UHPFRC reinforced with steel re-bars shows a similar pattern to that observed in UHPFRC reinforced with SD400 steel re-bars, as the effect increases with the volume ratio of steel fiber.

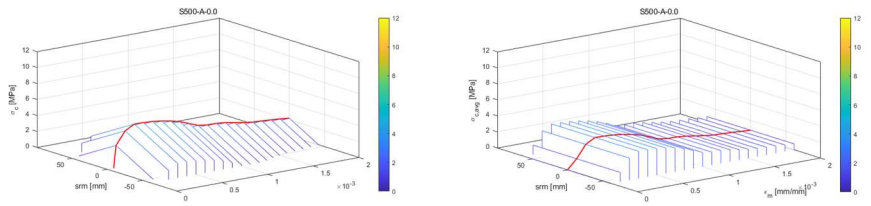

(a)

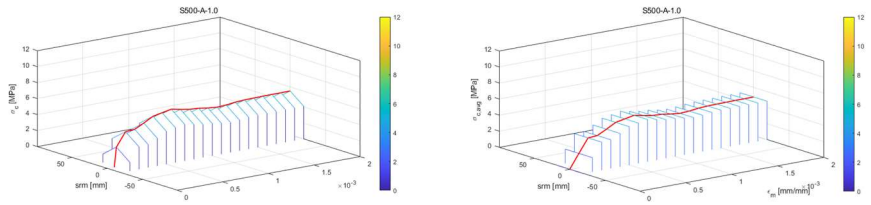

(b)

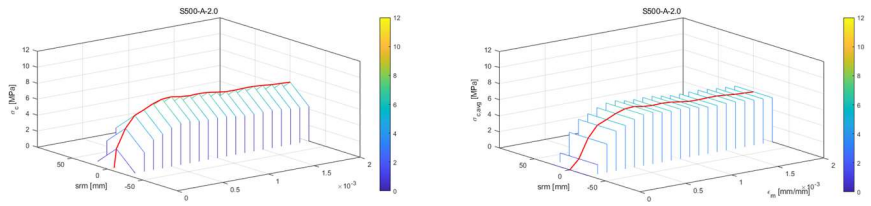

(c)

Figure 5-25 Maximum(left) and average(right) tensile contribution of UHPFRC matrix by strain in entire crack element in specimen reinforced with D10 SD500 steel re-bar by Tension Chord Model, steel fiber volume ratio: (a) 0.0% (b) 1.0% (c) 2.0%

Maximum and average tensile contribution of UHPFRC matrix by strain in entire crack element in specimen reinforced with D13 SD500 steel re-bar by Tension Chord Model is described in **Figure 5-27**. The overall tensile contribution of the UHPFRC matrix remains relatively unchanged in comparison to D10 SD500 steel re-bars, and the improvement in tension stiffening effect is also comparable.

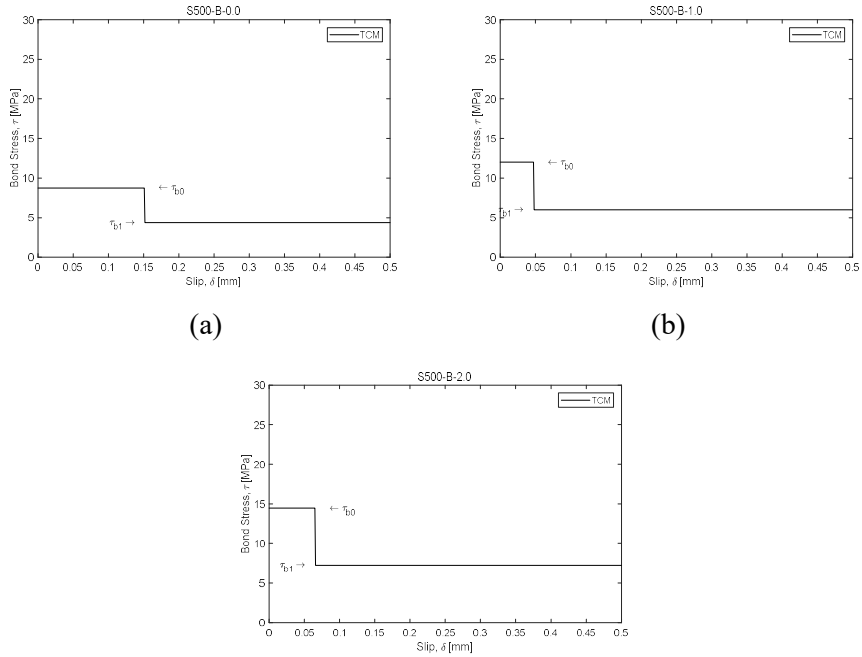

(a) (b)

(c)

Figure 5-26 Mean bond stress model for D13 SD500 steel re-bar by applying CMR model, steel fiber volume ratio: (a) 0.0% (b) 1.0% (c) 2.0%

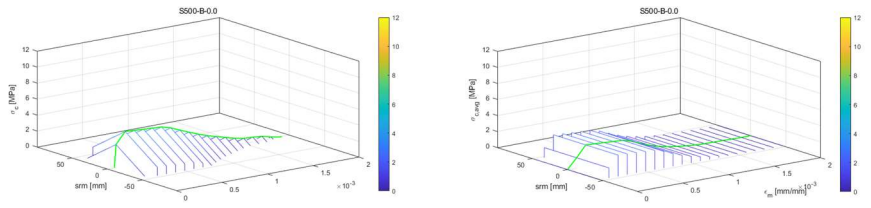

(a)

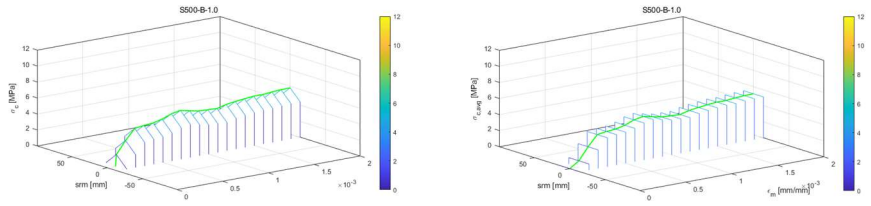

(b)

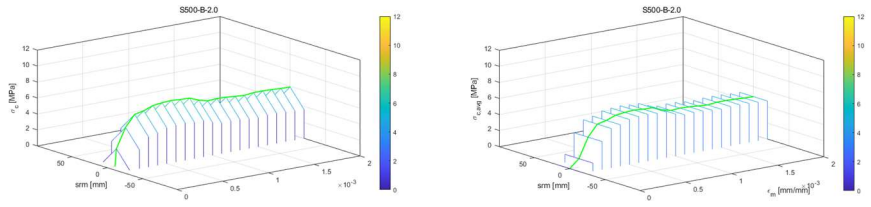

(c)

Figure 5-27 Maximum(left) and average(right) tensile contribution of UHPFRC matrix by strain in entire crack element in specimen reinforced with D13 SD500 steel re-bar by Tension Chord Model, steel fiber volume ratio: (a) 0.0% (b) 1.0% (c) 2.0%

Maximum and average tensile contribution of UHPFRC matrix by strain in specimen reinforced with D16 SD500 steel re-bar by Tension Chord Model is described in **Figure 5-29**. Similar to the D10 and D13 SD500 steel re-bar series, the overall tensile contribution of the UHPFRC matrix remains consistent.

As the steel fiber volume ratio is increased, a similar tension stiffening effect pattern, characterized by an increase in the tension stiffening effect, is observed in the specimens reinforced with SD400 steel re-bars. However, there is a small difference in the tension stiffening effect between re-bars with large diameters and those with small diameters.

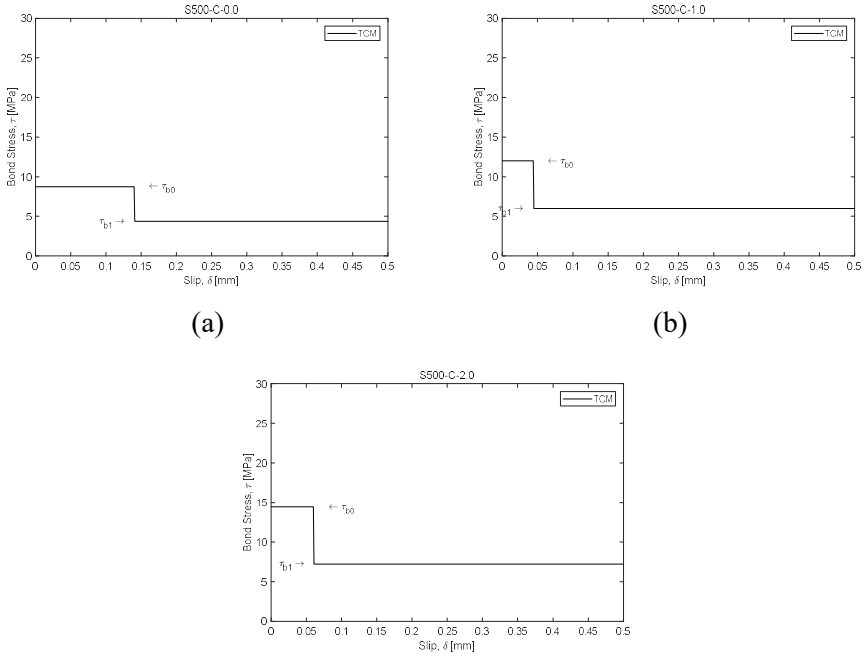

(a) (b)

(c)

Figure 5-28 Mean bond stress model for D16 SD500 steel re-bar by applying CMR model, steel fiber volume ratio: (a) 0.0% (b) 1.0% (c) 2.0%

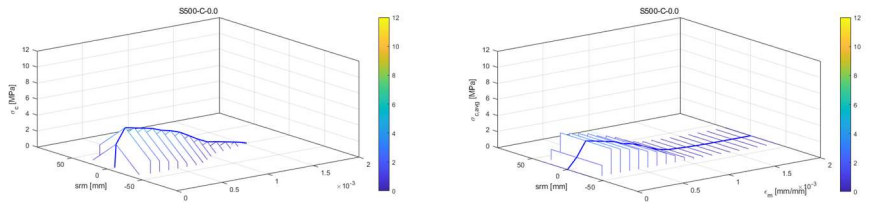

(a)

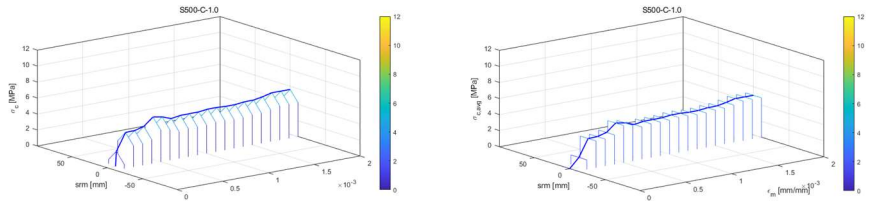

(b)

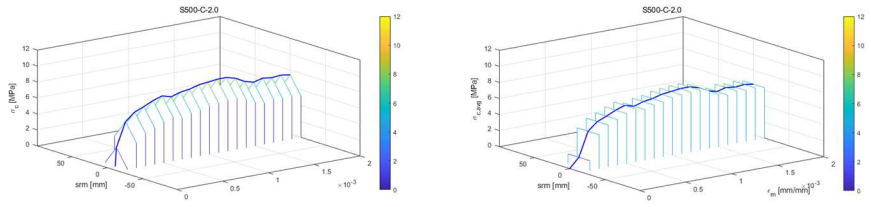

(c)

Figure 5-29 Maximum(left) and average(right) tensile contribution of UHPFRC matrix by strain in entire crack element in specimen reinforced with D16 SD500 steel re-bar by Tension Chord Model, steel fiber volume ratio: (a) 0.0% (b) 1.0% (c) 2.0%

The overall comparison of tensile contribution of the UHPFRC matrix UHPFRC matrix of crack element in specimen reinforced with SD500 steel re-bar is depicted in **Figure 5-30**. Increasing steel fiber volume ratio enhances UHPFRC matrix tension stiffening effect via improved bond strength, while larger re-bar diameter results in weaker bond strength compared to re-bar

strength and lower tensile contribution of UHPFRC matrix. Higher steel fiber volume ratio has a greater impact on tension stiffening in specimens with lower reinforcement ratios, indicating a stronger effect in smaller diameter re-bars even at low steel fiber volume ratios. The characteristics of the improvements in tension stiffening effect by the change of steel fiber volume ratio are similar between the specimens reinforced with SD400 and SD500 steel re-bars.

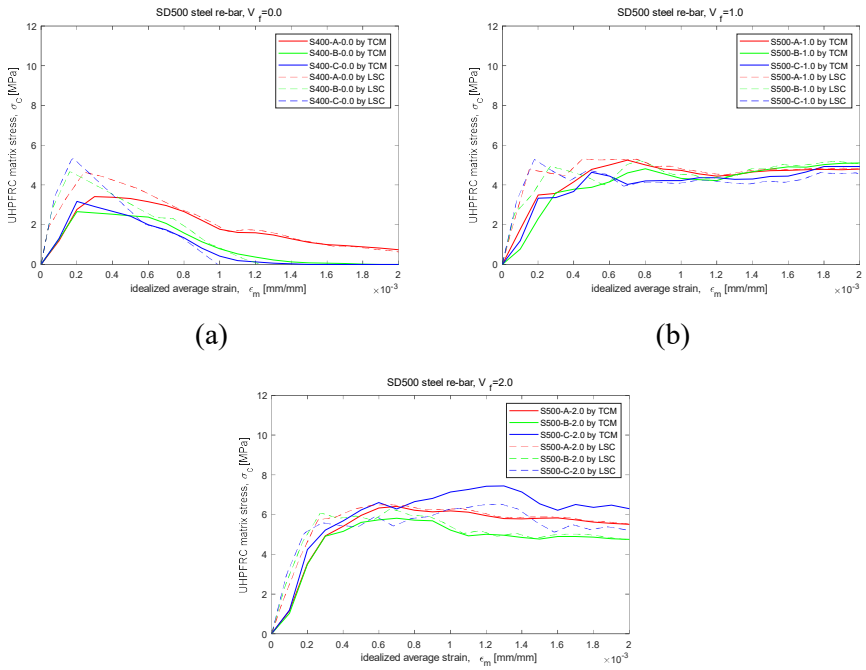

Figure 5-30 Average tensile contribution of UHPFRC matrix of crack element in specimen reinforced with SD500 steel re-bar by Tension Chord Model compared to Load Sharing Concept, steel fiber volume ratio: (a) 0.0% (b) 1.0% (c) 2.0%

5.4 Bond Factor

The bond factor, represented by β, is a normalized value that is calculated by dividing the average tensile stress of concrete by the cracking stress. It indicates the average stress or load that the cracked concrete is able to sustain, and is a measure of the average tensile stress in the UHPFRC matrix, reflecting the material's tension stiffening capability. The variation in tension-stiffening bond factor among UHPFRCs with different steel fiber volume ratios can be mainly attributed to the tension carried by the steel fibers at the cracks. The addition of steel fiber to concrete can also enhance tension stiffening performance, particularly in cases where split cracking is a concern (Abrishami and Mitchell [21]). This is achieved by delaying or preventing the degradation of bond strength between the reinforcement bars and the UHPFRC matrix.

The general relationship for tension stiffening of UHPFRC reinforced with GFRP, SD400 steel, and SD500 steel re-bar at various steel fiber volume ratios is depicted in **Figures 5-33, 5-32**, and **5-33**, respectively. The tension stiffening effect is significantly influenced by the diameter of the re-bar. As the diameter of the re-bar increases, the cover thickness decreases, which leads to more splitting cracks and decrease in bond strength. As confirmed in section 3.3, an increase in the steel fiber volume ratio can prevent splitting cracks and improve the tension stiffening effect effectively.

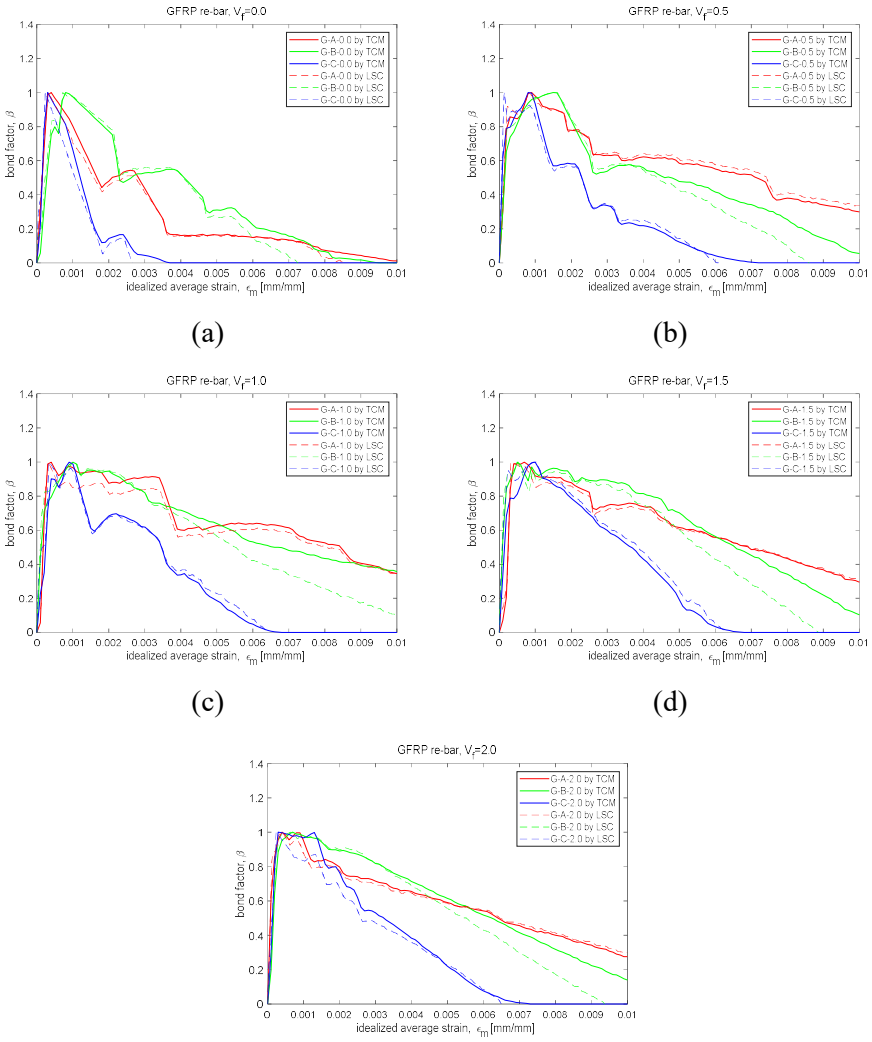

Figure 5-31 Comparison of bond factor, β in specimen reinforced with GFRP re-bar by Tension Chord Model and Load Sharing Concept, steel fiber volume ratio: (a) 0.0% (b) 0.5% (c) 1.0% (d) 1.5% (e) 2.0%

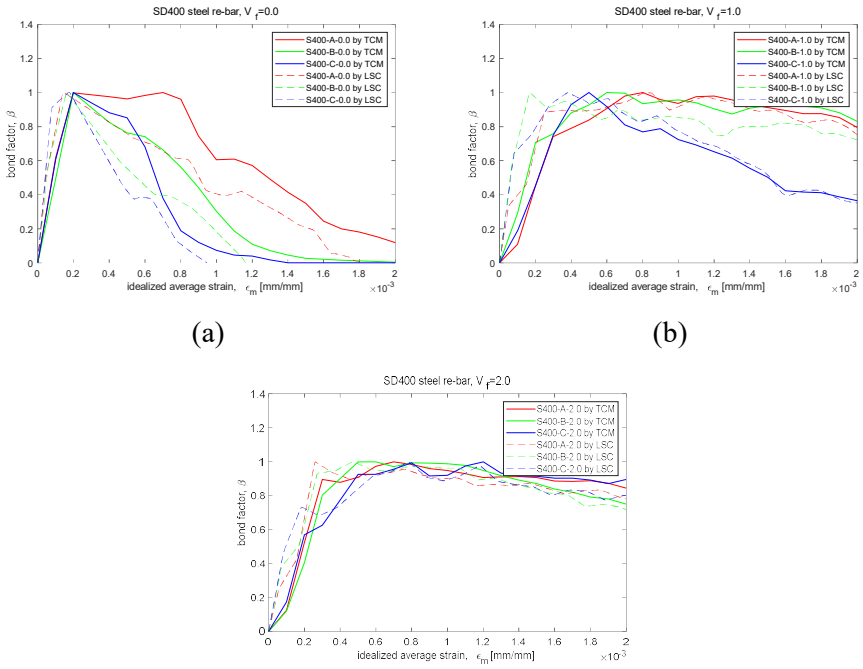

Figure 5-32 Comparison of bond factor, β in specimen reinforced with SD400 steel re-bar by Tension Chord Model and Load Sharing Concept, steel fiber volume ratio: (a) 0.0% (b) 1.0% (c) 2.0%

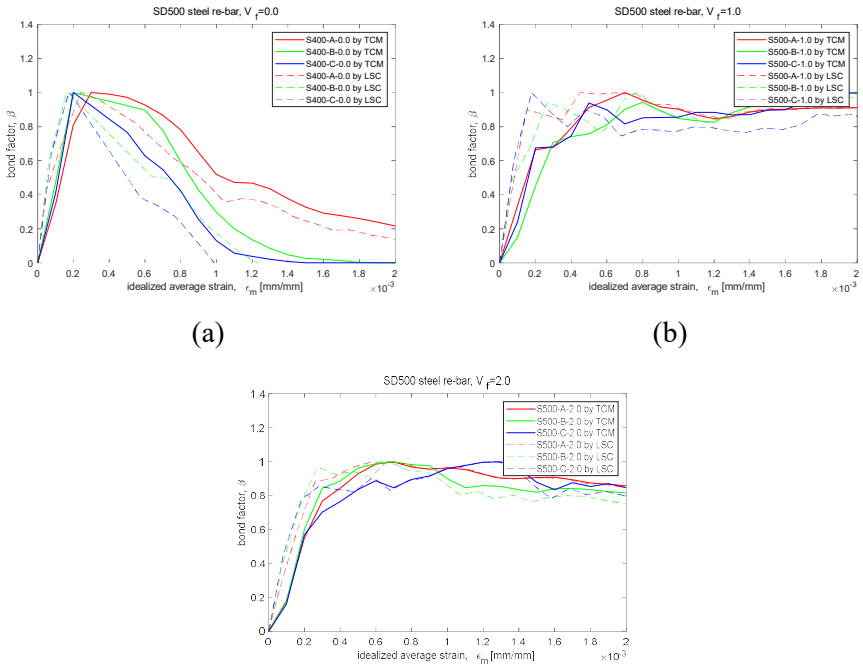

Figure 5-33 Comparison of bond factor, β in specimen reinforced with SD500 steel re-bar by Tension Chord Model and Load Sharing Concept, steel fiber volume ratio: (a) 0.0% (b) 1.0% (c) 2.0%

5.5 Tension Stiffening Effect Comparison Between UHPFRC and NRC

Tension stiffening effect is also compared between R-UHPFRC and NRC. Comparison of both tensile contribution and energy density absorbtion by UHPFRC and NRC matrix are made.

5.5.1 Tensile Contribution of NRC

Tensile contribution of NRC is derived by using model proposed by Bischoff et al. [22], which is described in **Eq. (5.14)**. E_b is the elastic modulus [GPa] of the re-bar. Since bond factor, β is a normalized value, the theoretical tensile contribution can be derived by multiplying cracking stress, f_{cr} of normal concrete.

$$\beta = \exp[-1100(\varepsilon_m - \varepsilon_{cr})(E_b / 200)] \tag{5.14}$$

$$f_{cr} = 0.37\sqrt{f_c'} \tag{5.15}$$

In this study, the cracking strain, ε_{cr} is considered as 0.0002 and f_{cr} is derived as **Eq. (5.15)**, where f_c' is considered as 40MPa [22]. Comparison of tensile contribution of UHPC and NRC matrix is shown in **Figure 5-34**. The initial cracking stress of both UHPC and NRC are shown as well as tensile contributions. It is evident that NRC exhibits lower initial cracking stresses in all re-bar types. However, the tensile contribution model employed for NRC does not adequately reflect the pull-out effect observed in the test results of this study. Instead of dropping below zero, the model tends to converge to zero.

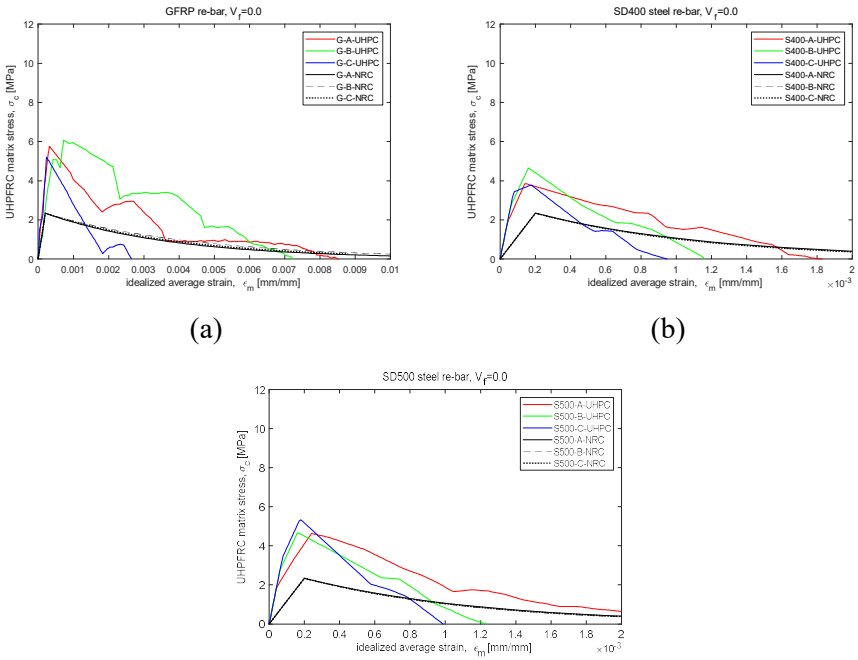

Figure 5-34 Comparison of tensile contribution of UHPC and NRC matrix reinforced with: (a) GFRP re-bar (b) SD400 steel re-bar (c) SD500 steel re-bar

5.5.2 Energy Density Absorbed by UHPFRC and NRC Matrix

The energy density, which represents the energy per unit volume, can be determined by integrating the stress-strain curve to calculate the area beneath the curve. The total magnitude of the tension stiffening effect can be quantified as the energy density absorbed within the UHPFRC and NRC matrix.

The overall energy density absorbed in UHPFRC and NRC matrix neglecting contribution of GFRP re-bar is shown in **Figure 5-35.** It can be seen that the effect of increase in steel fiber volume ratio is large for re-bar with small diameter. The G10-GFRP re-bar series attained the highest value and sustained it beyond a steel fiber volume ratio of 0.5%. In contrast, the G13 and G16 re-bar series required a higher volume ratio of steel fiber to achieve enhanced results.

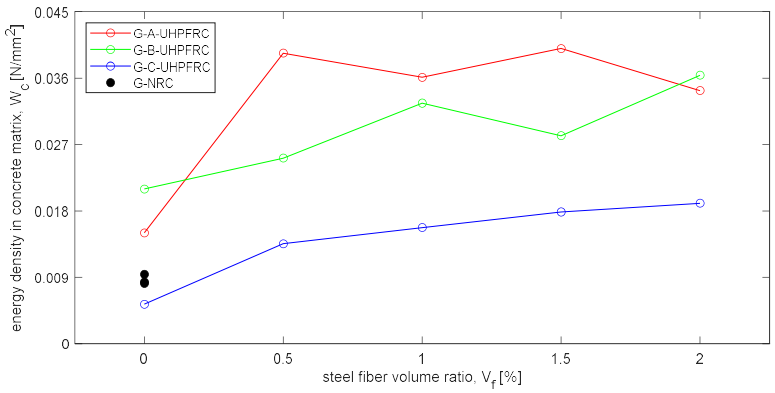

Figure 5-35 Energy density absorbed in UHPFRC and NRC martrix of specimens with GFRP re-bars

Figure 5-36 illustrates the overall energy density absorbed in the UHPFRC matrix, excluding the contribution of SD400 and SD500 steel re-bar. It can be observed that the increase in steel fiber volume ratio has a significant impact on re-bars with small diameter, similar to the GFRP re-bar series. Notably, the range of the elastic state, is larger for steel re-bar with larger values of yield strain, ε_{sy}. As a result, the energy density of the SD500 steel re-bar series exceeds that of the SD400 steel re-bar series.

Table 5-4 The yield strain, ε_{sy} in SD400 and SD500 steel re-bar

Re-bar type	ε_{sy}
S400-A	0.0027
S400-B	0.0025
S400-C	0.0023
S500-A	0.0032
S500-B	0.003
S500-C	0.003

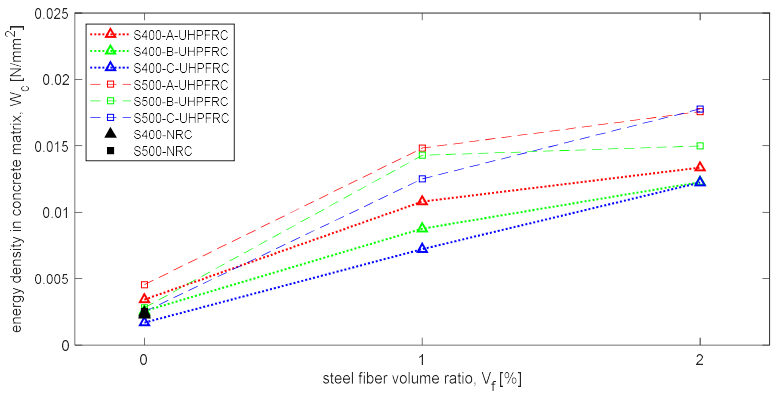

Figure 5-36 Energy density absorbed in UHPFRC and NRC martrix of specimens with SD400 and SD500 steel re-bars respectively

Figure 5-35 and **Figure 5-36** shows that compared to NRC matrix, it is clearly observed that UHPFRC matrix can absorb larger values of energy density. This observation holds true even for the G-C and S400-C series, although the UHPFRC matrix absorbs a smaller amount of energy density than the NRC matrix when considering the pull-out effect.

5.6 Conclusion

This chapter provides a comparative analysis of the tension stiffening effect among various variables in UHPFRC. The study utilized two approaches: the simple subtraction of bare re-bar response from the measured member response and the Tension Chord Model. Through these methods, the overall tension stiffening effect in a member's response was examined, along with a detailed analysis of the decomposed UHPFRC matrix tensile contribution in a crack element considering variations in bond strength due to the type of re-bar and steel fiber volume ratio. The study reveals dissimilarities in the tensile behavior between GFRP rebar and steel rebar, necessitating different approaches for applying the Tension Chord Model to each material. While the conventional Tension Chord Model sufficed for the steel re-bar series, a modified model incorporating the CMR model was required for the GFRP re-bar series.

Despite the different approaches used, the results obtained from both methods showcased a similar general relationship for tension stiffening in UHPFRC reinforced with GFRP, SD400 steel, and SD500 steel re-bar at various steel fiber volume ratios. The increase in steel fiber volume ratio was found to enhance the tension stiffening effect with a more significant impact observed for re-bar with smaller diameters. As the diameter of the re-bar increases, the effectiveness of the tension stiffening effect decreases, possibly due to a decrease in bond strength relative to the tensile strength of the re-bar. This phenomenon is expected to occur in the GFRP re-bar series, as the bond stress is generally lower for GFRP re-bars compared to steel re-bars. Furthermore, as the re-bar diameter increased, the reduction in cover thickness

led to more splitting cracks and a decrease in bond strength. On the other hand, an increase in the steel fiber volume ratio proved effective in preventing splitting cracks and improving the tension stiffening effect.

Chapter 6. Application of Design Standard

6.1 Crack Control

The limitation of the maximum crack width is a crucial consideration in service design. The crack width is influenced by the crack spacing s_{rm}, which is determined by the initial crack formation and decreases as the post-cracking strength increases. It is also affected by the model parameter λ. Furthermore, the value of may vary during the loading process due to the potential for progressive cracking. Therefore, a value of $\lambda = 1$ does not necessarily result in larger crack spacing at the end of progressive cracking (Valente et al. [14]).

The design of GFRP-reinforced concrete is often governed by serviceability requirements, as the stress in GFRP bars under service load needs to be limited to a relatively small proportion of the bar strength in order to control crack width. In contrast, controlling crack width in steel re-bar reinforced concrete is driven by concerns about corrosion. Unlike steel re-bars, GFRP bars are not susceptible to corrosion, allowing for wider crack widths to be tolerated (Newhook et al. [23]). Standards such as CAN/CSA S806 [24] permit crack widths of 0.7 mm and 0.5 mm for interior and exterior exposure, respectively, while the French Standard NF P 18-710 [25] servicability limit states, based on Eurocode 2, allows for a maximum crack width of 0.3 mm, **Table 6-1**.

Table 6-1 Design standards for the maximum crack width, w_{max} of tensile members reinforced with GFRP and steel re-bar by exposure

CSA Standard S806-02 (GFRP)	French Standard NF P 18-710 (Steel)
Interior: $w_{max} = 0.7mm$ Exterior: $w_{max} = 0.5mm$	X0, XC1 (no risk of corrosion or very dry): $w_{max} = 0.3mm$ XC2, XC3, XC4 (corrosion by carbonation): $w_{max} = 0.2mm$ XD1, XD2, XD3, XS1, XS2, XS3 (corrosion by chloride): $w_{max} = 0.1mm$

As can be seen in **Figure 3-21** and **Figure 3-22**, the crack width and spacing can be controlled by adjusting reinforcement ratio and steel fiber volume ratio. Since the secimens reinforced with small reinforcement ratio of GFRP re-bar tend to have large values of crack width exceeding the standard even at the cracking load, enough steel fiber volume ratio can be used to effectively reduce the crack width.

6.2 Development Length

One of the primary challenges associated with using GFRP re-bars arises from their low bond strength. This issue is addressed in Chapter 3 and 5, where it is noted that the lack of bond strength is the reason behind the development of design standards, such as CAN/CSA S806 [24], which focus on ensuring sufficient bond strength without the risk of pull-out. In contrast, standards for the development length of steel re-bars are applied by the Korea Concrete Institute [26].

Table 6-2 Design standards for the development length, l_d of GFRP and steel re-bars in tension

CSA Standard S806-02 (GFRP)	Korea Concrete Institute (Steel)
Normal requirement: $l_d = 1.15 \frac{k_1 k_2 k_3 k_4 k_5}{d_{cs}} \frac{f_F}{\sqrt{f_c'}} A_b$ d_{cs} shall not be larger than $2.5 d_b$ Premitted variation: $l_d = 0.5 k_1 k_2 k_3 k_4 k_5 \frac{f_F}{\sqrt{f_c'}} d_b$ Clear cover and clear spacing of the bars being developed are at least $1.5 d_b$ and $1.8 d_b$ *maximum permissible value of $\sqrt{f_c'}$: $8 MPa$	Basic development length: $l_{bd} = \frac{0.186 d_b f_{yk}}{\phi_m f_c'}$ *minimum permissible value of l_d : $5.5 d_b$ f_{yk} = steel re-bar design yield stress ϕ_m = material reduction factor, generally 0.77 Development length: l_d = modification factor $\times l_{bd}$ modification factor: The case when spacing between the developed reinforcing bars is equal to or greater than d_b, and the cover thickness

f_F = FRP design tensile stress at ULS k_1 = Bar location factor 1.3: horizontal reinforcement placed so that more than 300 mm of fresh concrete is cast in the 1 member below the development length or splice 1.0: other cases k_2 = Concrete density factor 1.3: structural low-density concrete 1.2: structural semi-low-density concrete 1.0: normal density concrete k_3 = Bar size factor 0.8: $A_b \le 300mm^2$ 1.0: $A_b > 300mm^2$ k_4 = Bar fiber factor 1.0: CFRP and GFRP 1.25: AFRP k_5 = Bar surface profile factor The bar surface profile factor may be taken as less than 1.0, but not less than 0.5, if this value has been shown by experiment. In the absence of direct experimental values, the following values shall be used: 1.0: surface-roughened or sand-coated surfaces 1.05: spiral pattern surfaces 1.0: braided surfaces 1.05: ribbed surfaces 1.80: indented surfaces	is also equal to or greater than d_b, and a minimum amount of stirrups or hoop reinforcement is placed throughout the entire length l_d. The spacing between the anchored reinforcing bars is equal to or greater than $2d_b$, and the cover thickness is equal to or greater than d_b. 0.8α : D19 steel re-bar or smaller α : D22 steel re-bar or larger Other cases 1.2α : D19 steel re-bar or smaller 1.5α : D22 steel re-bar or larger Upper reinforcement (Horizontal reinforcement where concrete is poured below less than 300mm from the development legnth): $\alpha = 1.3$ Other reinforcement $\alpha = 1.0$

Chapter 7. Concluding Remarks

7.1 Summary

This study investigates the uniaxial tensile behavior of reinforced ultra-high-performance-fiber-reinforced-concrete (R-UHPFRC) and compares the effects of changes in steel fiber volume ratio and rebar type, such as GFRP and steel.

The findings indicate that different factors contribute to various types of re-bar failure, resulting in distinct patterns in ultimate stress. In the GFRP re-bar series, the ultimate tensile stress increases as the steel fiber volume ratio rises when specimens fail by pull-out, due to the bond strength between UHPFRC and the re-bar. However, when re-bar rupture occurs, the ultimate tensile stress is limited to the re-bar's tensile strength. Additionally, the increase in reinforcement ratio does not proportionally increase the attachment area, leading to slip caused by a relative reduction in bond strength. In the SD400 and SD500 steel re-bar series, an increase in the steel fiber volume ratio results in higher ultimate tensile stress. Localization of cracks around a single major crack leads to stress concentration on the corresponding part of the re-bar, causing failure at a smaller strain, particularly in the SD500 series at a higher steel fiber volume ratio.

The comparison between the tensile behaviors of members with and without considering the shrinkage effect focuses on the initial cracking stress. It is observed that an increase in re-bar diameter and modulus of elasticity leads to an increase in residual load, while an increase in the steel fiber volume ratio

alleviates the residual load and increases the initial cracking stress. The GFRP re-bar series exhibits the largest shrinkage and lowest residual load, resulting in the highest initial cracking stress when considering the shrinkage effect.

The study employs two approaches, the simple subtraction of bare re-bar response and the Tension Chord Model, to analyze the tension stiffening effect. Both methods demonstrate a similar general relationship for tension stiffening in UHPFRC with GFRP, SD400 steel, and SD500 steel re-bar at various steel fiber volume ratios. The study reveals dissimilarities in tensile behavior between GFRP rebar and steel rebar, necessitating different approaches for each material. An increase in the steel fiber volume ratio enhances the tension stiffening effect, particularly in re-bar with smaller diameters. The effectiveness of the tension stiffening effect diminishes as the re-bar diameter increases due to several reasons such as splitting crack and relative decrease in bond strength. Additionally, the steel fiber volume ratio helps prevent splitting cracks and improves tension stiffening.

7.2 Discussion

Proper use of re-bar for UHPFRC in needed because of its high shrinkage. Moreover, an appropriate volume ratio of steel fiber in UHPFRC can help mitigate the drawbacks associated with the reinforcement materials.

Despite its high strength, GFRP re-bar exhibits a relatively low elastic modulus, leading to increased deflections and crack widths. Consequently, the design of GFRP-reinforced concrete structures is frequently driven by serviceability considerations, with tension stiffening playing a significant role in influencing behavior. While it may be challenging for GFRP re-bar to match the excellent performance of steel re-bar in terms of ductility and performance in the plastic range after initial cracking, this study provides evidence that GFRP re-bar, when used in UHPFRC, achieves comparable and even superior performance compared to steel re-bar in certain aspects. This highlights the potential of GFRP re-bar applied in UHPFRC to provide more favorable outcomes compared to conventional practices.

The low modulus of elasticity in GFRP re-bar mitigates the reduction in initial cracking stress caused by shrinkage-induced residual stress. Additionally, it alleviates the decrease in the tensile contribution of UHPFRC resulting from shrinkage compared to steel re-bar. Also, the presence of steel fibers contributes to tension in the crack plane, playing a significant role in enhancing the tension stiffening effect. By increasing the steel fiber volume ratio, the disadvantage due to the low ductility of GFRP re-bar can be improved. Except for the tension stiffening effect in the elastic range, there were minimal differences observed between the SD400 and SD500 steel re-bar series.

Comparing with NRC, UHPFRC exhibits higher residual stress due to shrinkage, but its strong tensile strength results in a larger tension stiffening effect. Therefore, GFRP, which has lower residual stress due to a small modulus of elasticity and requires a larger tension stiffening effect, is expected to have better usability in UHPFRC compared to NRC. When using GFRP re-bar with a steel fiber volume ratio of low percentage, the crack width in UHPFRC may exceed the specified standards. However, crack control is achievable by increasing the steel fiber volume ratio and reinforcement ratio. Additionally, ensuring an adequate development length is also crucial. GFRP-reinforced UHPFRC is suitable for locations vulnerable to corrosion, places with magnetic effects, and areas where large deflections are tolerated.

References

[1] P. Richard and M. H. Cheyrezy, “Reactive Powder Concretes With High Ductility and 200 - 800 Mpa Compressive Strength,” *SP*, vol. 144, pp. 507–518, Mar. 1994, doi: 10.14359/4536.

[2] C.-C. Hung, H.-S. Lee, and S. N. Chan, “Tension-stiffening effect in steel-reinforced UHPC composites: Constitutive model and effects of steel fibers, loading patterns, and rebar sizes,” *Composites Part B: Engineering*, vol. 158, pp. 269–278, Feb. 2019, doi: 10.1016/j.compositesb.2018.09.091.

[3] K. Koh, G. Ryu, S. Kang, J. Park, and S. Kim, “Shrinkage Properties of Ultra-High Performance Concrete (UHPC),” *Advanced Science Letters*, vol. 4, no. 3, pp. 948–952, Mar. 2011, doi: 10.1166/asl.2011.1505.

[4] H.-L. R. Chen and J.-H. Choi, “Analysis of Shrinkage and Thermal Stresses in Concrete Slabs Reinforced with GFRP Rebars,” *J. Mater. Civ. Eng.*, vol. 23, no. 5, pp. 612–627, May 2011, doi: 10.1061/(ASCE)MT.1943-5533.0000216.

[5] S. S. and R. A. American Society for Testing and Materials. Committee A-01 on Steel, *Standard test methods and definitions for mechanical testing of steel products*. ASTM International, 2017.

[6] S. H. Park, D. J. Kim, G. S. Ryu, and K. T. Koh, “Tensile behavior of Ultra High Performance Hybrid Fiber Reinforced Concrete,” *Cement and Concrete Composites*, vol. 34, no. 2, pp. 172–

184, Feb. 2012, doi: 10.1016/j.cemconcomp.2011.09.009.

[7] D.-Y. Yoo, J.-J. Park, S.-W. Kim, and Y.-S. Yoon, "Influence of reinforcing bar type on autogenous shrinkage stress and bond behavior of ultra high performance fiber reinforced concrete," *Cement and Concrete Composites*, vol. 48, pp. 150–161, Apr. 2014, doi: 10.1016/j.cemconcomp.2013.11.014.

[8] P. H. Bischoff, "Effects of shrinkage on tension stiffening and cracking in reinforced concrete," *Can. J. Civ. Eng.*, vol. 28, no. 3, pp. 363–374, Jun. 2001, doi: 10.1139/l00-117.

[9] E. Fehling, "Crack Formation and Tensile Behaviour of UHPC Reinforced with a Combination of Rebars and Fibres".

[10] W. Kaufmann, *Strength and Deformations of Structural Concrete Subjected to In-Plane Shear and Normal Forces*. Basel: Birkhäuser Basel, 1998. doi: 10.1007/978-3-0348-7612-4.

[11] P. Marti, M. Alvarez, W. Kaufmann, and V. Sigrist, "Tension Chord Model for Structural Concrete," *Structural Engineering International*, vol. 8, no. 4, pp. 287–298, Nov. 1998, doi: 10.2749/101686698780488875.

[12] V. Sigrist and P. Marti, *Ductility of structural concrete: A contribution*. Institut für Baustatik und Konstruktion, ETH Zürich, 1994.

[13] T. Markić, A. Amin, W. Kaufmann, and T. Pfyl, "Strength and deformation capacity of tension and flexural RC members containing steel fibers," *Journal of Structural Engineering*, vol. 146, no. 5, p.

04020069, 2020.

[14] "Tensile Response of Reinforced Ultra-High-Performance Fiber-Reinforced Cementitious Composites: Modeling and Design Recommendations," *SJ*, vol. 120, no. 1, Jan. 2023, doi: 10.14359/51736122.

[15] D.-Y. Yoo, K.-Y. Kwon, J.-J. Park, and Y.-S. Yoon, "Local bond-slip response of GFRP rebar in ultra-high-performance fiber-reinforced concrete," *Composite Structures*, vol. 120, pp. 53–64, Feb. 2015, doi: 10.1016/j.compstruct.2014.09.055.

[16] "Behavior and Modeling of Bond of FRP Rebars to Concrete." https://ascelibrary.org/doi/epdf/10.1061/(ASCE)1090-0268(1997)1:2(40)?src=getftr (accessed Mar. 27, 2023).

[17] A. Hillerborg, "Numerical methods to simulate softening and fracture of concrete," *Fracture mechanics of concrete: structural application and numerical calculation*, pp. 141–170, 1985.

[18] P. E. Petersson, "FRACTURE ENERGY OF CONCRETE; METHOD OF DETERMINATION".

[19] T. Pfyl, *Tragverhalten von stahlfaserbeton*, no. 279. vdf Hochschulverlag AG, 2003.

[20] B. Zhou, R.-Y. Wu, J. Feng, and S. Yin, "Modeling of tensile behavior of hybrid GFRP-steel reinforced concrete chords," *Composite Structures*, vol. 236, p. 111853, Mar. 2020, doi: 10.1016/j.compstruct.2019.111853.

[21] H. H. Abrishami and D. Mitchell, “Influence of Steel Fibers on Tension Stiffening,” *ACI Structural Journal*, 1997.

[22] P. H. Bischoff and R. Paixao, “Tension stiffening and cracking of concrete reinforced with glass fiber reinforced polymer (GFRP) bars,” *Can. J. Civ. Eng.*, vol. 31, no. 4, pp. 579–588, Aug. 2004, doi: 10.1139/l04-025.

[23] J. Newhook, A. Ghali, and G. Tadros, “Cracking and Deformability of Concrete Flexural Sections with Fiber Reinforced Polymer,” *J. Struct. Eng.*, vol. 128, no. 9, pp. 1195–1201, Sep. 2002, doi: 10.1061/(ASCE)0733-9445(2002)128:9(1195).

[24] “CSA-S806-02_Design-and-Construction-of-Building-Components-with-Fibre-Reinforced-Polymers.pdf.” Accessed: Jun. 14, 2023. [Online]. Available: http://giacoketcau.com/download/CSA-S806-02_Design-and-Construction-of-Building-Components-with-Fibre-Reinforced-Polymers.pdf

[25] “NF-P-18-710-UHPC.pdf.” Accessed: Jun. 14, 2023. [Online]. Available: http://uhpc.com.vn/wp-content/uploads/2018/09/NF-P-18-710-UHPC.pdf

[26] 최정욱, 조창빈, and 김지상, “섬유보강 SUPER Concrete 구조설계지침,” 콘크리트학회지, vol. 28, no. 1, pp. 26–30, 2016.

초 록

GFRP 및 철근 보강 UHPFRC의 인장 거동 특성

홍 승 기

서울대학교 건축학과 대학원

초고성능 섬유보강 콘크리트 (Ultra-High-Performance-Fiber-Reinforced-Concrete, UHPFRC)에 보강근을 결합하면(R-UHPFRC) 기존의 철근 콘크리트보다 더욱 엄격한 내구성과 기계적 요구사항을 충족하는 구조적인 해결책을 얻을 수 있다. 하지만, 기존의 철근 콘크리트보다 높은 수축 및 보강근 구속으로 인한 높은 잔류응력 형성은 해결해야할 문제이다. 현재 유리섬유 보강 폴리머(GFRP) 보강근의 일반콘크리트 및 초고성능 콘크리트(UHPC)에 적용에 관한 연구는 원활히 진행되고 있다. 하지만, 초고성능 섬유보강 콘크리트와의 합성에 대한 연구는 부족한 실정이며, 특히, 혼입되는 강섬유의 부비 비율의 영향에 대한 연구는 더욱 필요하다고 사료된다.

본 논문의 목적은 초고성능 섬유보강 콘크리트(UHPFRC)가 철근

및 유리섬유보강폴리머(GFRP) 보강근으로 보강하였을 때 어떠한 거동을 보이는지 살펴보고, 이들을 비교분석하는 것이다. 구체적으로, 보강근의 종류와 강섬유 부피 비율의 변화가 R-UHPFRC의 단축 방향 인장거동에 미치는 영향에 중점을 두며, 인장부재의 수축이 미치는 구조적 영향 및 인장 증강 효과를 탐구하는 체계적인 접근 방식을 따른다.

먼저, 탄성 및 소성 상태에서의 궁극적인 응력 및 변형과 함께 균열 형성과 특성의 관찰을 통해 단축 방향 인장 거동에 대한 R-UHPFRC 시편의 전반적인 분석을 한다. 또한, 시편 단축을 야기하는 수축과, 이로 인한 잔류 응력에 대한 영향을 분석하며, 실험결과와 이론적 결과에서의 균열 응력을 비교 검토한다. Tension Chord Model 및 Load Sharing Concept를 사용하여, 인장시편에서의 콘크리트와 보강근의 인장응력 기여도를 분석하고 다양한 변수에 대한 인장 증강 효과를 비교한다.

직관적 관찰에서 분석 결과에 이르기까지 이 연구의 포괄적인 접근 방식은 UHPFRC 구조물의 성능과 내구성을 극대화하는 설계 지침을 개발하는 데 기여할 수 있을 것으로 사료된다.

주요어 : 강섬유 부피비, 철근비, 수축, 잔류응력, 인장증강효과

학 번 : 2021-28331